Coherent Raman scattering: applications in imaging and sensing

by
Meng Cui

A dissertation submitted in partial fulfillment
of the requirements for the degree of
Doctor of Philosophy
(Physics)
in The University of Michigan
2009

Doctoral Committee:

Assistant Professor Jennifer P. Ogilvie, Chair
Professor Paul R. Berman
Professor Roberto D. Merlin
Professor Theodore B. Norris
Professor Bing Zhou

This work is dedicated to my parents.

ACKNOWLEDGEMENTS

First, I would like to acknowledge the support and guidance given by Professor Ogilive. She introduced me to the field of nonlinear microscopy and gave me the opportunity and freedom to build up the entire nonlinear microscopy and spectroscopy experiments. Despite her busy schedule, she always made time for discussion which helped me to progress on my research. In her team, I was always encouraged to test new ideas and improve my experiment. I am very grateful to have the opportunity to work in her lab. I also thank Professor Rand for introducing me to nonlinear laser spectroscopy.

University of Michigan in Ann Arbor is an unique place in that it gathers many world class experts in atomic physics, quantum optics, and ultrafast science. I truly enjoyed most of the FOCUS seminars and also the courses given by many of the experts, such as statistic optics by professor Leith who is known as the father of modern holography, quantum optics by professor Berman, ultrafast optics by professor Norris, coherent control by professor Bucksbaum, and the summer course on phonon by professor Merlin. The impact on me is beyond the knowledge you impart through the courses. More important is the enthusiasm and interest you show towards the specific field of science.

I also like to thank all my friends in physics who played basketball on many of the Saturdays. I enjoyed the competence we showed on the basketball court. Despite that each of us worked on quite difference field in physics, we always motivate each other

throughout the years in Michigan. I truly benefit a lot from the discussions with the students in Professor Steel's lab, Professor Merlin's lab, and Professor Raithel's Lab. Especially I like to thank Xiaodong Xu who generously shares his broad experience in laser spectroscopy both in experiment and in theory.

During my first three years in Michigan, I enjoyed the student seminars organized by the optics club in north campus which eventually found the OSA student chapter in Ann Arbor. Many of the interesting talks draw my interest into the field of optics science. I am grateful to be a part of the optics club as a beginning graduate student and to have the opportunity to discuss optics science with many senior graduate students at that time.

Most importantly I like to thank the patience and support from my parents in the past six years, which has given me tremendous amount of courage and confidence to face the challenges during my Ph.D. study. I feel very lucky to meet my wife Tsai-wei in Michigan. I like to thank her love and encouragement. I also benefit a lot through the discussion with her on various simulation techniques. I dedicate this thesis to my parents and my wife.

TABLE OF CONTENTS

DEDICATION . . . . . **ii**

ACKNOWLEDGEMENTS . . . . . **iii**

LIST OF FIGURES . . . . . **vii**

LIST OF APPENDICES . . . . . **xii**

ABSTRACT . . . . . **xiii**

CHAPTER

I. Introduction 1

1.1 Motivation for nonlinear microscopy 1
1.2 Coherent anti-Stokes Raman scattering (CARS) microscopy: a brief review . 3
1.2.1 Implementations of CARS microscopy 6
1.2.2 Single mode CARS and multiplex CARS 8
1.2.3 Nonresonant signal suppression 10
1.3 Thesis outline and chapter overview 13

II. Theory 15

2.1 Spontaneous Raman scattering 15
2.2 Coherent Raman scattering 18
2.3 Optical imaging in microscopy 19
2.3.1 Incoherent imaging 20
2.3.2 Coherent imaging 23
2.3.3 Coherent vs incoherent Raman imaging 27

III. Fourier transform CARS microscopy 31

3.1 Introduction 31
3.2 Motivation of time domain coherent Raman imaging 31
3.3 Experiment setup 33
3.4 Stability and position accuracy 37
3.5 Signal analysis 40
3.6 FTCARS spectroscopy 41
3.7 Power dependence measurement 41
3.8 Concentration dependence measurement 44
3.9 Spectral filtering and excitation considerations 44
3.10 Imaging applications 47
3.11 Biological imaging 50
3.12 Combined with two-photon fluorescence imaging 51

3.13 Conclusion . . . 51

IV. Interferometric Fourier transform CARS microscopy . . . 54

4.1 Introduction . . . 54
4.2 Noise analysis . . . 54
4.3 Idea for achieving shot noise limited SNR . . . 56
4.4 Experimental setup . . . 59
4.5 Phase stability . . . 62
4.6 Experimental results . . . 62
4.7 Comparing IFTCARS with pump-probe impulsive Raman scattering . . . 67
4.8 Dual channel detection . . . 67
4.9 Conclusion . . . 68

V. Spectral-domain coherent Raman imaging . . . 70

5.1 Introduction . . . 70
5.2 Benefits of spectral domain measurements . . . 70
5.3 Theory of time delayed spectral domain coherent Raman measurement . . . 71
5.4 Implementation with a single pulse . . . 73
5.5 Interferometric time-delayed spectral domain CARS . . . 74
5.6 Signal to noise ratio comparison between spectral domain and time domain methods . . . 84
5.7 Signal to noise ratio comparison (experiment) . . . 85
5.8 Conclusion . . . 91

VI. Coherent versus incoherent Raman scattering . . . 92

6.1 Introduction . . . 92
6.2 Theory . . . 93
6.3 Experiment . . . 94
6.4 Solution measurements . . . 98
6.5 Conclusion . . . 100

VII. Coherent Raman scattering in the near field . . . 102

7.1 Introduction . . . 102
7.2 Introduction to surface plasmons . . . 104
7.3 Experiment . . . 107
7.4 Conclusion . . . 112

VIII. Conclusion . . . 114

8.1 Summary . . . 114
8.2 Future directions . . . 116

APPENDICES . . . **117**

BIBLIOGRAPHY . . . **126**

LIST OF FIGURES

Figure

1.1 The energy diagram of (a) CARS and (b) nonresonant FWM. 4

1.2 Experimental setup of the first CARS spectroscopy measurement.[1] 5

1.3 Experimental setup of the first CARS Microscope. 6

1.4 Setup for synchronizing two Ti:sapphire oscillators. [2] 7

1.5 Raman spectra of a single intact cell and a single metaphase chromosome.[3] 9

1.6 (a) Energy diagram of single mode CARS, narrow band pump and Stokes pulses drive a single Raman mode. (b) Energy diagram of multiplex CARS, narrow band pump and broad band Stokes pulses drive all the Raman modes within the Stokes pulse bandwidth. A narrow band probe pulse generates broad band CARS signal. . 10

2.1 Illustration of the focus in spherical coordinates[4] 21

2.2 The imaginary part of E field at the focus of a NA1.2 water immersed objective lens with filling factor $f_0 = 1$. 24

2.3 The spherical volume integral of the signal as a function of spherical radius R for one-photon, two-photon and three-photon absorption. 24

2.4 CARS signal and three photon fluorescence signal generated at the boundary of Raman active medium and Raman inactive medium as a function of the focus position. 26

2.5 The incoherent and coherent signal dependence on the NA of an air objective lens and a water immersed objective lens. 30

3.1 Experiment setup of ISRS. [5] 32

3.2 (a) Experiment setup of FTCARS. BS: beam splitter; Obj: objective lens; LP: long-pass filter; SP: short-pass filter, PMT: photomultiplier tube, DC: dichroic beam splitter. The DC before the objective collects fluorescence in the epi direction for simultaneous CARS and fluorescence imaging. (b) Energy diagram of FTCARS. . 34

3.3 Photo of the laser scanning microscope (Prairie Technologies). 35

3.4 Spectral filtering method: the blue edge of the input pulse is removed by a long pass filter. The interaction with the sample generates blue shifted CARS and NR signals. A short pass filter is used to block the laser light and let the blue shifted signal enter the detecor. 36

3.5 Michelson interferometer setup. The red dotted line is the path of the reference beam (633nm) and the yellow solid line is the path of the 12fs pulses. PD: Si photodiode, BS: beam splitter, M: mirror, Stage: translation stage driven by a DC motor of 7nm resolution, HeNe:Helium-neon laser (reference laser). 37

3.6 (a) NR signal spectral interference. Data acquisition time for each spectrum is 100msec. 100 spectra taken over 15 seconds are overlapped in the plot. (b) Absolute value of the Fourier transform of the interferogram. (c) The phase variation at 290 fs position over 150 seconds. 39

3.7 Simulated (left) and experimental (right) FTCARS results. a) Spectrum of the pump and probe pulse. The locations of the long pass (dashed) and short pass (solid) filters are also indicated. b) Time domain FTCARS signal for pyridine including the dominant CARS modes at 991 cm^{-1} and 1030 cm^{-1}, with smaller peaks at 983 cm^{-1} and 1070 cm^{-1}. The actual scan length was 12 ps, providing 3 cm^{-1} resolution. c) Fourier transform of the oscillatory part of the time domain data for τ >250fs yields the CARS spectrum. 42

3.8 Power dependence measurement on 2propanol. Linear fit indicates slopes of 1.18(first pulse) and 2.16(second pulse). 43

3.9 FTCARS signal of the 820cm^{-1} mode of 2-propanol at different concentrations. The experimental data is fitted with a quadratic function which passes the origin. . 45

3.10 (a) Dependence of the FTCARS resonant signal amplitude on the frequency of the CARS mode for different choices of the longpass filter wavelength. (b) Dependence of the FTCARS resonant signal amplitude on the frequency of the CARS mode to be excited. Several different relative power ratios between pulses 1 and 2 (P_1/P_2) are shown. 46

3.11 (a) NR background signal image of 15μm polystyrene beads in water. (4 mW in each beam, 512×512 pixels, 10μs exposure time per pixel) (b) FTCARS image of a single polystyrene bead from the sample shown in (a) (4 mW in each beam, 36×36 pixels, 7ms exposure time per pixel, spectral resolution of 16 cm^{-1}) (c) FTCARS spectrum from a single pixel within the bead in image (b). 48

3.12 (a) Nonresonant image of 15 μm polystyrene beads embedded in PMMA (b)FTCARS images of the sample shown in (a). The image is acquired with 4 mW power in each beam with a data acquisition time of 7 ms/pixel. The spectral resolution is 16 cm^{-1}. The top row of images show a maximum contribution from the PMMA near 820 cm^{-1} while the lower row corresponds to the dominant polystyrene peak near 1000 cm^{-1} in agreement with the reported Raman spectra [6]. The upper row has been multiplied by a factor of 4 to show the weaker PMMA signal on the same scale as the polystyrene bead. 49

3.13 NR image of Caenorhabditis elegans. 50

3.14 (a) NR image of Caenorhabditis elegans; (b) 40x128 pixel FTCARS image from the area inside the box in (a). 90 picoJ pulses at 75 MHz are used. The data acquisition time is 40ms/pixel. 52

3.15 (a) Polystyrene bead of one micron in diameter. (b) Caenorhabditis elegans. . . . 53

4.1 (a) Time domain noise data, data acquisition rate is 200kHz, the total data collection time is one second; (b) the noise spectrum around 140Hz; (c) the noise spectrum around 1500Hz. 55

4.2 (a) Noise power dependence data at different gain (applied voltage) levels; (b) the same data on double log plot. 57

4.3 4f setup, RM: return mirror, CM: curved mirror, gr: grating, ND: linear ND flter, EM: end mirror (Fourier plane), gl: compensation glass 59

4.4 Probe pulse spectrum variation: The blue edge of the probe pulse is reduced by the 4f setup to provide a controllable local field. Blue shifted NR and CARS(R) signals are generated in the sample. A short pass filter only passes the blue shifted signal and the controllable local field. 60

4.5 Phase stability of IFTCARS setup, determined by spectral interferometry. (a) 10,000 spectra are plotted. The fringes are generated by introducing a time delay on the local field. (b) The absolute value of the Fourier transform of the spectra in (a). (c) The phase at 1689 fs time delay, whose standard deviation 0.0143rad is equivalent to $\lambda/435$ at $\sim 710nm$ 63

4.6 Nonresonant signal image of 4 μm polystyrene beads. The yellow line indicates the linescan position. 64

4.7 (a) Line scan through a $4\mu m$ polystyrene bead taken with IFTCARS. The image is acquired with 1 mW power (13pJ pulse) in each beam with a data acquisition time of 4 seconds and spectral resolution of $16cm^{-1}$. b) Corresponding standard FTCARS line scan (local field is blocked). c) Comparison of CARS spectra at pixel 75 in the two images. 65

4.8 Total noise equivalent power (NEP) vs.local field power. Two regimes are clearly seen: a background noise regime (local field $<$ 1pW) and the shot noise regime (local field $>$ 100pW). The actual local field used in the IFTCARS images shown in Fig. 4.7 is 38pW as indicated with an arrow. 66

4.9 (a) Stokes spectrum. (b) anti-Stokes spectrum. (c) Fourier transform of difference signal. 69

5.1 Energy diagram of the time delayed spectral domain CARS 72

5.2 Laser spectrum 73

5.3 4f setup. rm, return mirror; cm, concave mirror; gr, grating; em, end mirror; cg, compensation glass; nd, neutral density filter; g, coverslip; M, mask. 74

5.4 (a) Spectrum for exciting 800 cm^{-1} mode; (b) spectrum for exciting 1400 cm^{-1} mode; 75

5.5 (a) Interference pattern in the spectral domain. The reduced signal contrast is due to the limited resolution of the compact spectrometer (b) Fourier transform of the interference pattern, indicating a time delay of 250fs. 76

5.6 2propanol signal spectrum without (above) and with (below) time delay. The excitation power is 2.35mW. The data acquisition time is 200msec. In (b) the peak position around 820cm^{-1} agrees with the spontaneous Raman spectrum of 2-propanol within the bandwidth of the probe pulse. The background at 600 cm^{-1} is the NR signal generated by the two pulse pulses. 77

5.7 Input spectrum. The local field from 700 to 720nm is too weak to show up on the same scale. 78

5.8 (a) 100 TDSCARS spectra from 2-propanol, input power = 4.8mW, exposure time = 1 sec; (b) averaged spectrum from (a). 79

5.9 Local field spectrum. 80

5.10 Processed ITDSCARS spectrum of 2-propanol, input power 4.8mW, exposure time 4msec. 81

5.11 (a) Signal spectrum with the local field blocked; (b) CCD noise. 81

5.12 (a) Pump pulses and the probe pulse in time domain ;(b) the blue shifted nonresonant signal. 83

5.13 Simulation of IFTCARS SNR. The three plots on the left side are the time domain signal; The three plots on the right side are corresponding spectra from the Fourier transform. The total photon number is 5E4. Three different detection bandwidths are considered with a total number of time steps of 5E3, 5E4, and 5E5. Note in the case of 5E5, the average photon number per time step is 0.1. A Poisson distribution is used to describe the photon statistics. 86

5.14 Measured CARS spectrum of 2propanol and water with 1600fs delay on the probe beam. 88

5.15 100 2-propanol CARS spectra. Exposure time of each spectrum is one second. . . . 89

5.16 FTCARS time domain data and its Fourier transform 90

6.1 CSRS setup. rm: return mirror, cm: concave mirror, gr: grating, M: amplitude mask, gl: glass slide 94

6.2 (a)-(d) and (e)-(h) are measured on polystyrene beads of 7.3μm and 4.3μm in diameter respectively. The image intensity is the difference in intensity between 1000cm^{-1} and 950cm^{-1}. (a) CSRS, power=4mW, exposure=40msec/pixel. (b) CSRS, power=1.3mW, exposure=100msec/pixel. (c) Raman, power=1.3mW, exposure=100msec/pixel. (d) Averaged spectrum from (b) and (c). (e) CSRS, power=4mW, exposure=50msec/pixel. (f) CSRS, power=1.3mW, exposure=200msec/pixel. (g) Raman, power=1.3mW, exposure=200msec/pixel. (h) Averaged spectrum from (f) and (g). The image sizes are 30μm and 10μm for (a)-(c) and (e)-(g) respectively. 96

6.3 Power dependence measurement of 2-propanol sandwiched between two fused silica slides. The optical path length is $\sim 10\mu m$. 98

7.1 Diagrams of the Kretschmann configuration and the Otto configuration 105

7.2 Reflectivity (a) and intensity enhancement (b) of glass substrate coated with 50nm gold. 106

7.3 (a), SEM image of the nanostructured substrate[7]. (b) Intensity distribution from FDTD simulation for normal incidence. The depth of the void structure is 1250nm and the incident wavelength is 785nm[7]. 108

7.4 (a), photo of the pulse picker. (b) photo of the 4f pulse shaper. The 640 pixel LCD spatial light modulator(SLM) is located at the Fourier plane which is also the symmetry plane of the setup. FM: folding mirror, GR: 600 groves/mm gold coated grating, CM: gold coated concave mirror(f=647mm), BBO: 20μm thick type I BBO crystal for second harmonic generation, BF: bandpass filter for 400nm second harmonic light, FP: fiber coupler to spectrometer. 109

7.5 L: Ti:sapphire oscillator, EO: pulse picker, PL: thin film polarizer, WP: half wave plate, TS: telescope for beam expansion, 4F: 4f pulse shaper, SLM: 640 pixel spatial light modulator, FL: flipper mirror, L1, L2, L3: objective lens, CCD: compact spectrometer, BP: bandpass filter for 400nm light, DC, dichroic beam-splitter, SP: short pass filter, XYZ: 3D translation stage, sample: benzenethiol on gold coated nanostructured substrate, CPU: computer. 110

7.6 (a) FTCARS signal for benzenethiol on the Klarite substrate. (b), Fourier transformed spectrum indicating the modes at 997cm^{-1}, 1021cm^{-1}, and 1072cm^{-1}, as expected from the Raman spectrum[8]. 111

A.1 Second order fringe resolved autocorrelation measured with an GaAsP diode. The dispersion ($\sim 1200 fs^2$) of a NA1.2 water immersed lens is compensated by a pair of chirped mirrors. The estimated pulse duration is $\sim 12 fs$ 119

A.2 Non-collinear autocorrelation measured with ZnS photodiode 120

A.3 (a), MIIPS scan in the first round. (b) MIIPS scan in the last round. (c) calculated spectral phase profile. (d) final second harmonic spectrum 123

LIST OF APPENDICES

Appendix

A. Summary of dispersion measurement and compensation 118
A.1 Low dispersion measurement and compensation 118
A.2 High dispersion measurement and compensation 120

B. Table of acronyms 124

ABSTRACT

In this thesis, I discuss the theory, implementation and applications of coherent Raman scattering to imaging and sensing. A time domain interferometric method has been developed to collect high resolution shot-noise-limited Raman spectra over the Raman fingerprint regime and completely remove the electronic background signal in coherent Raman scattering. Compared with other existing coherent Raman microscopy methods, this time domain approach is proved to be simpler and more robust in rejecting background signal. We apply this method to image polymers and biological samples and demonstrate that the same setup can be used to collect two photon fluorescence and self phase modulation signals. A signal to noise ratio analysis is performed to show that this time domain method has a comparable signal to noise ratio to spectral domain methods, which we confirm experimentally. The coherent Raman method is also compared with spontaneous Raman scattering. The conditions under which coherent methods provide signal enhancement are discussed and experiments are performed to compare coherent Raman scattering with spontaneous Raman scattering under typical biological imaging conditions. A critical power, above which coherent Raman scattering is more sensitive than spontaneous Raman scattering, is experimentally determined to be $\sim$1mW in samples of high molecule concentration with a 75MHz laser system. This finding is contrary to claims that coherent methods provide many orders of magnitude enhancement under comparable conditions. In addition to the far field applications, I also discuss the

combination of our time domain coherent Raman method with near field enhancement to explore the possibility of sensing and near field imaging. We report the first direct time-resolved coherent Raman measurement performed on a nanostructured substrate for molecule sensing. The preliminary results demonstrate that sub 20 fs pulses can be used to obtain coherent Raman spectra from a small number of molecules bound to a specially engineered metal structure and pave the way for a broad range of near field nonlinear experiments which require such short pulses.

CHAPTER I

Introduction

1.1 Motivation for nonlinear microscopy

Imaging is a powerful tool in many scientific research fields. X-ray diffraction has helped physicists to reveal crystal structures of molecules as complex as proteins, providing insight into how their structure gives rise to functionality. Magnetic resonant imaging (MRI) and ultrasound imaging have enabled disease detection at its earliest stage. Conventional optical microscopy has helped biologists to gain insight into cellular structure and function. Among the various imaging techniques, optical imaging has the unique capability of noninvasiveness, high resolution and a relaxed requirement on sample conditions.

Conventional wide field optical microscopy was invented in the sixteenth century. Despite its simplicity, it provides sub micron spatial resolution and has had a tremendous impact in biology and medicine. The contrast mechanism is the transmission or reflectivity of the sample. Since many cellular structures are transparent, the variation of the reflectivity and transmission is very small. Phase contrast and differential interference contrast microscopes have been developed to convert the optical phase differences into intensity differences and greatly enhance the image contrast.

The limitation of the conventional microscope is that it does not provide chemical

specificity. The new frontiers of microelectronics, disease detection, material analysis, and biochemistry demand the ability to visualize the molecular identity in complex materials in real time. Many advanced imaging techniques have been invented to answer these challenges. With the development of fluorescence labels, fluorescence imaging has gained popularity among cell biologists and biochemists because the signal is specific to the label and its sensitivity reaches the single molecule level. Green fluorescent protein[9–12] (GFP) is one of the most important fluorescence markers. The GFP gene can be introduced into the genome of various organisms and expressed. By joining the GFP gene with the gene of the protein of interest, the protein is expressed with a bright fluorescence marker connected to it allowing its motion or even orientation to be studied. Despite its success, fluorescence imaging has several limitations. First of all, the fluorescence molecules have a finite life time under illumination before they are photo-bleached. This actually finds application in membrane research such as Fluorescence recovery after photobleaching (FRAP)[13] and Fluorescence loss in photobleaching (FLIP)[14]. Secondly, through non-radiative energy transfer, the fluorescent molecule may form oxygen radicals and kill the cell expressing it. This phototoxicity property has been applied in photodynamic therapy(PDT)[15]. Thirdly, the types of samples that can be labeled are quite limited. In addition, the labeling may strongly perturb the natural function of the target; in many cases the fluorescent molecule has an even larger size than its target. Current research in nonlinear microscopy is aiming to develop alternative methods that provide endogenous contrast.

Various nonlinear signals, such as second harmonic generation[16], third harmonic generation[17], and self-phase modulation (SPM)[18] have been used for imaging. Second harmonic generation (SHG) arises from the second order nonlinearity of ma-

terials with a noncentrosymmetric molecular organization. Certain biological materials such as collagen can assemble into large noncentrosymmetric structures, making them a good target for SHG microscopy[16]. Third harmonic generation (THG) has no restriction on the symmetry property of the material. THG signals are strong at interfaces and small inhomogeneities of the size smaller than the focus. This has enabled the application of THG in imaging micrometer-sized lipid bodies in hepatocytes[17]. SPM is also a third order nonlinearity which gives rise to blue and red shifted spectral components. Recent research[18] has demonstrated the SPM signatures of neuronal activity.

1.2 Coherent anti-Stokes Raman scattering (CARS) microscopy: a brief review

SHG, THG and SPM derive their contrast from the nonlinearity of the material being imaged and do not require external labeling. One major limitation of these methods is that they lack molecular specificity. One powerful optical method for identifying molecules is Raman spectroscopy. Raman scattering is an inelastic scattering process, during which the scattered light is red or blue shifted by a amount equal to the molecule's vibrational frequency. For a specific molecule, there are a set of vibrational eigenmodes which give rise to a distinct Raman spectrum. Therefore a Raman spectrum can be used as a fingerprint to uniquely reveal the sample's molecular identity. Unfortunately the Raman scattering cross-section is often quite small (more than 10 orders of magnitude smaller than fluorescence), which necessitates relatively high excitation power and long data acquisition time.

Theoretically, the small Raman scattering cross-section is a consequence of the far off resonance of the excitation light. For most biological samples, the lowest electronic resonance is around the ultraviolet (UV). UV light is known to cause sample damage,

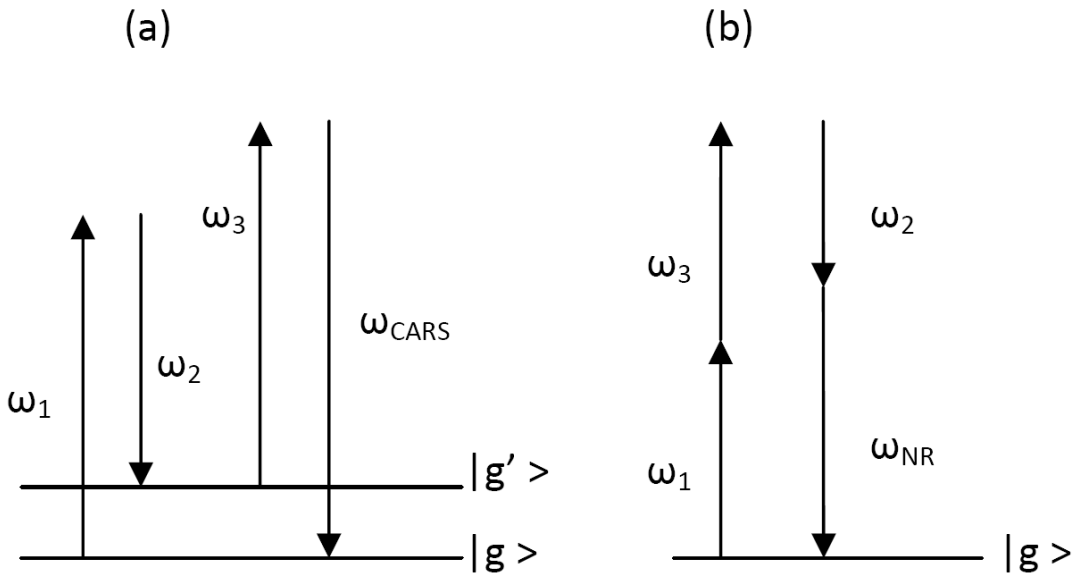

Figure 1.1: The energy diagram of (a) CARS and (b) nonresonant FWM.

and should therefore be avoided for non-invasive imaging. Another way around the small Raman scattering cross-section is by direct excitation of the vibrational states with IR light. Similar to biological molecules, water also absorbs IR light strongly, causing sample heating and damage. In addition, the long wavelength of IR light reduces spatial resolution. The poor performance of IR detectors also limits the attractiveness of IR microscopy.

Coherent anti-Stokes Raman scattering (CARS) is a four wave mixing (FWM) process which probes the third order nonlinearity of molecules. Fig.1.1 (a) is the energy diagram of CARS. If the frequency difference $\omega_1 - \omega_2$ matches the molecule vibration frequency, the two input fields can provide a coherent driving force to all the molecules within the beam path, modulating the material's polarizability. A third field ω_3 probes the modulated polarizability and generates both blue and red shifted light. The photo damage of UV light and the low resolution and detection efficiency of IR light are all circumvented by CARS, which uses near IR pulsed light sources. In addition, the vibration of the molecules is synchronized. Thus the electromagnetic

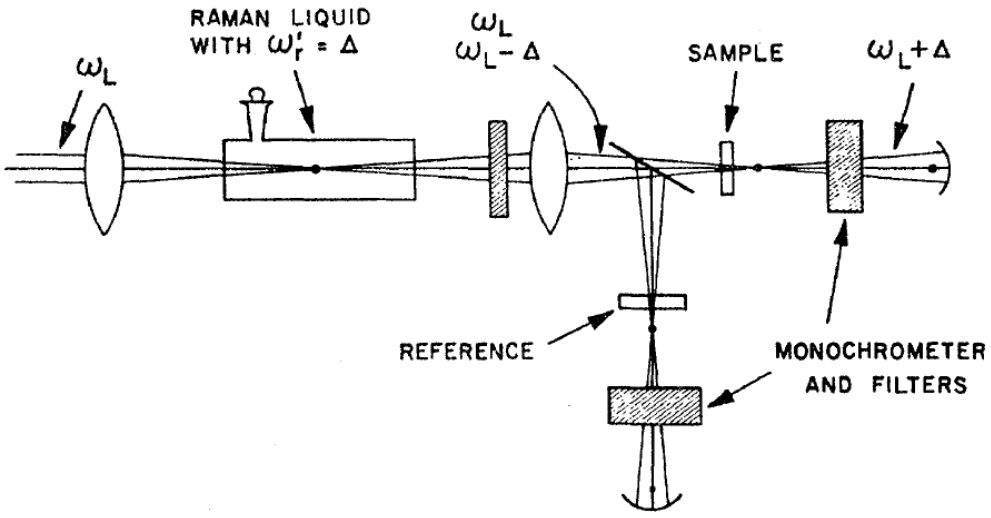

Figure 1.2: Experimental setup of the first CARS spectroscopy measurement.[1]

signal field adds up coherently, in contrast to the incoherent intensity summation in spontaneous Raman scattering.

The blue shifted light (anti-Stokes signal) is used for microscopy application because there is no fluorescence background. However, CARS is not background free. Fig.1.1 (b) shows the energy diagram of another third order process which generates signal light of the same frequency (ω) and direction (k). This signal, which is electronic in nature, is generated regardless of whether the driving fields match the molecule's vibration and it is commonly referred to as nonresonant (NR) signal. The NR signal will be discussed further in **section 1.2.3**.

CARS spectroscopy was first demonstrated in 1965[1]. Fig.1.2 shows the experimental setup, which used a Q-switched Ruby laser to provide powerful pulses to generate Stokes side bands via stimulated Raman scattering in a benzene derivative. The output was filtered and delivered to the sample, after which the blue shifted anti-Stokes signal was detected. Since its initial demonstration, CARS has become a widely adopted method, finding application in physics, chemistry, and material

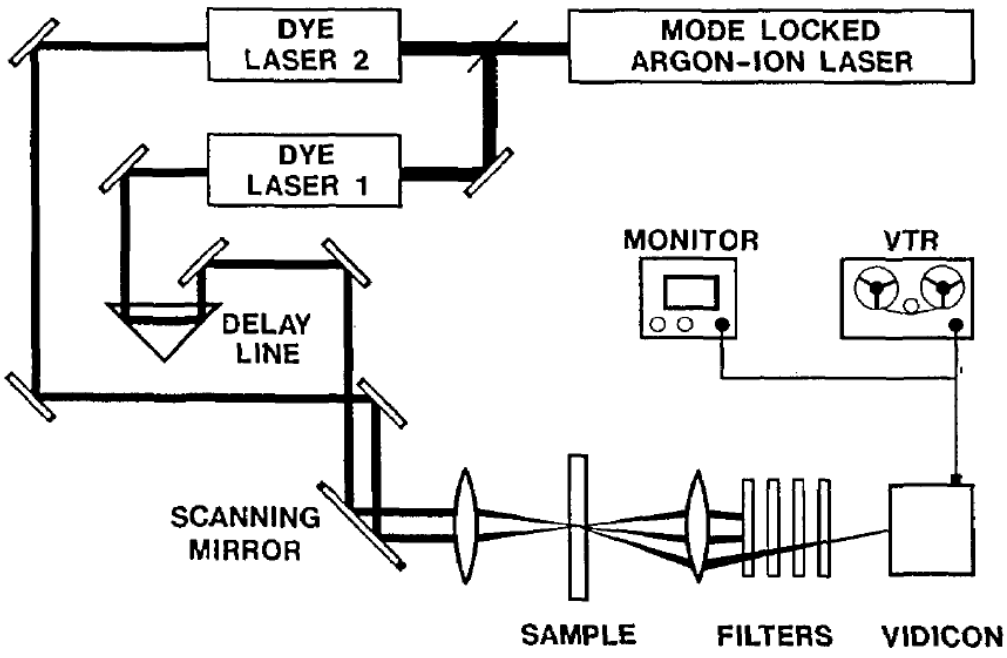

Figure 1.3: Experimental setup of the first CARS Microscope.

science[19–23].

1.2.1 Implementations of CARS microscopy

With the development of laser technology, tunable picosecond mode-locked lasers became available. In the early 80's [24], visible picosecond dye lasers were employed for the first CARS microscopy (Fig.1.3). The visible light source works poorly in biological samples due to the presence of two-photon resonances, that increased the NR background. In addition, the non-collinear beam geometry in this experiment prevents high spatial resolution imaging.

It was not until the late 90's [25] that near-IR pico-second solid state pulsed light sources were used for imaging biological samples. Near-IR pulsed sources turn out to be a much better tool than visible light sources for three reasons: firstly, the Rayleigh scattering is much reduced and hence the light penetrates deeper into the sample; secondly, the NR signal is lower for longer wavelength and hence the NR background

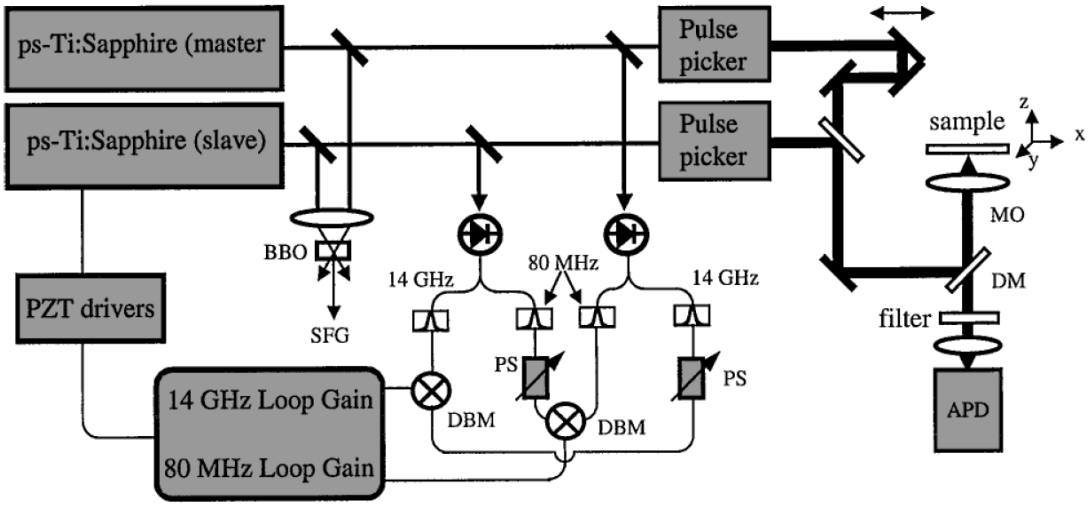

Figure 1.4: Setup for synchronizing two Ti:sapphire oscillators. [2]

is weaker; thirdly there is less photo damage at longer wavelengths.

The typical Raman line width of biological molecules in room temperature is $10cm^{-1}$. In the time domain, this means that the coherent molecule oscillation lasts 3.3 picoseconds. If pulses much longer than 3.3 picoseconds are used for excitation, the coherence of the molecule system increases at the beginning of the pulse and then reaches a steady state value balanced by excitation and coherence decay. The excitation efficiency can be significantly improved if the pulse duration matches the Raman mode bandwidth. With picosecond pulses, the coherence builds up over the entire pulse duration.

In the first CARS microscopy experiment two oscillators were used to provide the pump (ω_1) and the Stokes (ω_2) beam. Quite often the pump beam also plays the role of probing the Raman coherence and generates blue shifted Stokes light. To maintain stable temporal overlap, the two oscillators have to be precisely locked since temporal walk off on the order of one pico-second can cause significant signal fluctuation. Fig.1.4 is one example of the synchronized system. One oscillator(master) provides

the reference repetition rate signal, to which the other oscillators(slave) is actively locked by a fast piezo actuator.

A simpler and more robust method than this early implementation is to use a single pulsed source to generate light of different colors as in the first CARS spectroscopy experiment[1]. This way the timing jitter is negligible. One commonly used nonlinear optics technique is parametric down conversion based on second order nonlinearity χ^2[26]. Another economic and widely used method is continuum generation in photonic crystal fibers based on the third order nonlinearity χ^3 [27]. Alternatively, a single ultra-broadband femtosecond laser can be used.

1.2.2 Single mode CARS and multiplex CARS

The simplest CARS measurement is to use two picosecond pulses to probe a single Raman mode. A single detector such as a Photomultiplier tube (PMT) or single photon counting Avalanche photodiode (APD) is used to collect the signal. For microscopy, this method finds applications if the Raman modes are well isolated and a single Raman mode is able to distinguish between molecules of interest. The C-H vibration around $3000cm^{-1}$ is strong and the C-H bonds are abundant in biological molecules. To date, most CARS microscopy applications have been based on imaging C-H distributions with the single mode CARS method [2, 19, 20, 28, 29] in systems such as myelin and lipids. While useful, the chemical information in this spectral region is limited.

The Raman spectrum between 700 and 1800 cm^{-1} contains most of the structural information of a molecule and is known as the fingerprint regime(Fig.1.5). The spectrum in this regime is often congested. Thus, acquiring CARS spectra over a broad bandwidth becomes necessary for separating different molecular components. The Stokes pulse is often replaced with a short broadband pulse to access more than

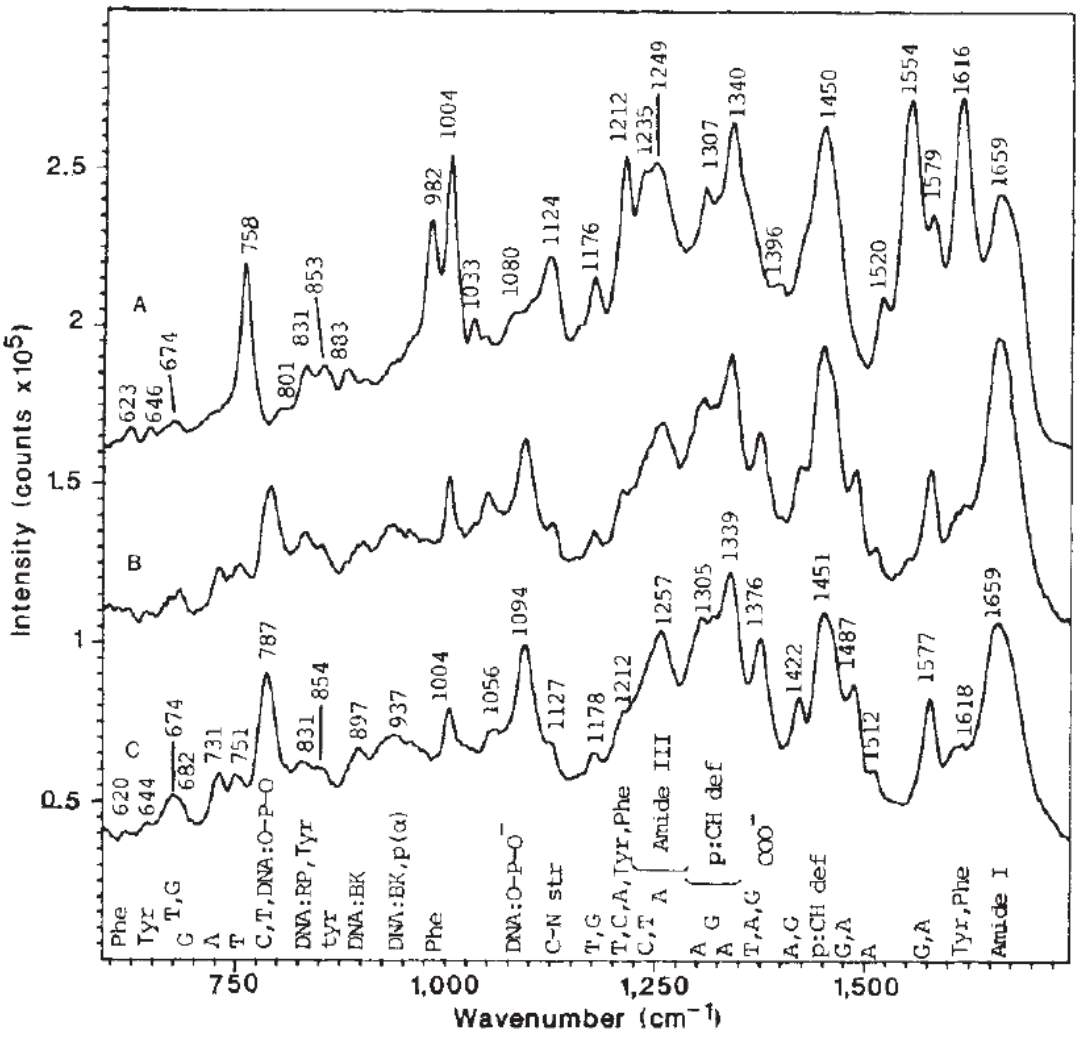

Figure 1.5: Raman spectra of a single intact cell and a single metaphase chromosome.[3]

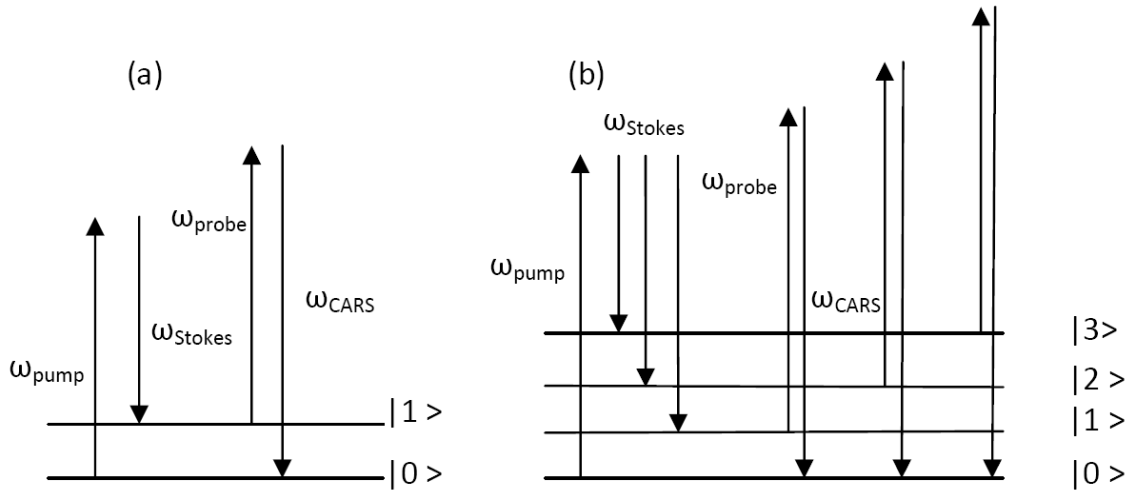

Figure 1.6: (a) Energy diagram of single mode CARS, narrow band pump and Stokes pulses drive a single Raman mode. (b) Energy diagram of multiplex CARS, narrow band pump and broad band Stokes pulses drive all the Raman modes within the Stokes pulse bandwidth. A narrow band probe pulse generates broad band CARS signal.

one mode at a time(Fig.1.6). This method is referred to as multiplex CARS[30], as depicted in Fig.1.6(b). The light source for fingerprint multiplex CARS can be further simplified with the commercially available sub 20 fs Ti:sapphire oscillator. The bandwidth of such short pulses is broad enough to provide both the pump and Stokes light. The spectral shape and phase are often engineered to provide both the selectivity and the spectral resolution[31–37].

1.2.3 Nonresonant signal suppression

In dielectric media, the electronic four wave mixing generates blue shifted NR signal at the anti-Stokes frequency. For multiplex CARS, the NR signal increases signal background and also distorts the Raman lineshape. Because this background signal may vary at different positions of the sample, it is difficult to make numerical corrections. Based on the difference between the NR signal and the resonant signal, a few optical techniques have been applied to suppress the NR signal.

One method of background suppression is based on polarization discrimination of the anti-Stokes signal. This method works very well in spectroscopy for studying samples in liquid form[38]. For biomedical applications, the NR signal generated may not have a fixed polarization, and the scattering inside the sample can often distort the polarization and cause errors in measurement.

Because the NR signal has a cubic dependence on the instantaneous light intensity, splitting a single short femtosecond pulse to a periodic pulse train can lower the NR signal. If the temporal spacing between the pulses equals an integer number of Raman periods, the pulse train can selectively excite a single Raman mode, providing selectivity. Phase shaping technique is used to generate the pulse train and control the pulse spacing. This method was first demonstrated by Weiner in 1991 in spectroscopy [5], and later employed by Silberberg's group in microscopy, imaging non-biological samples [33–37]. The beating of two picosecond pulses with frequency difference matching a Raman mode is also a periodic pulse train with spacing equal to a single Raman period. From this point of view, the NR suppression is better with picoseconds pulses since it has the maximum number of pulses and hence the lowest possible instantaneous light intensity.

One clever trick for NR suppression is to use the NR signal as a spectral local oscillator and control the interference between the local oscillator and the CARS signal with pulse shaping techniques [31, 32] to measure the complex χ^3, which has been developed concurrently with our time domain CARS methods. Since χ^3_{NR} is a real number, the imaginary part of χ^3 is free from NR contribution. The polarization of the probe beam is set perpendicular to that of the pump beam. Polarizers are used to combine the CARS signal with the NR signal. Depending on the orientation of the polarizer, the coherent signal is added to the NR signal with or without a

π phase difference. Measuring the difference between the two signals can yield the CARS spectrum free from NR background, which has been demonstrated in imaging polymer samples. This method relies on controlling the polarization of light, which may suffer from errors caused by scattering in biological samples.

One other difference between the NR signal and the resonant signal is the time scale of the response function. The NR signal originates from electron's motion which is much faster than nuclear motion(Raman signal). If the time response function can be directly measured, the two signal components can be easily separated from each other. With sub 20 fs pulses, the Raman modes within the fingerprint regime can be directly time resolved[39, 40]. This is what we believe to be the most robust method for separating the resonant signal from the NR signal and is the basis for much of the work presented here.

CARS microscopy revived in 1999 [25] and has found several applications in biomedical research [28, 41] based on imaging C-H vibration mode. Only a few groups have attempted to apply CARS in the Raman fingerprint regime [42–44]. The research discussed in this thesis provides a very ideal solution to fingerprint CARS imaging for its simplicity, robustness, resolution, and sensitivity. An experimental comparison between spontaneous Raman scattering and coherent Raman scattering is performed under conditions relevant for biological imaging, providing a basis for evaluating the advantages of coherent Raman imaging. We also discuss the preliminary studies on near field coherent Raman scattering, which have shown promising results for exploring the possibility of near field CARS imaging.

1.3 Thesis outline and chapter overview

In this thesis, I will discuss two unique coherent Raman imaging techniques for effectively isolating the resonant signal from the NR signal. Both of these two techniques rely on time delayed detection.

Chapter 2 provides the theoretical background of spontaneous Raman scattering and coherent Raman scattering. The theory can help answer three basic questions: 1) Which vibrational modes are Raman active ? 2) Why is coherent Raman scattering stronger than spontaneous Raman scattering ? 3) How can we describe the optical driving force ? The general theory of optical imaging and nonlinear signal generation at the tight laser focus are presented.

In **Chapter 3**, the theory of Fourier transform CARS(FTCARS), its implementation and imaging applications are discussed. The main advantage of FTCARS is its ability to isolate coherent Raman signal from the NR signal. As a demonstration, we apply FTCARS microscopy to image polymers [45, 46] and biological samples. The work in this chapter has been published in [45, 46].

In **Chapter 4**, interferometric Fourier transform CARS(IFTCARS) [47] is discussed with an emphasis on the signal to noise ratio. The motivation behind this method is to reach the shot-noise limited signal-to-noise ratio (SNR) which is the highest possible SNR achievable with a classical light source. The work in this chapter has been published in [47].

In the field of OCT[48, 49] and sum frequency generation[50], there has been discussion about the SNR advantage of spectral domain methods over time domain methods. In **Chapter 5**, a simple argument is presented to show that the SNR of IFTCARS is similar to the spectral domain method given that both methods are

shot-noise limited. Experimental results are presented to confirm the prediction.

As a third order coherent process, CARS has a cubic dependence on the input power and quadratic dependence on molecule concentration, in contrast to the linear power and concentration dependence of spontaneous Raman signals. Intuitively there exists a critical power below which spontaneous Raman signal is stronger than the coherent signal. In **Chapter 6**, the coherent method is directly compared with the incoherent method under conditions appropriate for biological imaging. The critical powers of several materials are determined in experiment. The work presented in this chapter has recently been submitted for publication.

While the first six chapters of the thesis focus on the development of far-field CARS imaging methods, higher sensitivity and better spatial resolution will be desirable for many imaging applications. The near field bound to the metal dielectric interface is known to be stronger than the input far field excitation. The ability to control the optical near field has enabled many applications in sensing and imaging, such as surface enhanced Raman scattering[51–53] and tip enhanced Raman microscopy[54–59]. In **Chapter 7**, the first time-resolved coherent Raman scattering experiment on nanostructured gold coated substrate is presented. The measurement results presented here are preliminary studies to motivate the development of NR background free tip enhanced CARS microscopy. It may also find applications in biosensing[60, 61].

CHAPTER II

Theory

2.1 Spontaneous Raman scattering

Raman scattering is an inelastic scattering process. Semiclassical theory[62] can be employed to compute the scattering cross section. In the dipole approximation, the Hamiltonian of a molecule interacting with an electromagnetic field is

$$H = H_0 - \mathbf{D} \cdot \mathbf{E} \tag{2.1}$$

where H_0 is the Hamiltonian of a molecule in the absence of electromagnetic field, $\mathbf{D}$ is the electric dipole moment of the molecule, and $\mathbf{E}$ is the input E field

$$\mathbf{E} = \mathbf{E}_- e^{-i\omega t} + \mathbf{E}_+ e^{i\omega t}, \tag{2.2}$$

with $\mathbf{E}_- = \mathbf{E}_+^*$. If $\mathbf{D} \cdot \mathbf{E}$ is much smaller than H_0, the Schrödinger equation

$$\left\{ H_0 - \mathbf{D} \cdot \mathbf{E}_- e^{-i\omega t} - \mathbf{D} \cdot \mathbf{E}_+ e^{i\omega t} \right\} \Psi = i\hbar(\partial/\partial t)\Psi \tag{2.3}$$

can be solved by perturbation theory. If $\psi_{0l} exp[-\varepsilon_{0l} t/\hbar]$ is the eigenfunction of H_0, to the first order, the perturbed wave function can be written as

$$\Psi_l = e^{-i\varepsilon_{0l} t/\hbar} \left\{ \psi_{0l} + \frac{1}{\hbar} \sum_\beta \sum_r \left[\frac{< r|D_\beta|l >}{\omega_{rl} - \omega} \psi_{0r} E_{-\beta} e^{-i\omega t} + \frac{< r|D_\beta|l >}{\omega_{rl} + \omega} \psi_{0r} E_{+\beta} e^{i\omega t} \right] \right\} \tag{2.4}$$

where β denotes the vector components of $\mathbf{D}$ and $\mathbf{E}$ and l is the quantum number of the state. The expectation value of the electric dipole moment associated with the transition between l and m states is

$$D_\alpha(t) = \sum_\beta \left\{ [\alpha^{lm}_{\alpha\beta}(\omega)]^* E_{-\beta} e^{-i(\omega+\omega_{lm})t} + \alpha^{lm}_{\alpha\beta}(\omega) E_{+\beta} e^{i(\omega+\omega_{lm})t} \right\} \tag{2.5}$$

where

$$\alpha^{lm}_{\alpha\beta}(\omega) = \frac{1}{\hbar} \sum_r \left\{ \frac{< l|D_\alpha|r >< r|D_\beta|m >}{\omega_{rm} + \omega} + \frac{< l|D_\beta|r >< r|D_\alpha|m >}{\omega_{rl} - \omega} \right\} \tag{2.6}$$

is the transition polarizability. The Born-Oppenheimer approximation and the normal-mode expansion can be used to simplify the results [63]. In the Born-Oppenheimer approximation, the eigenfunction of H_0 can be written

$$\Psi_{n\upsilon}(x, X) = \chi_{n\upsilon}(X)\varphi_n(x, X), \tag{2.7}$$

where $\varphi_n(x, X)$ is the electron's wave function with quantum number n, whose eigenvalue $E_n(X)$ for the electronic motion is a function of nuclear coordinates X. The nuclear part $\chi_{n\upsilon}(X)$ (υ is the nuclear motion quantum number) moves in an effective potential $E_n(X) - E_n(X^0)$. The eigenvalue of H_0 can be written

$$E_n(X^0) + \epsilon_{n\upsilon}, \tag{2.8}$$

in which the vibrational energy is much smaller than the electronic transition energy, $\epsilon_{n\upsilon} \ll E_{n'}(X) - E_n(X)$. The transition polarizability of a vibrational transition can be written

$$\alpha^{\upsilon\upsilon'}_{\alpha\beta} = \frac{1}{\hbar} \sum_{n''} \sum_{\upsilon''} \left\{ \frac{< 0\upsilon|D_\alpha|n''\upsilon'' >< n''\upsilon''|D_\beta|0\upsilon' >}{\omega_{n''\upsilon'',0\upsilon'} + \omega} + \frac{< 0\upsilon|D_\beta|n''\upsilon'' >< n''\upsilon''|D_\alpha|0\upsilon' >}{\omega_{n''\upsilon'',0\upsilon} - \omega} \right\} \tag{2.9}$$

The summation over n'' can be split into two terms corresponding to $n'' = 0$ and $n'' \neq 0$. By using the approximation $\omega_{n''\upsilon'',0\upsilon} = \omega_{n'',0}$ the polarizability becomes

$$\alpha_{\alpha\beta}^{\upsilon\upsilon'} = \frac{1}{\hbar}\sum_{\upsilon''}\left\{\frac{<\upsilon|D_\alpha(X)|\upsilon''><\upsilon''|D_\beta(X)|\upsilon'>}{\omega_{\upsilon''\upsilon'}+\omega} + \frac{<\upsilon|D_\beta(X)|\upsilon''><\upsilon''|D_\alpha(X)|\upsilon'>}{\omega_{\upsilon''\upsilon}-\omega}\right\}$$
$$+\frac{1}{\hbar}\sum_{n''}\left\{\frac{<0\upsilon|D_\alpha|n''\upsilon''><n''\upsilon''|D_\beta|0\upsilon'>}{\omega_{n''0}+\omega} + \frac{<0\upsilon|D_\beta|n''\upsilon''><n''\upsilon''|D_\alpha|0\upsilon'>}{\omega_{n''0}-\omega}\right\} \tag{2.10}$$

where

$$\mathbf{D}(X) = \int \varphi_0^*(x,X)\mathbf{D}(x,X)\varphi_0(x,X)dx \tag{2.11}$$

The first term depends only on the nuclear motion with electrons in the lowest level and is referred to as the ionic part of the polarizability. The second term, referred to as the electronic polarizability, can be written as $<\upsilon|\alpha_{\alpha\beta}(\omega,X)|\upsilon'>$, with

$$\alpha_{\alpha\beta}(\omega,X) = \frac{1}{\hbar}\sum_{n''\neq 0}\left\{\frac{<0|D_\alpha|n''><n''|D_\beta|0>}{\omega_{n'',0}+\omega} + \frac{<0|D_\beta|n''><n''|D_\alpha|0>}{\omega_{n'',0}-\omega}\right\} \tag{2.12}$$

For the infrared refractive properties, the ionic parts and the electronic parts are of the same order of magnitude. For the optical frequency, ω is the same order of magnitude as $\omega_{n''0}$ and is much larger than $\omega_{\upsilon''\upsilon}$. Thus Eq. 2.10 indicates that the ionic part of the polarizability is divided by an extra factor of $10^2 - 10^3$ and becomes much smaller than the electronic part.

$\alpha(\omega, X)$ can be expanded in Taylor's series with respect to the normal coordinate q where $q = \mu^{-1/2}X$ and μ is the reduced mass.

$$\alpha(\omega,X) = \alpha(\omega,X^0) + \sum_i \left(\frac{\partial\alpha}{\partial q_i}\right)_0 q_i + \frac{1}{2}\sum_{ij}\frac{\partial\alpha}{\partial q_i\partial q_j}q_i qj + \ldots \tag{2.13}$$

The Stokes and anti-Stokes signals are contributed by the first order term, whose

matrix element can be written

$$\begin{aligned} < \upsilon|\alpha(\omega, X)|\upsilon' > &= \sum_i < \upsilon| \left(\frac{\partial\alpha}{\partial q_i}\right)_0 q_i|\upsilon' > \\ &= \sum_i \left(\frac{\partial\alpha}{\partial q_i}\right)_0 < \upsilon|q_i|\upsilon' > \end{aligned} \tag{2.14}$$

Eq. 2.14 shows that the normal mode coordinate q is involved in the dynamics and $\left(\frac{\partial\alpha}{\partial q_i}\right)_0$ is the coupling constant for the light matter interaction. Given the polarizability, the dipole moment can be written $D_\alpha = \sum_\beta \alpha_{\alpha\beta} E_\beta$ and the radiated power per unit solid angle by the dipole can be calculated with classical electrodynamics.

$$\frac{dP}{d\Omega} = \frac{1}{4\pi c^3} \left(\frac{\partial^2 D}{\partial t^2}\right)^2 \sin^2\varphi \tag{2.15}$$

where φ is the angle between the direction of the dipole moment and the direction of the emitted radiation. By using Eq. 2.14 and $< 1|q|0 >= (\hbar/2\omega_\upsilon)^{1/2}$, the Raman scattering induced by a linearly polarized light can be written

$$\frac{dP}{d\Omega} = \frac{\omega_s^4}{2\pi c^3} \left(\frac{\partial\alpha}{\partial q}\right)_0^2 \frac{\hbar}{2\omega_\upsilon} |E_L|^2 \cos^2\theta \tag{2.16}$$

where θ is the angle between the input and the scattered wave. The total scattered power by the dipole is

$$P = \frac{4\omega_s^4}{3c^3} \left(\frac{\partial\alpha}{\partial q}\right)_0^2 \frac{\hbar}{2\omega_\upsilon} |E_L|^2 \tag{2.17}$$

From Eqs. 2.16 and 2.17, the differential and total spontaneous Raman scattering cross section for a single molecule can be derived.

$$\frac{d\sigma}{d\Omega} = \frac{dP}{d\Omega} \left(\frac{c|E_L|^2}{4\pi}\right)^{-1} = \frac{2\omega_s^4}{c^4} \left(\frac{\partial\alpha}{\partial q}\right)_0^2 \frac{\hbar}{2\omega_\upsilon} \cos^2\theta, \tag{2.18}$$

$$\sigma = \frac{16\pi\omega_s^4}{3c^4} \left(\frac{\partial\alpha}{\partial q}\right)_0^2 \frac{\hbar}{2\omega_\upsilon} \tag{2.19}$$

2.2 Coherent Raman scattering

If two coherent electromagnetic fields are present with frequency difference matching the vibration frequency of a Raman mode, the E fields can provide a force driving

the Raman vibration coherently. The light matter interaction Hamiltonian is

$$H_{int} = \left(\frac{\partial \alpha}{\partial q}\right)_0 q E_L E_S^*. \tag{2.20}$$

If a new variable is defined as $Q = N^{1/2} < q >$, the dynamics of the Raman vibration can be described by the classical equation of motion

$$\frac{\partial^2 Q}{\partial t^2} + 2\Gamma \frac{\partial Q}{\partial t} + \omega_0^2 Q = N \frac{\partial \alpha}{\partial Q} E_L E_S^* \tag{2.21}$$

If one of the coherent field is generated from vacuum via Stokes scattering, the wave equation can be written

$$\nabla^2 E_S - \frac{\epsilon_0}{c^2} \frac{\partial^2}{\partial t^2} E_S = -\frac{4\pi N}{c^2} \frac{\partial \alpha}{\partial Q} \frac{\partial^2 Q^*}{\partial t^2} E_L \tag{2.22}$$

Eqs. 2.21 and 2.22 are the coupled equations describing stimulated Raman scattering. For microscopy application, the input light power at the sample is limited by the sample's damage threshold and the interaction path length is comparable to the focal depth. Therefore, the generated signal is often more than 10 orders of magnitude smaller than the input field and Eqs. 2.21 and 2.22 become decoupled. In CARS, two fields are supplied to drive the Raman vibration and Eq. 2.21 can be used to calculate Q with the knowledge of $\partial\alpha/\partial Q$ which can be inferred from the spontaneous Raman scattering cross section. A third field is used to probe the Raman vibration and the blue shifted anti-Stokes signal can be calculated with Eq. 2.22.

2.3 Optical imaging in microscopy

In this section, the theory of nonlinear incoherent imaging and nonlinear coherent imaging are discussed. Nonlinearity gives rise to a three dimensionally confined excitation volume for the incoherent imaging cases, and the point spread function of the focus can be used to describe the resolution. For coherent imaging, the E

field generated is computed with the Green's function and the longitudinal size of the effective focus is generally longer than the incoherent imaging with the same order of nonlinearity. The theory included in the discussion can be found in many textbooks[64–66].

2.3.1 Incoherent imaging

Fluorescence has the advantages of high sensitivity and can be used to achieve chemical specificity by selective labeling with fluorescent markers. The most commonly used fluorescence imaging method is confocal microscopy. A pin hole at the conjugate focal plane rejects out of focus light and provides three dimensional imaging capabilities. If the intensity of the laser light is low enough to avoid saturation, the signal is linearly proportional to the input light intensity. The disadvantage is that the fluorescent molecules along the beam path are being excited all the time while only the signal from the ones inside the focus is collected. Each fluorescent molecule has a certain life time before it is photo-bleached (typical fluorophores emit $\sim 10^6$ photons before photo-bleaching). It will be ideal if the molecule is only excited when it is being imaged.

Multi-photon fluorescence microscopy is a very good solution to the above problem[67]. The input light source is a near-IR femtosecond pulsed laser. Through two photon or three photon absorption, the effective excitation volume is significantly confined in three dimensions. In other words, it offers automatic sectioning ability. To properly describe this method, the light at the focus of a high numerical aperture (NA) objective lens has to be carefully evaluated. One simple way to describe focusing is to make the paraxial approximation. The assumption is that the transverse wavenumbers (k_x,k_y) are much smaller than k. Under weak focusing condition, the Gaussian function can properly describe the light field at the focus. However with a high NA

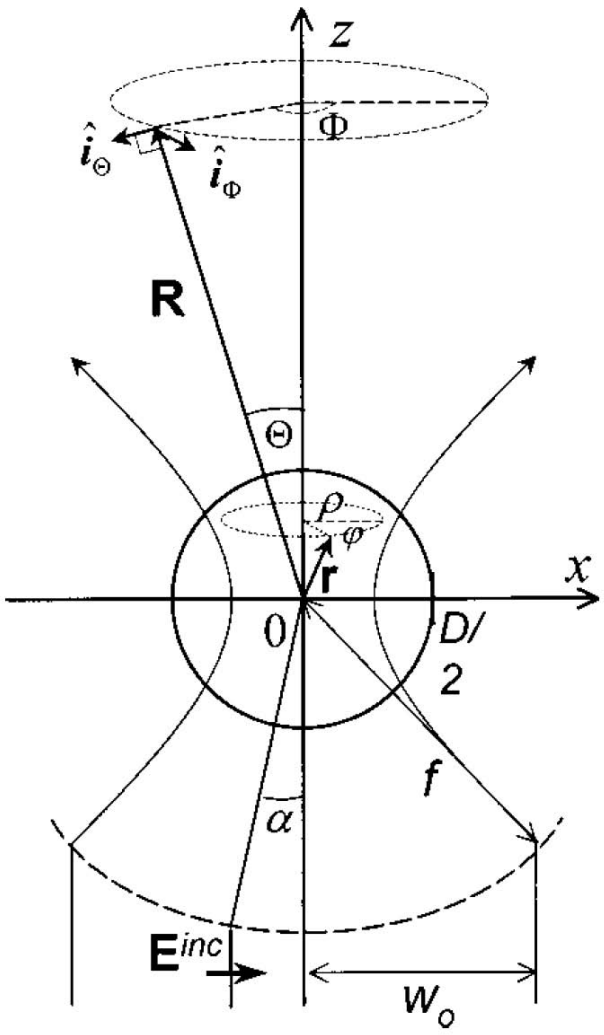

Figure 2.1: Illustration of the focus in spherical coordinates[4]

objective lens the transverse wavenumbers (k_x,k_y) become comparable to k. Hence strict calculation has to be applied.

The angular spectrum representation in Fourier optics can be employed to compute the E field distribution at the focus of a high NA objective lens[66]. The wave propagation in a homogeneous space can be simply described in the spatial spectrum. Suppose the E field at the plane $z = 0$ is $\boldsymbol{E}(k_x, k_y; 0)$. Then the E field in the plane z can be written,

$$\boldsymbol{E}(k_x, k_y; z) = H(k_x, k_y; z)\boldsymbol{E}(k_x, k_y; 0). \tag{2.23}$$

where $H(k_x, k_y; z) = e^{ik_z z}$ is called propagator in reciprocal space. Transferring the spectral representation to a spatial one, we have

$$\boldsymbol{E}(x, y, z) = \int_{-\infty}^{\infty}\int_{-\infty}^{\infty} \boldsymbol{E}(k_x, k_y; 0) e^{i[k_x x + k_y y + k_z z]} dk_x dk_y \tag{2.24}$$

In the limit of $r = \sqrt{x^2 + y^2 + z^2} \to \infty$, the above equation becomes

$$\boldsymbol{E}_\infty(s_x, s_y, s_z) = -2\pi i k s_z \boldsymbol{E}(k s_x, k s_y; 0) \frac{e^{ikr}}{r} \tag{2.25}$$

where $(s_x, s_y, s_z) = (x/r, y/r, z/r) = (k_x/k, k_y/k, k_z/k)$. If the far field($\boldsymbol{E}_\infty$) is given, the Fourier spectrum at $z = 0$ can be expressed as,

$$\boldsymbol{E}(k_x, k_y; 0) = \frac{ire^{-ikr}}{2\pi k_z} \boldsymbol{E}_\infty(k_x, k_y). \tag{2.26}$$

Substituting the above expression into Eq .2.24, we have

$$\boldsymbol{E}(x, y, z) = \frac{ire^{-ikr}}{2\pi} \int\int_{(k_x^2 + k_y^2) \le k^2} \boldsymbol{E}_\infty(k_x, k_y) e^{i[k_x x + k_y y + k_z z]} \frac{1}{k_z} dk_x dk_y \tag{2.27}$$

The focusing of a high NA objective lens can be calculated in two steps: step1, the input far field is refracted at the back aperture of the lens; step2, the theorem discussed above for wave propagating in a homogeneous medium is employed to calculate the E field distribution at the focus. The detailed description of an aplanatic lens can be found in chapter 3.5 of ref.[66]. Due to the symmetry of the objective lens, the calculation is the simplest in spherical coordinates (Fig.2.1 [4, 68]). For simplicity, only the lowest order Hermite-Gaussian mode is considered as the input light at the back aperture of the lens. The incident E field is [66]

$$E_{inc} = E_0 e^{-(x^2 + y^2)/w_0^2} = E_0 e^{-f^2 \sin^2\theta / w_0^2} \tag{2.28}$$

Here f is the focal length of the objective lens. For a specific objective lens, the maximum angle θ_{max} is fixed, which is related to aperture radius R by $R = f \sin\theta_{max}$.

A filling factor can be defined as[66] $f_0 = w_0/f \sin\theta_{max}$. The E field at the focus can be calculated with the following integral.

$$E(\rho, z) = \frac{ikf}{2} e^{-ikf} \int_0^{\theta_{max}} E_{inc} (\cos\theta)^{1/2} \sin\theta (1 + \cos\theta) J_0(k\rho \sin\theta) e^{ikz\cos\theta} d\theta \quad (2.29)$$

Fig.2.2 is the calculated E field distribution at the focus of a NA1.2 water immersed objective lens with filling factor $f_0 = 1$. The generated signal in multi-photon fluorescence inside a spherical volume of radius R is calculated as[66]

$$Signal \propto \sigma_n \int_0^{2\pi} \int_0^{\pi} \int_0^{R} |E(r, \theta, \phi)|^{2n} r^2 \sin\theta dr d\theta d\phi \quad (2.30)$$

where σ_n is the n-photon absorption cross-section. If the E field in Fig.2.2 is used for excitation, the volume integral for $n = 1, 2, 3$ is illustrated in Fig.2.3. The integral converges for two-photon and three-photon absorption, which means the excitation is localized and it guarantees automatic sectioning ability. For the case of one-photon absorption, the out of focus fluorescence molecules along the laser beam path also generate significant signals. Because the direction of fluorescence emission is random (incoherent process), a pinhole aperture at the conjugate focal plane can effectively reject the out of focus signals, as is done in confocal imaging. However, if the emission is coherent (the direction is the same as the excitation beam) as in CARS, the pinhole cannot remove the out of focus signal.

2.3.2 Coherent imaging

Given the E field distribution at the focus, the polarization of the blue or red shifted signal can be calculated by using the coherent Raman scattering theory outlined in the previous section. Because the signal is coherent, a Green's function approach should be used to calculate the signal in the far field[4, 66, 68].

$$\mathbf{E}_{CARS}(\mathbf{R}) = -\frac{4\pi\omega^2}{c^2} \int\int\int_V dV \left(\mathbf{I} + \frac{\nabla\nabla}{k^2} G(\mathbf{R} - \mathbf{r}) \right) \cdot \mathbf{P}_{CARS}(\mathbf{r}) \quad (2.31)$$

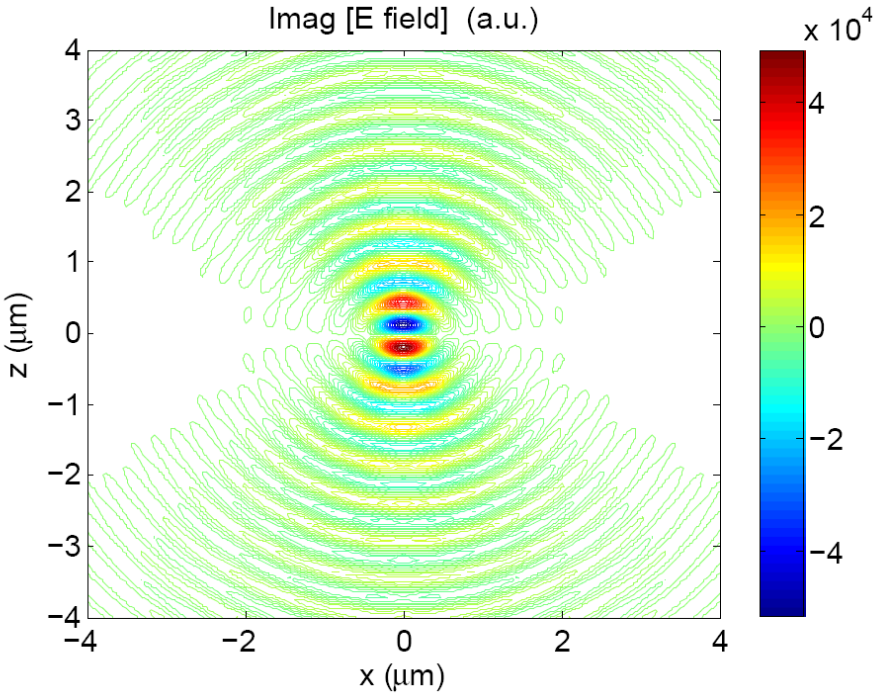

Figure 2.2: The imaginary part of E field at the focus of a NA1.2 water immersed objective lens with filling factor $f_0 = 1$.

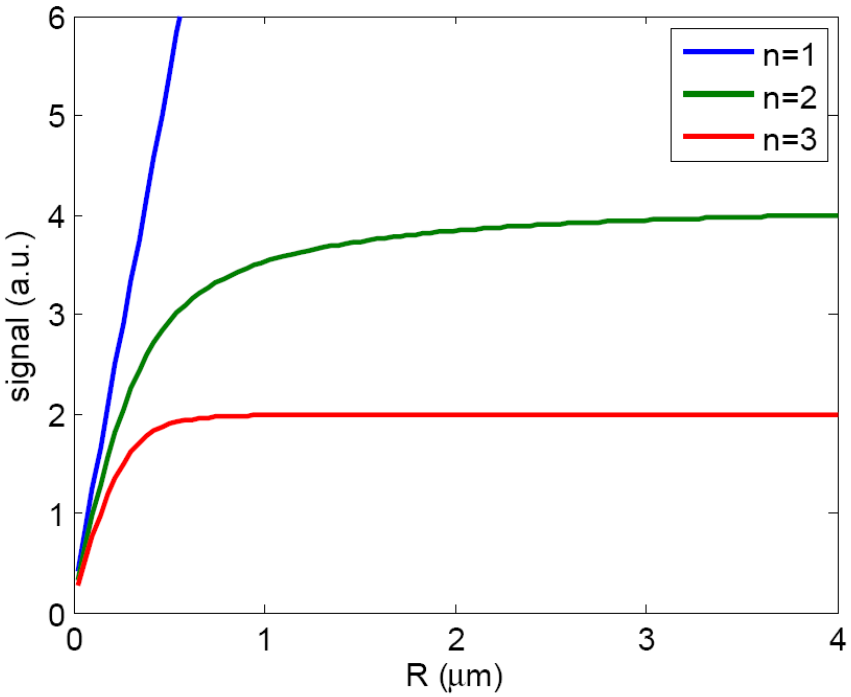

Figure 2.3: The spherical volume integral of the signal as a function of spherical radius R for one-photon, two-photon and three-photon absorption.

$$G(\mathbf{R}-\mathbf{r}) = \frac{e^{ik|\mathbf{R}-\mathbf{r}|}}{4\pi|\mathbf{R}-\mathbf{r}|} \tag{2.32}$$

In the far field, $|\mathbf{R}| \gg |\mathbf{r}|$ and $|\mathbf{R}-\mathbf{r}| \simeq |\mathbf{R}| - \mathbf{R}\cdot\mathbf{r}/|\mathbf{R}|$. The signal can be recast as[4, 68]

$$\mathbf{E}(\mathbf{R}) = -\frac{\omega^2}{c^2}\frac{exp(ik|\mathbf{R}|)}{|\mathbf{R}|}\int\int\int_V dV exp\left(\frac{-ik\mathbf{R}\cdot\mathbf{r}}{|\mathbf{R}|}\right) \tag{2.33}$$
$$\times \begin{bmatrix} 0 & 0 & 0 \\ \cos\Theta\cos\Phi & \cos\Theta\sin\Phi & -\sin\Theta \\ -\sin\Phi & \cos\Phi & 0 \end{bmatrix} \begin{bmatrix} P_x(\mathbf{r}) \\ P_y(\mathbf{r}) \\ P_z(\mathbf{r}) \end{bmatrix} \begin{matrix} \hat{i}_R \\ \hat{i}_\Theta \\ \hat{i}_\Phi \end{matrix}$$

The above procedures can be applied to various coherent nonlinear microscopies, such as harmonic generation, self-phase modulation, and CARS microscopy. As an example, the third order CARS signal generated at the boundary ($z = 0$) of Raman active medium and Raman inactive medium is plotted as a function of the focus position. For comparison, the three photon fluorescence signal is also computed and normalized to the same scale and shown in Fig.2.4. One feature of the coherent signal is that the E field adds up coherently in the far field in contrast to the incoherent intensity summation. The dependence of the third order E field on the input intensity is $I^{1.5}$ instead of I^3, so intuitively, the longitudinal size of the effective focal volume is longer in CARS than in three photon fluorescence. Due to the E field summation along the z axis, the CARS signal has quadratic dependence on the sample's thickness and gives rise to the asymmetry in the z scan, as discussed in the next paragraph.

To clearly show the feature of nonlinear coherent signal generation, the input E field is assumed to be a plane wave and the slowly varying envelope approximation is made to yield the following analytic expression:

$$ik_s\frac{\partial \boldsymbol{E}_s(\boldsymbol{r})}{\partial z} = -4\pi\frac{\omega_p^2}{c^2}\boldsymbol{P}(\boldsymbol{r},\omega_p)e^{-i(k_s-k_p)z} \tag{2.34}$$

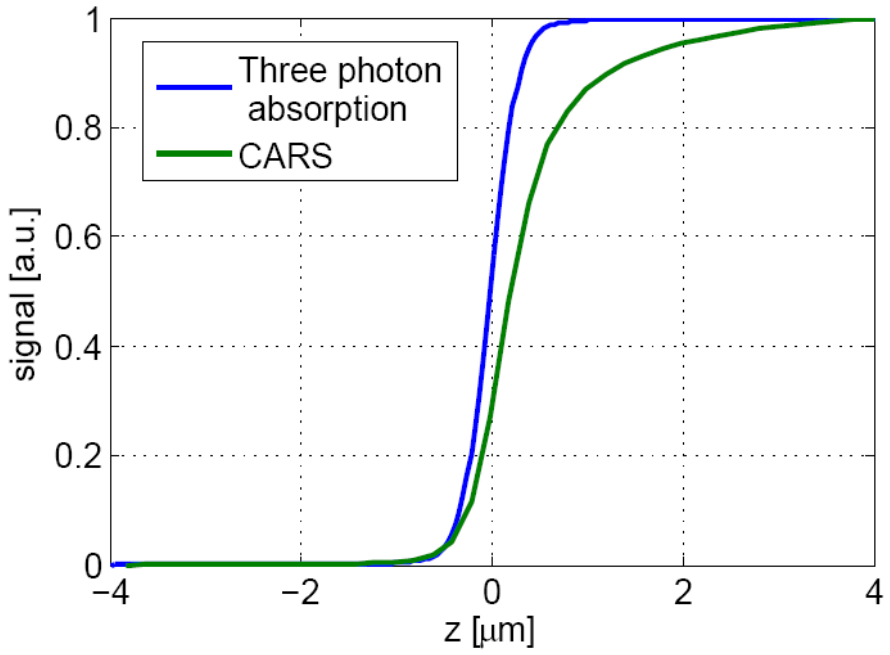

Figure 2.4: CARS signal and three photon fluorescence signal generated at the boundary of Raman active medium and Raman inactive medium as a function of the focus position.

where $\boldsymbol{E}_s$ is the generated signal E field, $\boldsymbol{P}$ is the nonlinear polarization, and k_s and k_p are the wavevectors of the signal field and the polarization field respectively. The signal generated from a sample of thickness L is therefore,

$$\boldsymbol{E}_s = -\frac{4\pi i}{n(\omega_p)}\frac{\omega_p}{c} L\boldsymbol{P}(\omega_p) sinc((k_s - k_p)L/2) e^{-i(k_s-k_p)L/2} \tag{2.35}$$

The *sinc* function in Eq.2.35 gives rise to the phase-matching condition. If there is a phase velocity mismatch between the polarization and the generated signal field due to material dispersion or Gouy phase shift, the overall signal will be significantly reduced. The linear dependence of $\boldsymbol{E}_s$ on sample thickness L makes the signal intensity quadratically dependent on the sample thickness, which leads to the asymmetry in the z scan as shown in Fig.2.4.

2.3.3 Coherent vs incoherent Raman imaging

Spontaneous Raman scattering is an incoherent linear process which does not provide automatic sectioning ability as discussed in previous sections. To acquire three dimensional images, confocal detection has to be applied. The NA of the objective lens not only determines the resolution but also affects the signal collection efficiency because the incoherent signal is randomly scattered to a 4π solid angle. If a uniform sample of thickness L ($L <$ depth of the focus) and molecule density N (number of molecules per unit volume) is imaged by a laser beam of power P and beam area A, the signal collected is

$$P_{Raman} = A \times L \times N \times (P/A) \times \frac{d\sigma}{d\Omega} \times \Omega_{collection} = PLN\frac{d\sigma}{d\Omega}\Omega_{collection} \tag{2.36}$$

The intensity of the coherent signal generated from the same sample is[69],

$$I_{CARS} = \left(\frac{4\pi^2\omega_{CARS}}{c^2 n_{CARS}}\right)^2 |3\chi|^2 I_1 I_2 I_3 \frac{\sin^2 \frac{1}{2}\Delta kL}{(\frac{1}{2}\Delta kL)^2} L^2 \tag{2.37}$$

The wave vector mismatch (Δk) can often be neglected in microscopy applications because on the one hand the wavelength difference between the signal and the input light is much smaller than harmonic generation, and on the other hand the length of the interaction is short ($\sim \lambda$). So the average power of the signal collected is,

$$\begin{aligned} P_{CARS} = I_{CARS}A &= \left(\frac{4\pi^2\omega_{CARS}}{c^2 n_{CARS}}\right)^2 |3\chi|^2 L^2 A \frac{P_1 T}{A\tau}\frac{P_2 T}{A\tau}\frac{P_3 T}{A\tau}\frac{\tau}{T} \\ &= \left(\frac{4\pi^2\omega_{CARS}}{c^2 n_{CARS}}\right)^2 |3\chi|^2 L^2 \frac{P_1 P_2 P_3 T^2}{A^2\tau^2} \end{aligned} \tag{2.38}$$

where $1/T$ is the repetition rate of the laser system, ω_{CARS} is the angular frequency of CARS signal, n_{CARS} is the refractive index of CARS signal, $P_{1,2,3}$ are the powers of the three laser beams, and τ is the duration of the optical pulses. The term $|3\chi|^2$ is related to the spontaneous Raman scattering cross section $d\sigma/d\Omega$ by[69]

$$|3\chi|^2 = \frac{\left(\frac{2Nc^4}{\hbar\omega_s^4}\Delta\frac{d\sigma}{d\Omega}\right)^2}{4\Delta\omega^2 + \Gamma^2}, \tag{2.39}$$

where N is the density of the molecules, ω_s is the Stokes angular frequency at which the Raman scattering cross section $d\sigma/d\Omega$ is measured, Δ is the population difference between the ground and excited vibrational states, $\Delta\omega$ is the detuning ($\Delta\omega = \omega_\upsilon - (\omega_1 - \omega_2)$), and Γ is the dephasing rate. For coherent Raman scattering, the signal dependence on the pulse duration is not actually τ^{-2} because the Raman resonance acts as a bandpass filter in the spectral domain. The τ^{-2} dependence is valid only when the pulse duration is much longer than the dephasing time T_2 (the laser bandwidth is narrower than the Raman resonance). The T^2 dependence indicates that laser systems of low repetition rate should be used for nonlinear microscopy. However previous studies[70, 71] on photo-damage in biological samples indicate a nonlinear dependence on the input intensity, $Damage \propto I^n$ where $n \sim 2.5$ for femtosecond pulses, which negates the benefit of using low repetition rate systems.

By using the following empirical formula for the focus size [72], the signal dependence on NA can be evaluated.

$$\omega_{xy} = \begin{cases} \frac{0.320\lambda}{NA} & \text{if } NA \leq 0.7 \\ \frac{0.325\lambda}{NA^{0.91}} & \text{if } NA > 0.7 \end{cases} \tag{2.40}$$

$$\omega_z = \frac{0.532\lambda}{(n - \sqrt{n^2 - NA^2})} \tag{2.41}$$

where ω_{xy} and ω_z are the lateral and axial $1/e$ radii of the illumination point spread function (IPSF) (in the reference [72], there is a $\sqrt{2}$ for evaluating IPSF^2). Conversion to FWHM can be achieved by multiplication by $2\sqrt{ln2}$. The normalized signal dependence is calculated and shown in Fig.2.5. The trend for both the incoherent and the coherent signal is that the signal decreases at higher NA. For the incoherent signal, the increased NA improves the signal collection efficiency. However the depth of the focus decreases faster, which reduces the overall signal. For the coherent signal, the reduction on the focal depth is compensated by the reduced beam area,

which gives rise to the slow variation of the signal at the low NA region. At the high NA region (water immersed lens), the variation on the focal depth becomes more pronounced and the signal decreases as rapidly as the incoherent signal.

Another important parameter is the density of the molecules (N). The incoherent signal has linear dependence on (N) in contrast to the quadratic dependence of the coherent signal, suggesting the reduced advantage of the coherent method at low molecule concentrations. Which method is favorable in real applications however depends on the sample's damaging threshold, the nonlinearity in the photo-damage mechanism, and the absolute value of the signal generated by each method instead of the dependence curves. Experiments were performed to compare the absolute signal strength under imaging conditions, which is presented in **Chapter 6**.

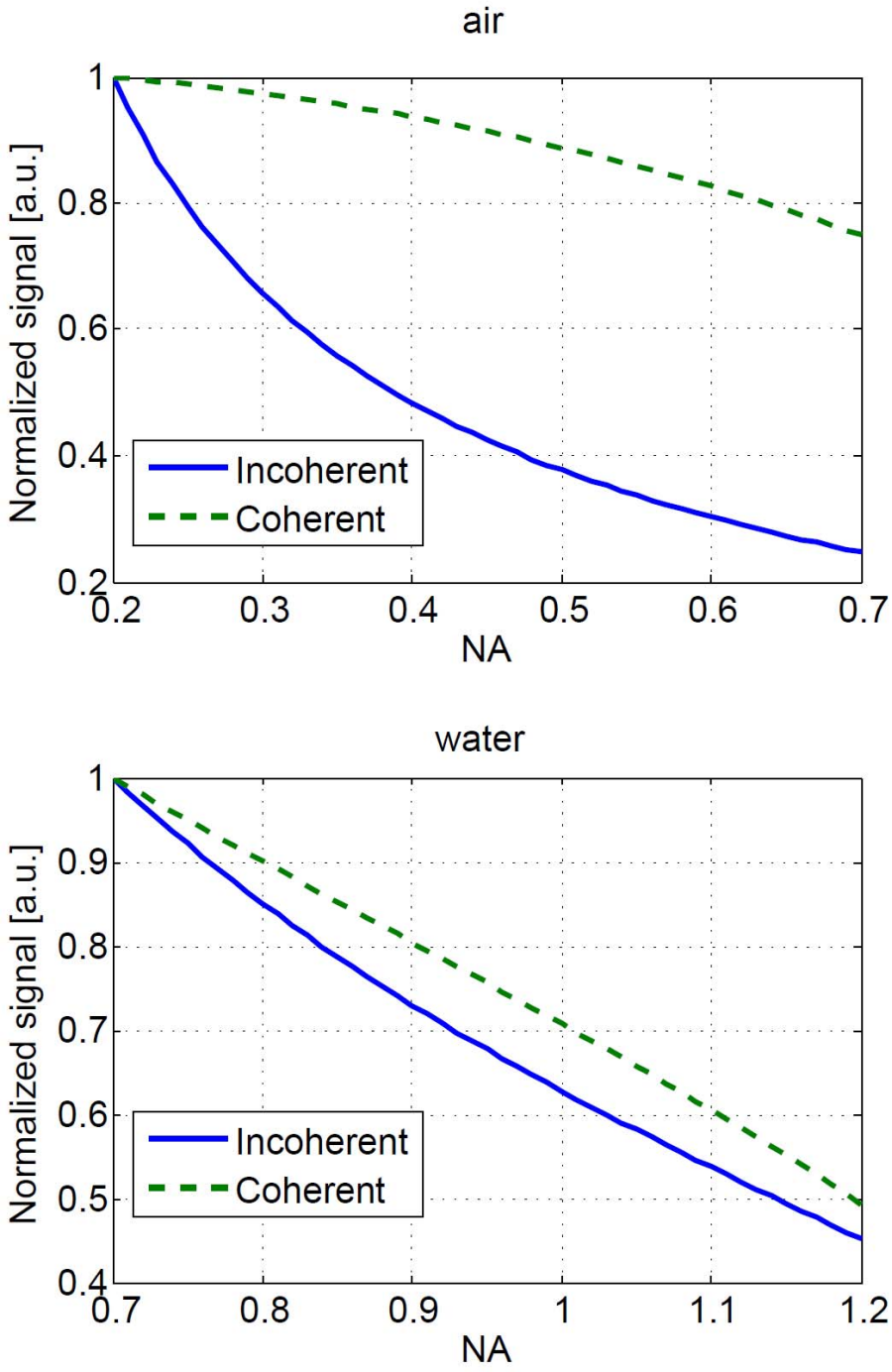

Figure 2.5: The incoherent and coherent signal dependence on the NA of an air objective lens and a water immersed objective lens.

CHAPTER III

Fourier transform CARS microscopy

3.1 Introduction

In this chapter, the theory, implementation and imaging applications of Fourier transform CARS (FTCARS) are presented. As a new version of the time domain coherent Raman method, FTCARS allows effective removal of the NR background signal and acquisition of high resolution spectra within the fingerprint regime. With sub 20 fs laser pulses, FRCARS can be easily combined with two photon fluorescence and self-phase modulation imaging. The robustness in rejecting the NR background, the simplicity in experiment setup, and multi-modality makes FTCARS a very promising tool for nonlinear microscopy.

3.2 Motivation of time domain coherent Raman imaging

Under a coherent driving force, nuclear motion gives rise to blue shifted CARS and red shifted CSRS signals via four wave mixing processes. Similarly, electronic contributions can also generate either blue or red shifted signal, giving rise to NR background. The major difference between nuclear and electronic contributions is the time scale: the electronic contribution is instantaneous compared with the nuclear contribution. If we resolve the signal in the time domain, the two contributions can be easily separated.

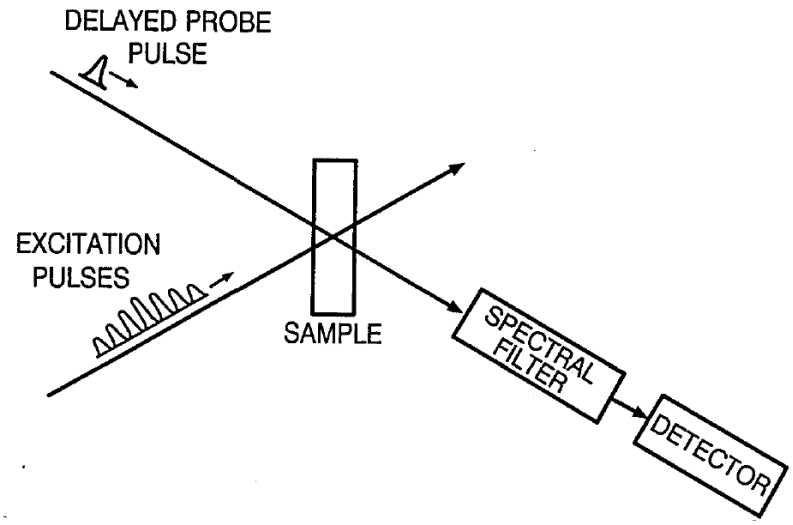

Figure 3.1: Experiment setup of ISRS. [5]

A well known time domain coherent Raman technique is pump-probe impulsive Raman scattering (ISRS) [39, 40]. Impulsive scattering means that the excitation duration is much shorter than the period of the vibrational mode. The excitation is too fast to be followed by the vibration. Short laser pulses transparent to the sample are used to excite and probe coherent Raman oscillations. According to the Nyquist sampling theorem, the pulse duration needs to be shorter than half of the period of molecular vibration. For resolving a Raman mode of $1000cm^{-1}$, a pulse shorter than 17fs is required. From the point of view of effective excitation, a short pump pulse is required: the vibration excited by the front of the pulse will be canceled by the vibration excited by the rear part of the pulse if its duration is longer than half of the vibrational period.

In impulsive stimulated Raman scattering, the first pulse initiates the molecular vibrational coherences. At a certain controllable time delay, a second pulse arrives and interacts with the sample. Depending on the time delay, the vibrational coherence excited by the second pulse may be in phase or out of phase with that excited by the first pulse. As a result, the second pulse may lose or gain energy from the

molecular vibration. In the spectral domain, the second pulse may be red or blue shifted. Detecting the blue edge or red edge can resolve the molecule's oscillation.

The difficulty for converting ISRS to microscopy applications is the non-collinear beam geometry(Fig.3.1) which causes reduced spatial resolution and focus abberation when in use with a high numerical aperture objective lens. A time domain method with collinear geometry and high signal contrast is desired for coherent Raman microscopy applications.

3.3 Experiment setup

Fourier transform CARS (FTCARS) is a time domain coherent Raman technique with a collinear geometry. The setup and energy diagram of FTCARS are shown in Fig.3.2 (a) and (b) respectively. As in ISRS, the pump pulse generates Raman coherences in all the modes within the pulse bandwidth, while the second pulse probes the coherences. Both Stokes and anti-Stokes fields are generated, and the anti-Stokes field is selected via spectral filtering. Recording the anti-Stokes signal as a function of the inter-pulse delay, the CARS spectrum can be obtained by Fourier transforming the time domain signal. The NR signal can be removed by windowing it out in the time domain.

A 12fs pulse from a Ti:sapphire oscillator is sent into a balanced Michelson interferometer to generate two pulse replicas. The two pulses are separated by a time delay controlled by a high precision DC motor with 7nm resolution. The DC motor is controlled with a homemade system composed of a digital signal processor and a high speed signal amplifier. The pulse pair is sent through a sharp edge long-pass filter centered at 735nm (Omega Optical, AELP735) to remove the blue edge of the laser pulses. A pair of chirped mirrors are used to compensate the total dispersion

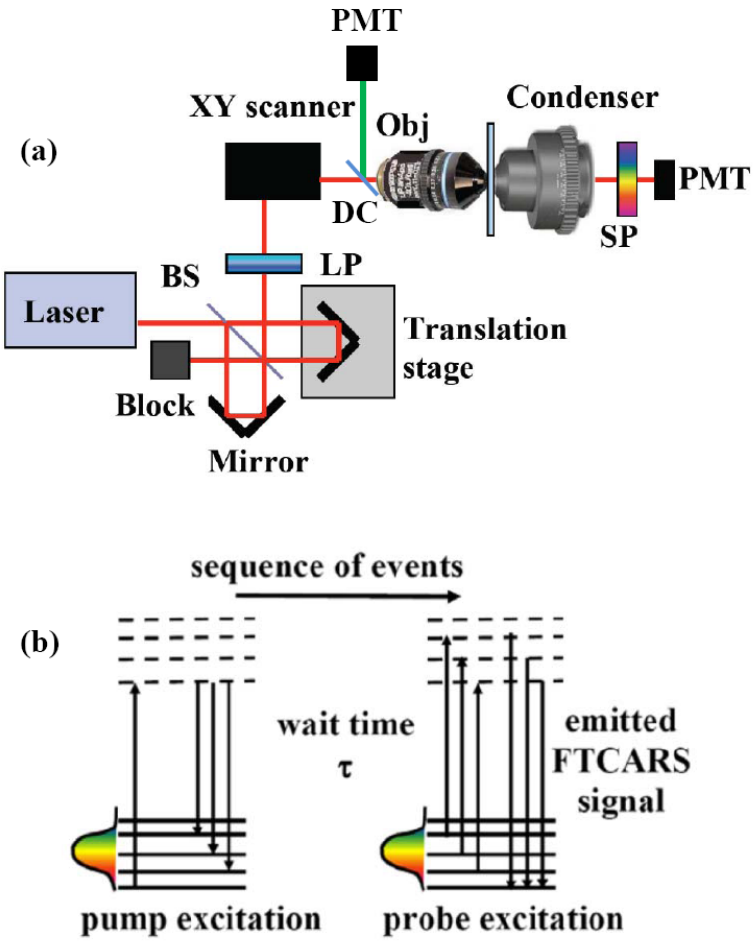

Figure 3.2: (a) Experiment setup of FTCARS. BS: beam splitter; Obj: objective lens; LP: long-pass filter; SP: short-pass filter, PMT: photomultiplier tube, DC: dichroic beam splitter. The DC before the objective collects fluorescence in the epi direction for simultaneous CARS and fluorescence imaging. (b) Energy diagram of FTCARS.

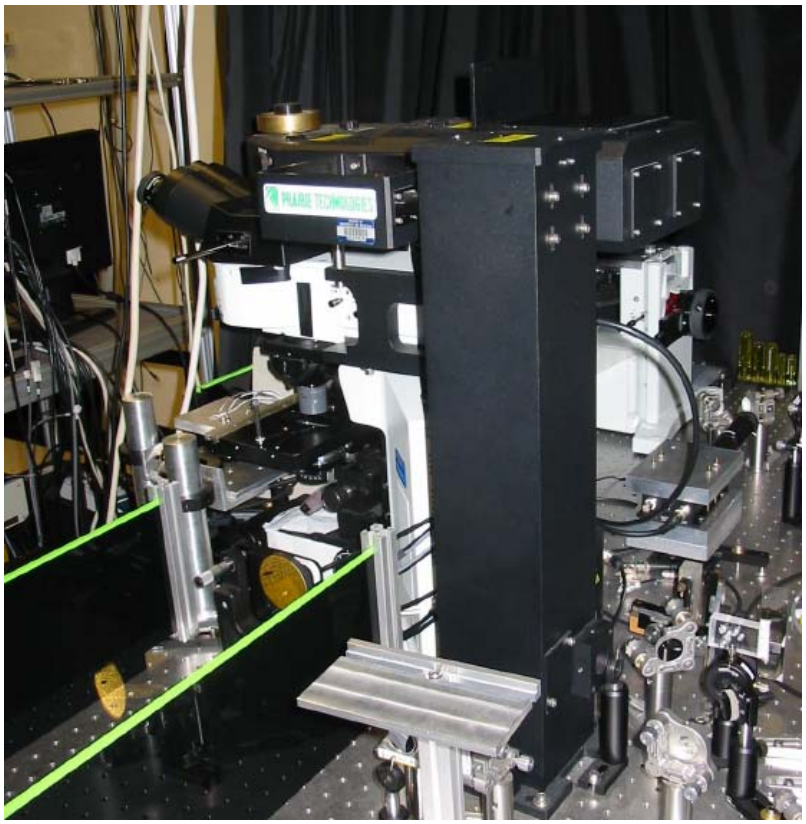

Figure 3.3: Photo of the laser scanning microscope (Prairie Technologies).

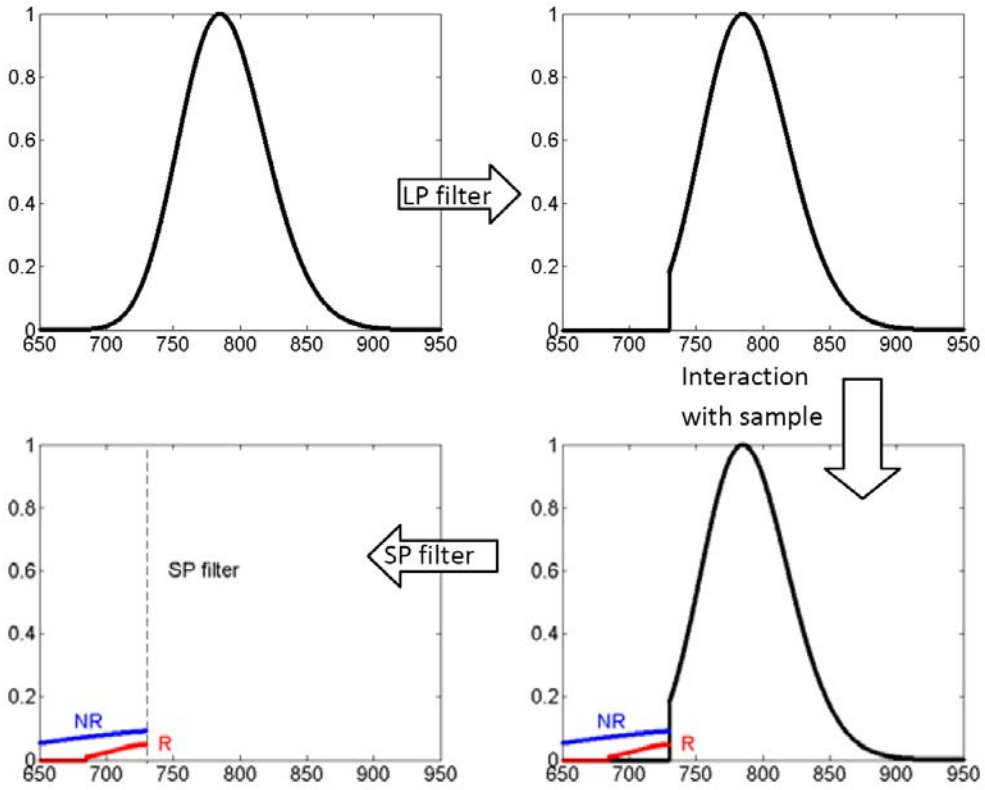

Figure 3.4: Spectral filtering method: the blue edge of the input pulse is removed by a long pass filter. The interaction with the sample generates blue shifted CARS and NR signals. A short pass filter is used to block the laser light and let the blue shifted signal enter the detecor.

caused by beam splitters, filters, an achromatic lens inside the laser scanning microscope, and the objective lens. The entire system dispersion is $4400 fs^2$. After the dispersion compensation, the pulse pair is sent into a laser scanning microscope (Prairie Technologies, Fig.3.3). After interaction with the sample, the beam is collimated and sent through a short-pass filter (Omega Optical, AELP 725) to block the input laser light and let the blue shifted signal enter a PMT detector. This spectral filtering method is illustrated in Fig.3.4. Both the blue shifted CARS signal and the red shifted CSRS signal can be used. If the sample fluoresces, anti-Stokes signal is the clear choice for avoiding the strong fluorescence background. Otherwise choosing CARS over CSRS is due to the much higher quantum efficiency of the detector at

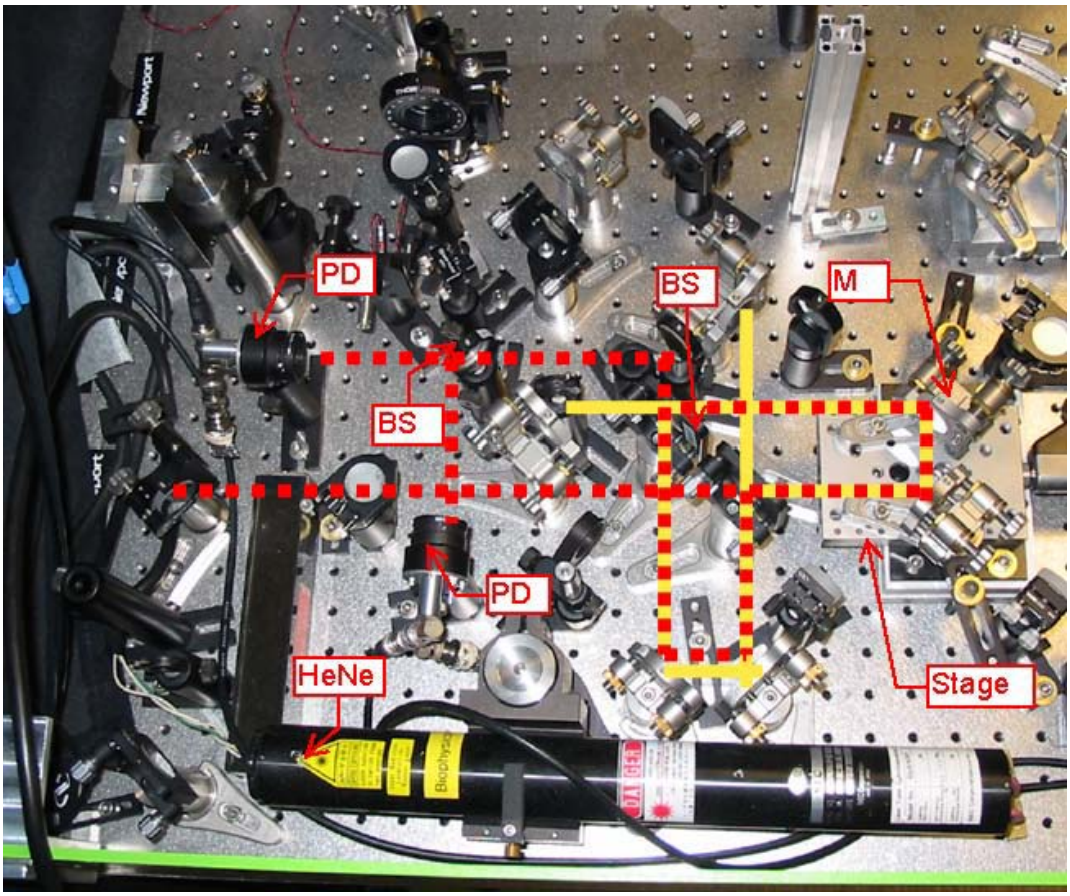

Figure 3.5: Michelson interferometer setup. The red dotted line is the path of the reference beam (633nm) and the yellow solid line is the path of the 12fs pulses. PD: Si photodiode, BS: beam splitter, M: mirror, Stage: translation stage driven by a DC motor of 7nm resolution, HeNe:Helium-neon laser (reference laser).

700nm compared to at 900nm.

3.4 Stability and position accuracy

Accurately measuring the time delay between the two laser pulses is very important. The error in time delay measurement can cause both error in spectral peak position and distortion of the spectral line shape.

The key element of this collinear time domain method is the Michelson interferometer. Fig.3.5 is a photo of the experimental setup. To minimize overall dispersion, a thin beam splitter with a dielectric coating is used with the coating on one side

of the substrate. Two identical beam splitters are arranged so that both beams traverse the glass substrate only once. Though the Michelson interferometer is composed of six isolated optical elements (two beam splitters and four mirrors), the short term stability is better than 50nm. This was determined by a spectral interferometry measurement[73]. Fig.3.6(a) shows 100 nonresonant signal spectra generated by two input pulses at a time delay of $\sim 290fs$ with a data acquisition time for each spectrum of 100 msec. All the spectra are taken over a time span of 15 seconds. Fourier transform of the spectral interferograms allows a straightforward phase stability analysis. The absolute value of the Fourier transform of the interferogram, and the phase at $t = 290fs$ are shown in Fig.3.6(b) and (c). The phase drift of 0.2 rad over 15 seconds can be inferred from the phase plot.

The linear stage is driven by a DC motor that has an encoder with 7nm resolution. However, the motor's backlash is on the order of a micron. To actively monitor the optical path difference and also remove backlash error, a HeNe laser is sent into the interferometer from the other port. In Fig. 3.5, the yellow solid line is the path of the pulsed laser and the dotted red line is the path of the Helium-neon (HeNe) laser. As we can see on the photo, the optical path of the HeNe beam overlaps with the Ti:sapphire path, allowing it to be used to accurately track position via fringe counting. The accuracy can readily reach $\lambda/40$. At 633nm, this means that the position accuracy is better than 16nm. The Raman period of a $1000cm^{-1}$ mode is 33.3fs $(1/(1000 * 0.00003))$. In free space, this corresponds to a $10\mu m$ optical path, which means that our position accuracy is close to three orders of magnitude greater than the Raman period, allowing us to neglect the noise due to position measurements in our signal to noise ratio analysis.

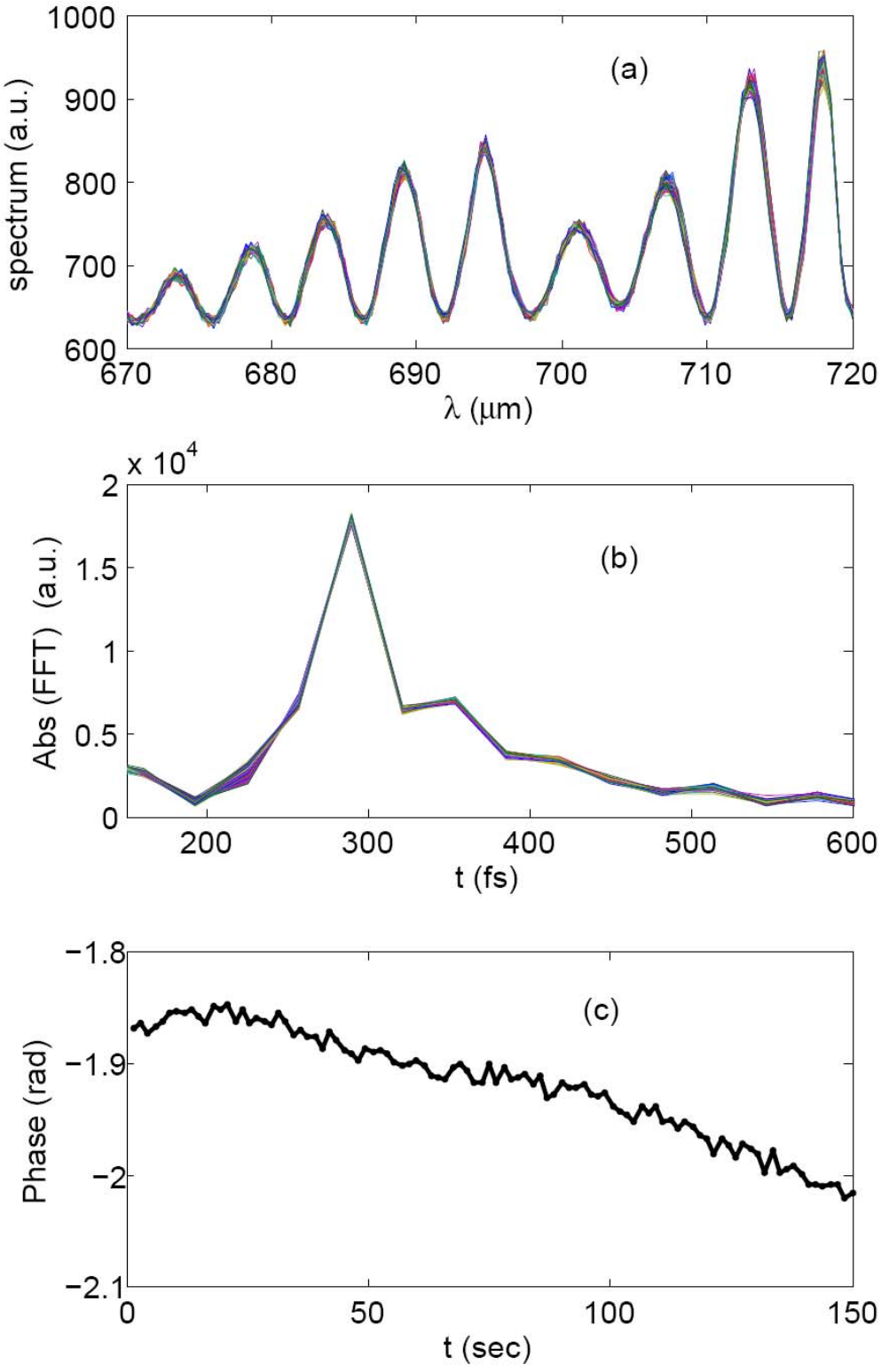

Figure 3.6: (a) NR signal spectral interference. Data acquisition time for each spectrum is 100msec. 100 spectra taken over 15 seconds are overlapped in the plot. (b) Absolute value of the Fourier transform of the interferogram. (c) The phase variation at 290 fs position over 150 seconds.

3.5 Signal analysis

If the two excitation pulses in FTCARS are well-separated in time, the detected signal intensity can be expressed as $I = I_1 + I_2$, where I_1 and I_2 are the signal intensities generated by pulse 1 and pulse 2 respectively. I_1 consists of resonant and NR contributions from pulse 1 and is independent of the time delay. I_2 has three components: NR signal I_{2nr} generated by pulse 2, resonant signal I_{2r} generated by pulse 2 only, and the resonant signal I_{r12} from coherences created by pulse 1 and probed by pulse 2. This latter component is the only time-dependent term. Note that we have neglected the NR signal generated by the combination of pulses 1 and 2 since this term only contributes during their temporal overlap. The three I_2 components interfere with each other due to their mutual coherence and time coincidence at the detector. The first two components have a fixed relative phase difference, allowing us to treat them as a single LO component I_{local}. Thus the overall FTCARS signal can be written as:

$$I(\tau) = I_1 + I_{local} + I_{r12} + 2c\sqrt{I_{local} I_{r12}} \cos\left(\phi_{r12}(\tau) - \phi_{local}\right) \tag{3.1}$$

where $c \leq 1$ is a constant accounting for the fact that the resonant and NR signals have different amplitude and phase profiles and hence may not have perfect interference. The cosine term indicates the need for relative phase stability between the signal and LO. Because $\phi_{r12}(t)$ is derived from the phase of $\chi_r^{(3)}(\tau)$ and $\sqrt{I_{r12}} \propto \left|\chi_r^{(3)}(\tau)\right|$, the last term in Eq.3.1 directly yields $\chi_r^{(3)}(\tau)$ to within a constant phase factor. The Fourier transform of $I(\tau)$ yields the resonant CARS spectrum, provided the NR contribution within the pulse overlap region is windowed-out. The first two terms in Eq.3.1, which carry no information, generate background noise in the measurement. As will be discussed in the next chapter, I_{local} needs to be large

enough to lift the signal above the background noise floor.

3.6 FTCARS spectroscopy

Fig 3.7 is the time domain data of pyridine measured with 43 mW power in each beam. The laser is focused to a spot of $30\mu m$ in diameter with a 5cm lens. The strong peak at $t = 0fs$ is due to the NR signal. This NR signal is present only when the two pulses are overlapped in time. The sharp cutting in the spectral domain and the presence of third order material dispersion give the pulses a long tail which lasts to $\sim 200fs$. Fourier transforming the data at $\tau >$250fs yields a clean spectrum that shows the dominant peaks at 991cm^{-1} and 1030cm^{-1} as reported in the spontaneous Raman spectrum[74]. Also shown is the simulated FTCARS signal based on the theory discussed in [47].

3.7 Power dependence measurement

Eq.3.1 shows that the time domain signal oscillation is proportional to both the amplitude of the local field and also the resonant Raman field. Because the local field is generated through a third order nonlinearity, the signal is linearly proportional to the intensity of the first pulse and quadratically proportional to the intensity of the second pulse (Eq 3.2), which is opposite to the conventional spectral domain method. In the conventional spectral domain method, the pump beam is also used as the probe beam($E_{CARS} = E_{pump}E^*_{Stokes}E_{probe} = E^2_{pump}E^*_{Stokes}$), which indicates quadratic and linear power dependence on the pump and the Stokes beam respectively. To verify the signal power dependence, linear neutral density filters are placed in both arms of the Michelson interferometer to control the incident power. The measurement result is shown in Fig 3.8. Linear fit on the double log plot yields a slope of 1.18 for the first pulse and 2.16 for the second pulse, which indicate linear and quadratic power

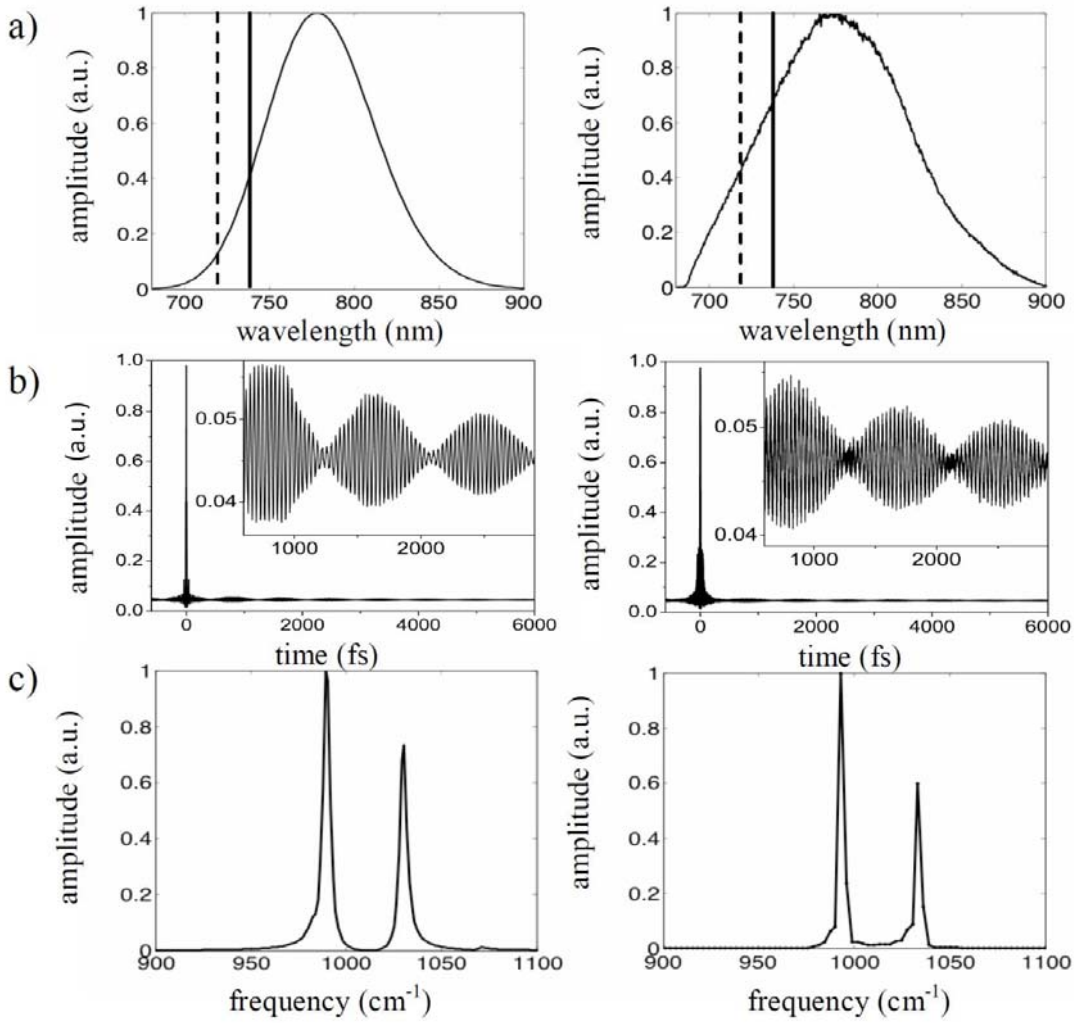

Figure 3.7: Simulated (left) and experimental (right) FTCARS results. a) Spectrum of the pump and probe pulse. The locations of the long pass (dashed) and short pass (solid) filters are also indicated. b) Time domain FTCARS signal for pyridine including the dominant CARS modes at 991 cm^{-1} and 1030 cm^{-1}, with smaller peaks at 983 cm^{-1} and 1070 cm^{-1}. The actual scan length was 12 ps, providing 3 cm^{-1} resolution. c) Fourier transform of the oscillatory part of the time domain data for τ >250fs yields the CARS spectrum.

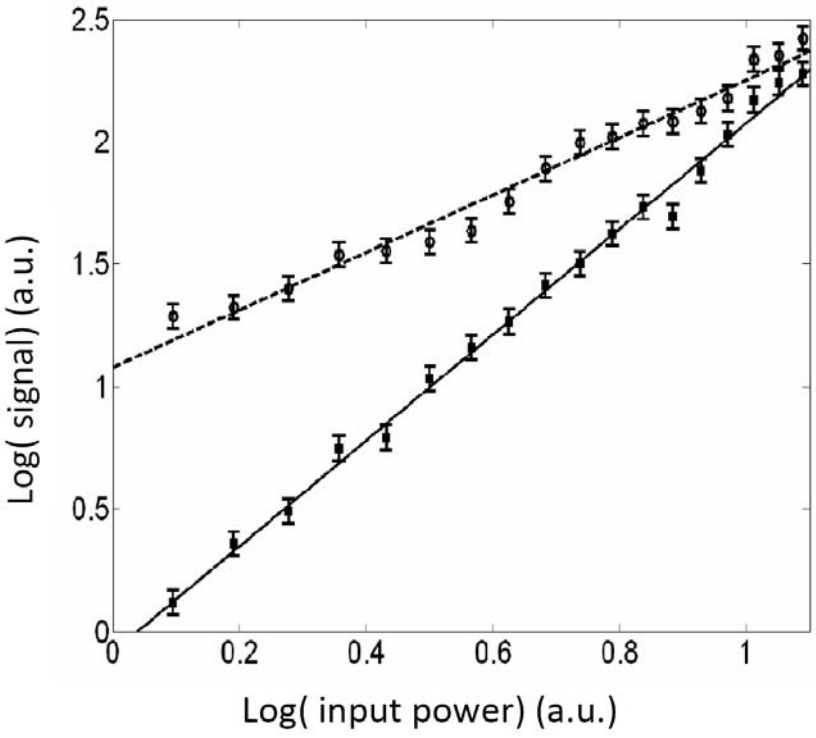

Figure 3.8: Power dependence measurement on 2propanol. Linear fit indicates slopes of 1.18(first pulse) and 2.16(second pulse).

dependence as expected.

$$Signal \propto \sqrt{I_{local} I_{r12}} \propto E_2^3 E_1^2 E_2 \propto I_1 I_2^2 \tag{3.2}$$

3.8 Concentration dependence measurement

The 820cm^{-1} mode of 2-propanol diluted in water was measured at different concentrations. A NA 0.4 air objective lens was used to focus 36mW laser light into a fused silica cell with 1mm path length. The experimental result is shown in Fig.3.9 and fitted with a quadratic function which passes the origin. As expected for coherent signals, the signal amplitude has a quadratic dependence on the density of the molecules, which is different from the linear dependence of incoherent signals such as spontaneous Raman scattering and fluorescence. With ∼20sec data acquisition time, the signal from 1% 2-propanol solution ($\sim 5 \times 10^8$ molecules) can be detected. Tighter focusing with NA 1.2 objective lens is expected to increase the sensitivity to $\sim 10^7$ molecules under the same experimental condition.

3.9 Spectral filtering and excitation considerations

To explore the dependence of the FTCARS signal amplitude on several experimental parameters, we calculate the time-domain FTCARS signal. The relative size of the resonant to NR background, is set by matching the resonant to NR signals calculated for FTCARS to the measured ratio determined from FTCARS data on 2-propanol. The spectral resolution is set to 10cm^{-1}, corresponding to a maximum time delay of 3ps. We assume transform-limited input pulses of 12fs in duration, centered at 790nm and perform spectral filtering with a constant separation of 5nm between long and short pass filters. As with the experimental data, we window out the first 300fs of the time-domain data before taking the Fourier transform to yield

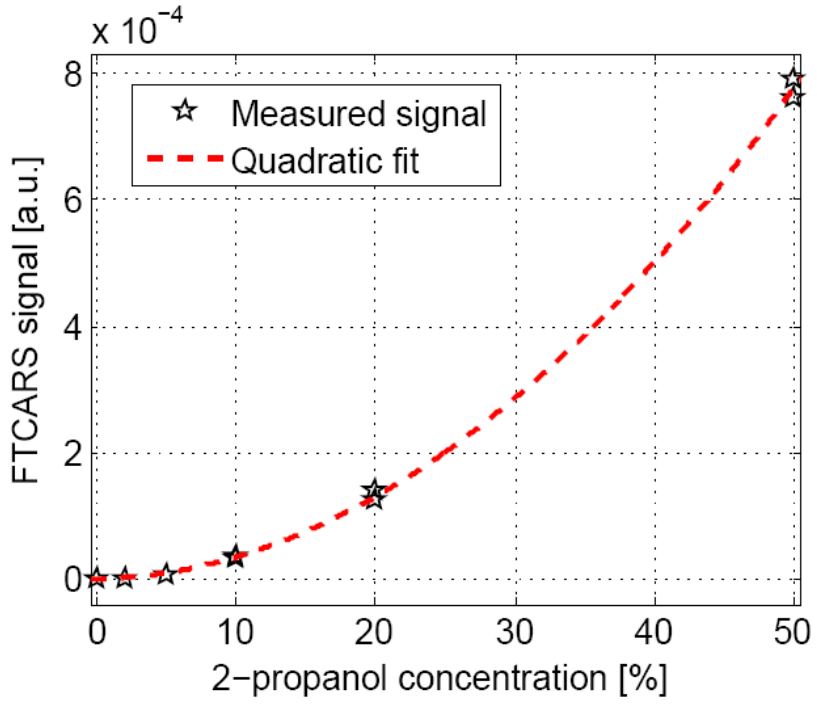

Figure 3.9: FTCARS signal of the 820cm^{-1} mode of 2-propanol at different concentrations. The experimental data is fitted with a quadratic function which passes the origin.

the FTCARS spectrum. We vary several parameters to study their effect on the FTCARS signal: the long pass filter edge wavelength, the power ratio between the two pulses, and the frequency of the Raman mode excited. The results are summarized in Fig.3.10. As expected, the calculations show that the resonant signal level is reduced for higher frequency modes, since fewer frequency combinations can excite the given mode. However, this is partly compensated by the fact that the larger blue shift of the higher frequency modes means that the signal passes the combination of long pass and short pass filters more efficiently than for lower frequency modes, resulting in a resonant signal level that is almost flat over the entire 600cm^{-1}, demonstrating the very broad effective bandwidth of the FTCARS method. The choice of long pass filter wavelength also influences the relative efficiency with which different modes can be excited. The signal is linearly dependent on pulse 1 and quadratically depen-

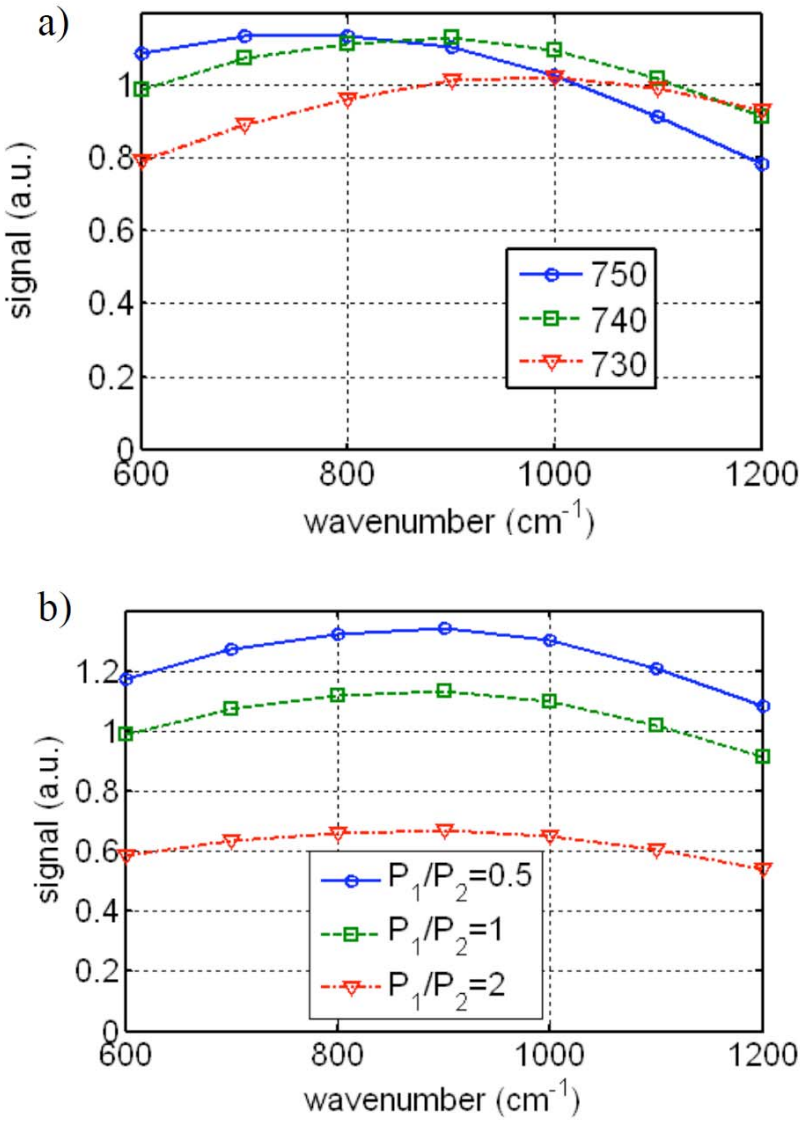

Figure 3.10: (a) Dependence of the FTCARS resonant signal amplitude on the frequency of the CARS mode for different choices of the longpass filter wavelength. (b) Dependence of the FTCARS resonant signal amplitude on the frequency of the CARS mode to be excited. Several different relative power ratios between pulses 1 and 2 (P_1/P_2) are shown.

dent on pulse 2, with the quadratic dependence arising from interference between the resonant signal and the NR background generated by pulse 2. Thus as expected, the second pulse should be stronger than the first pulse for optimum excitation, as shown in Fig.3.10(b).

3.10 Imaging applications

For imaging applications, the laser beam is sent to a pair of galvanometer mirrors(X Y mirrors) before going through the objective lens. The laser beam is raster scanned along a line on the sample at 1kHz (X mirror) while the time delay between the two laser pulses is varied slowly at 0.5Hz. The other mirror (Y mirror) moves the laser spot to a different line at the end of each time delay scan. The motion of the two mirrors and the time delay motor has to be synchronized carefully. A c++ code is used to program a DSP for motor control and computer interfacing. A matlab program with graphical user interface is employed to control the two scanning mirrors and synchronize the experiment. A multifunction data acquisition card (NI PCI-6110) acquires data simultaneously from three channels. One channel is for the single detector (PMT Hamamatsu R636-10) and the other two are for the HeNe fringe tracking measurement.

In Fig.3.11 we show FTCARS images of a sample of 15 μm polystyrene beads imaged with 4 mW of power in each pulse. Fig.3.11(a) shows the NR signal obtained from a single pulse. While the chemical contrast provided by NR signals is limited we note that it may also find applications for noninvasive imaging[18, 75]. In Fig.3.11(b) we show spectrally resolved images of a single bead, acquired with 16 cm^{-1} spectral resolution and 7 ms exposure time per pixel. Higher spectral resolution is readily obtained by scanning longer time delays. We show the corresponding FTCARS

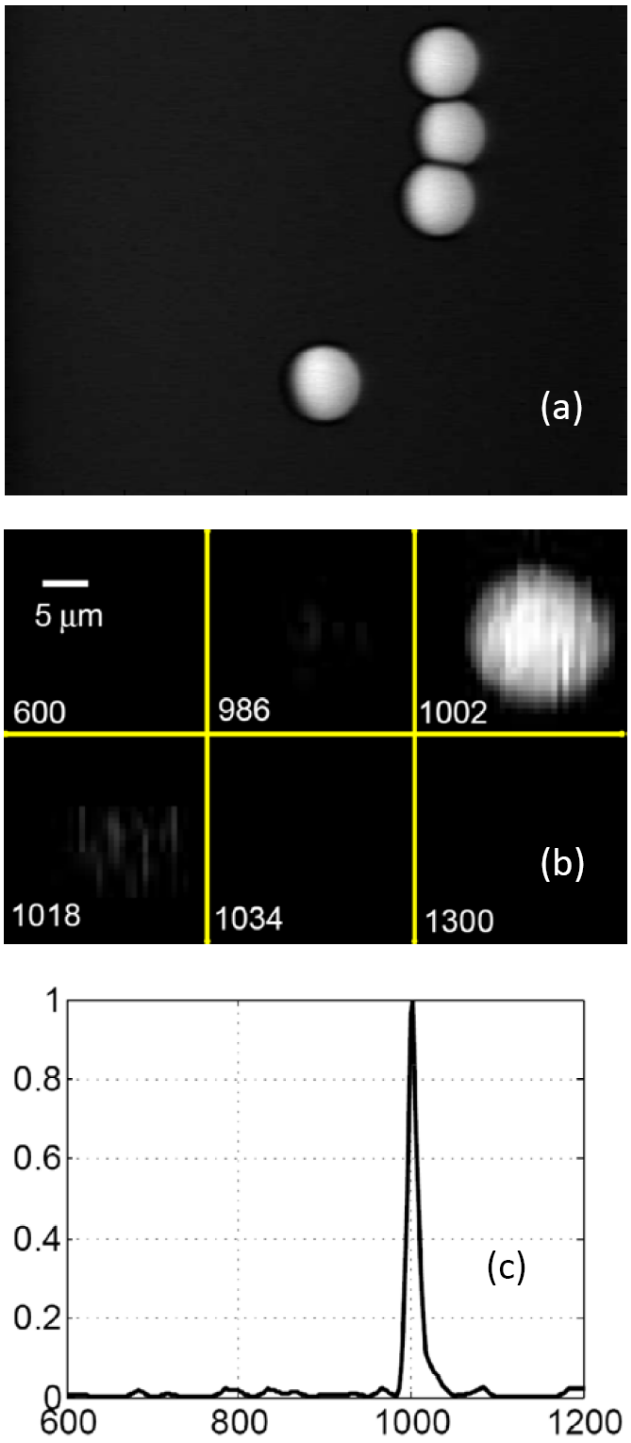

Figure 3.11: (a) NR background signal image of 15μm polystyrene beads in water. (4 mW in each beam, 512×512 pixels, 10μs exposure time per pixel) (b) FTCARS image of a single polystyrene bead from the sample shown in (a) (4 mW in each beam, 36×36 pixels, 7ms exposure time per pixel, spectral resolution of 16 cm^{-1}) (c) FTCARS spectrum from a single pixel within the bead in image (b).

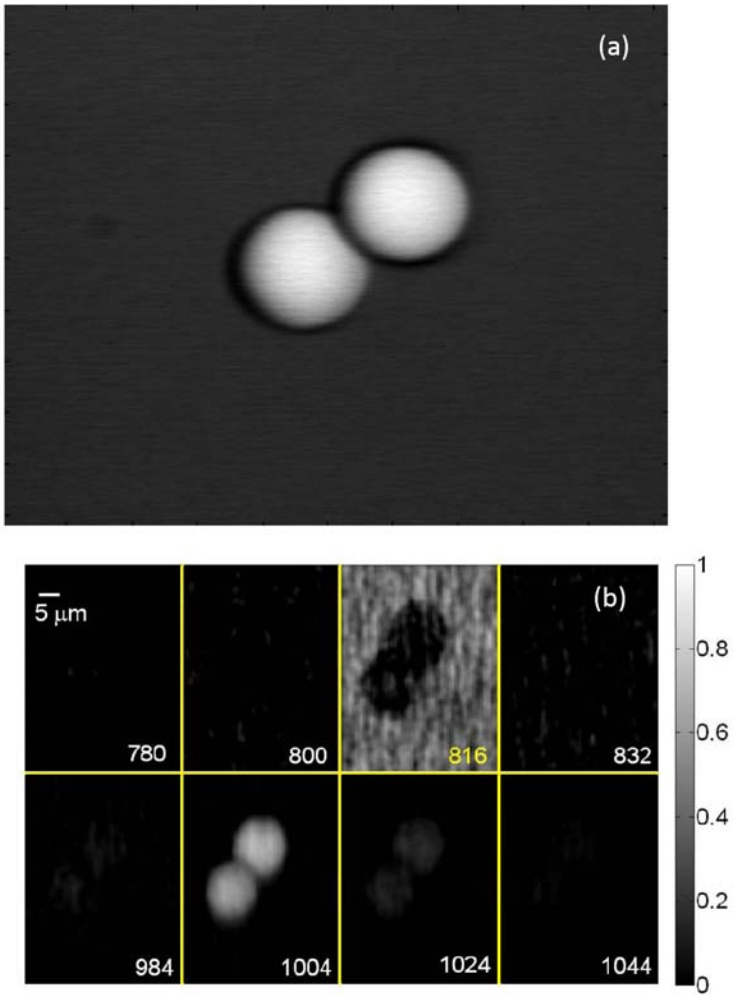

Figure 3.12: (a) Nonresonant image of 15 μm polystyrene beads embedded in PMMA (b)FTCARS images of the sample shown in (a). The image is acquired with 4 mW power in each beam with a data acquisition time of 7 ms/pixel. The spectral resolution is 16 cm^{-1}. The top row of images show a maximum contribution from the PMMA near 820 cm^{-1} while the lower row corresponds to the dominant polystyrene peak near 1000 cm^{-1} in agreement with the reported Raman spectra [6]. The upper row has been multiplied by a factor of 4 to show the weaker PMMA signal on the same scale as the polystyrene bead.

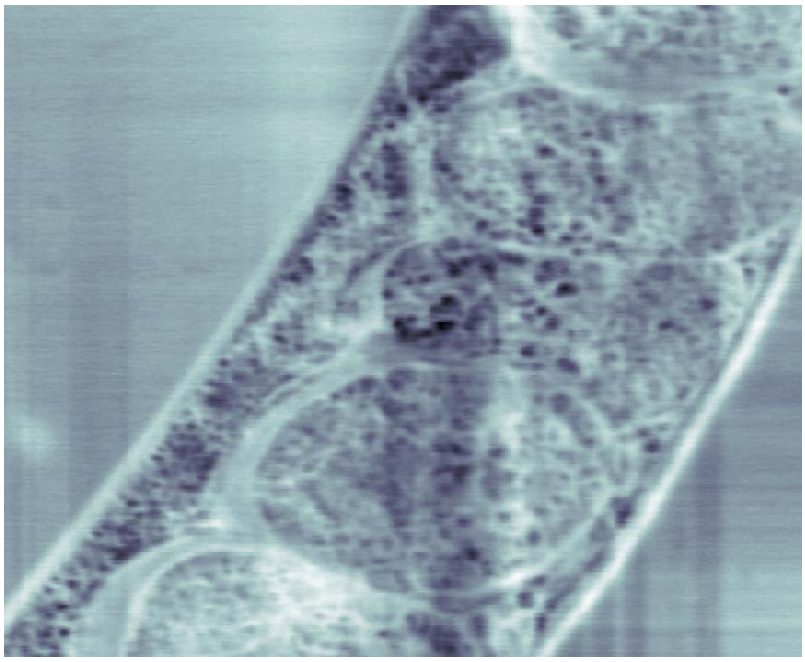

Figure 3.13: NR image of Caenorhabditis elegans.

spectrum for a single pixel in the bead in Fig.3.11(c). The spectrum shows the expected dominant ring mode at 1000cm^{-1} as observed in the Raman spectrum [6]. Fig.3.12 shows larger beads embedded in poly-methyl methacrylate (PMMA) and imaged under the same acquisition conditions.

3.11 Biological imaging

Due to its signal strength, NR signals allow faster imaging. So in our experiments, the NR signal is used to acquire morphological information(Fig.3.13) first and then FTCARS imaging is applied on areas of interest to acquire chemical information. Fig.3.14 shows two images acquired from Caenorhabditis elegans. The first image(Fig.3.14 (a)) is acquired with the NR signal. FTCARS measurement (Fig.3.14 (b)) is performed at the center of this image. 90 picoJ pulses at 75MHz are used. The average dwell time on each pixel is 40ms. From an early Raman microscopy study[76] on DNA and proteins, the dominant mode around 1000 cm^{-1} is

an indicator for the amino acid Phenylalanine. Comparable Raman studies are not available on Caenorhabditis elegans, making it difficult to confirm this assignment. FTCARS has also been applied to image live cells but without reproducible results. The challenges are that the thickness of subcellular components is much smaller than the focal depth and the molecule density is low, which significantly reduces the efficiency of coherent scattering. In addition, the NR signal generated in cells is quite weak and cannot provide enough local field to lift the signal above the background noise floor, which is the motivation for the development of interferometric FTCARS (IFTCARS), discussed in **Chapter 4**.

3.12 Combined with two-photon fluorescence imaging

Because short femtosecond pulses are used in the FTCARS measurement, the same setup can also collect two-photon fluorescence signal in the backwards (epi) direction, as shown in Fig.3.2(a). In Fig.3.15, polystyrene beads of one micron in diameter and Caenorhabditis elegans were imaged with 5mW input power at a rate of two frames per second. Both samples were labeled with dragon green fluorescent dye which has a broad fluorescent emission peaked at 520nm.

3.13 Conclusion

In this chapter, the theory, implementation, and applications of FTCARS are discussed. As a time domain CARS method, FTCARS allows easy removal of the NR background signal. With sub20 fs pulses, much of the fingerprint regime spectrum can be acquired in a single measurement. The FTCARS method can also be simply combined with self-phase modulation imaging (NR imaging) and two-photon fluorescent imaging in epi direction. The simplicity, robustness, and multimodality make FTCARS a very promising tool for biological imaging applications.

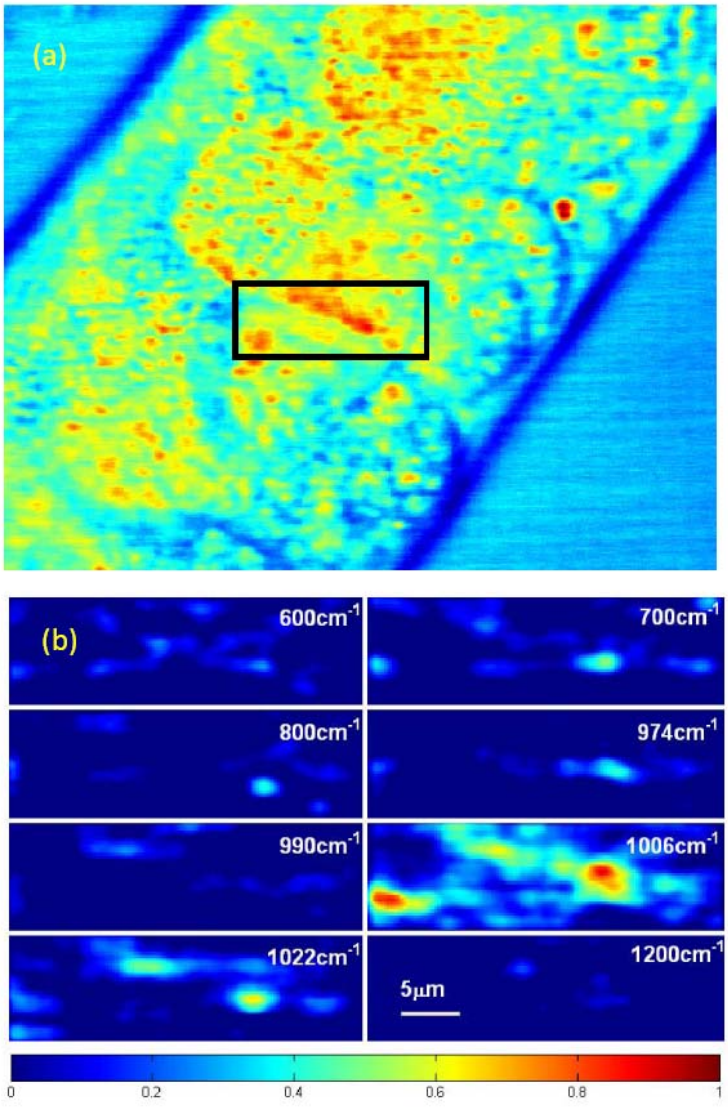

Figure 3.14: (a) NR image of Caenorhabditis elegans; (b) 40x128 pixel FTCARS image from the area inside the box in (a). 90 picoJ pulses at 75 MHz are used. The data acquisition time is 40ms/pixel.

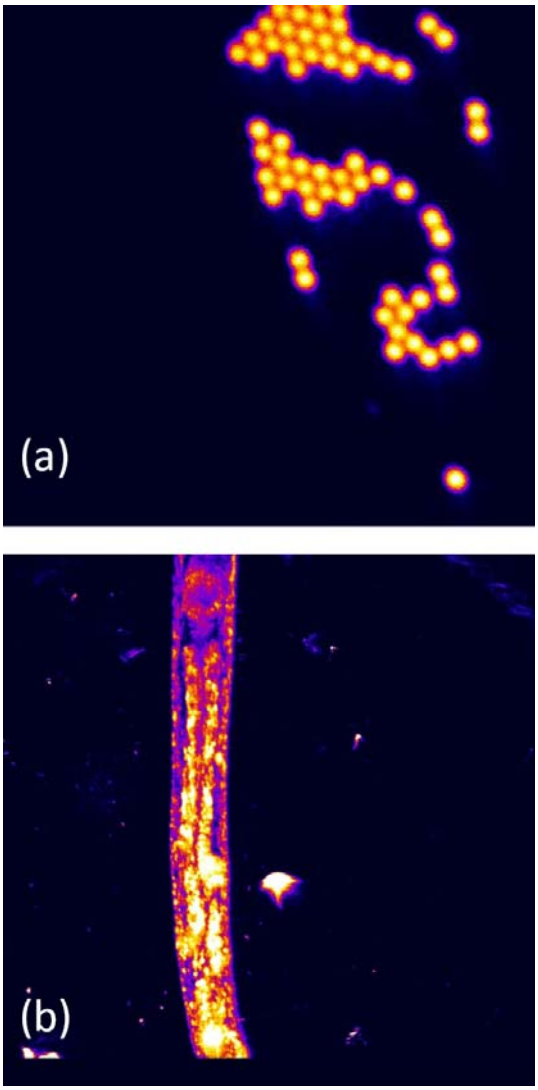

Figure 3.15: (a) Polystyrene bead of one micron in diameter. (b) Caenorhabditis elegans.

CHAPTER IV

Interferometric Fourier transform CARS microscopy

4.1 Introduction

The coherent signal generated inside the focal volume has a quadratic dependence on both the molecule concentration and the thickness of the sample (see Eq.2.38). For imaging thin and dilute samples, the NR signal generated may not provide enough local field to lift the signal above the background noise floor. In this section, a compact interferometric FTCARS method with passive phase stability is presented, which provides additional local field to interfere with the signal and yield shot noise limited signal to noise ratio (SNR), the highest achievable SNR with classical light sources.

4.2 Noise analysis

The sensitivity of FTCARS is determined by the noise level. Three types of noise contribute to the noise floor: background noise, shot noise, and laser noise. Background noise refers to the constant noise floor which is independent of input light power. Thermal noise of the detector, electronic noise from the signal amplification electronics and the read noise from the analog to digital (AD) converter are all considered background noise. Shot noise describes the random fluctuations in a signal due to the random arrival time of the signal carriers. It is a quantum noise

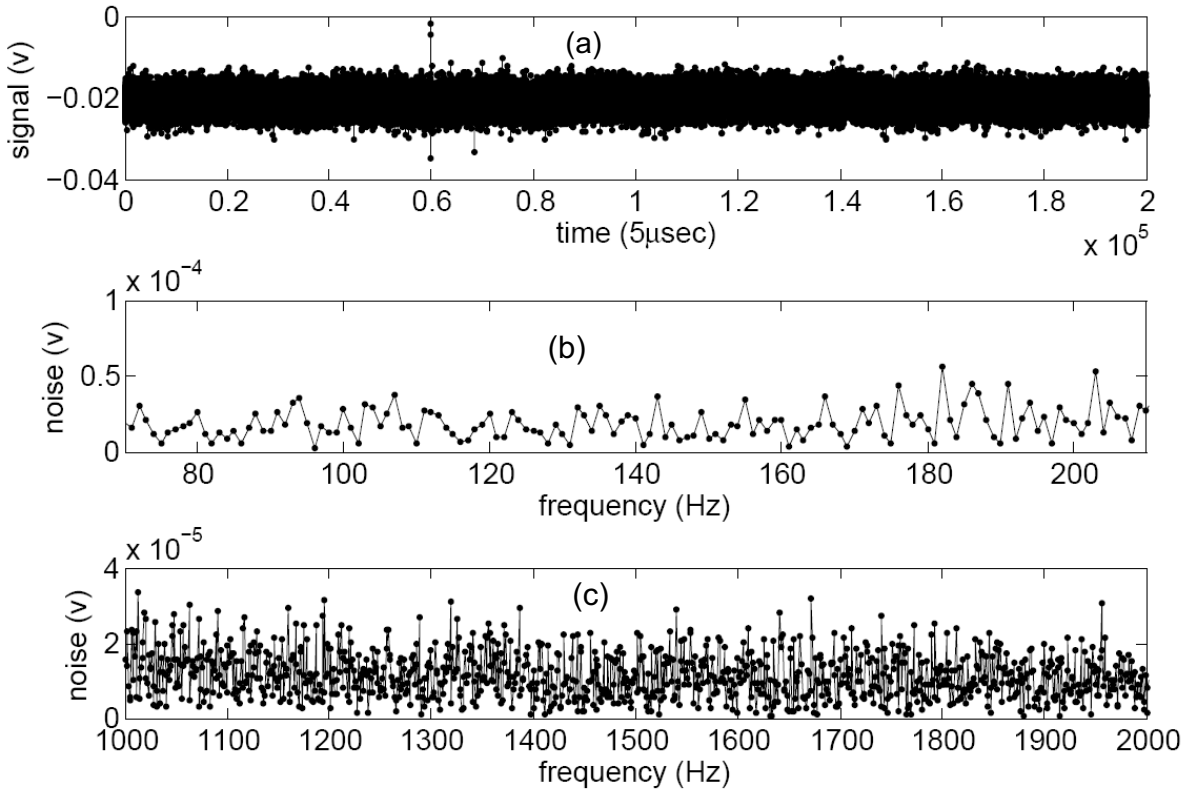

Figure 4.1: (a) Time domain noise data, data acquisition rate is 200kHz, the total data collection time is one second; (b) the noise spectrum around 140Hz; (c) the noise spectrum around 1500Hz.

effect, related to the discreteness of photons and electrons. The output of a laser or an incoherent light source, such as an incandescent lamp, can be described as a Poisson process. As a result, the photon number fluctuation measured for a certain time is proportional to the square root of the mean photon number. So the SNR decreases as the average intensity decreases. Another noise source is the laser power noise which consists of the very slow ($\sim$ 1Hz) intensity fluctuations due to pump source and laser cavity instabilities. This noise is linearly proportional to input light power. Because it is slow, one general noise suppression method is to use a light modulator combined with a lock-in amplifier to shift the signal to higher frequency where the influence of laser noise is greatly reduced. For a time domain measurement, a more straightforward method is simply to use a fast scanner.

In a FTCARS experiment, the signal is acquired at $\sim$ 100Hz. In order to determine the noise components, noise power dependence measurements were performed with a data acquisition card. As an example, Fig. 4.1(a) shows the time domain noise measurement performed with a Hamamatsu R636-10 PMT detector loaded with 200kΩ resistance and a 1200V power supply. The signal is digitized at 200kHz for a total data acquisition time of one second. The Fourier transform of the time domain data generates the noise spectrum around 140Hz and 1500Hz as shown in Fig. 4.1(b) and (c). The measurement is performed with different gains (applied voltages) and signal levels as shown in Fig. 4.2(a) and (b). For applied voltages greater than 900V, the double log plot has a slope of 1/2, which indicates the system is shot noise limited. At lower gains or higher input powers, the slope is between 1/2 and 1, indicating that laser power noise starts to become significant. Most of the imaging measurements are performed at the high gain (1150V-1250V) weak signal regime which is dominated by shot noise.

4.3 Idea for achieving shot noise limited SNR

From the signal component analysis in the previous chapter, we know that if the local field energy is b^2 and the coherent Raman signal energy is a^2, then the signal energy after Fourier transform is ab (see Eq.3.1). If the local field dominates all other signals, then the total noise (shot noise) is close to $\sqrt{b^2} = b$. The signal to noise ratio (SNR) is therefore $ab/b = a$. In this way, the SNR is independent of the amount of local field present in this measurement. This SNR is the highest possible with a classical light source. Downconversion is able to generate twin entangled photons [77]. If one of the twin photons is used for the local field and the other is used as a reference to correct the shot noise, the SNR can be further improved in theory. For

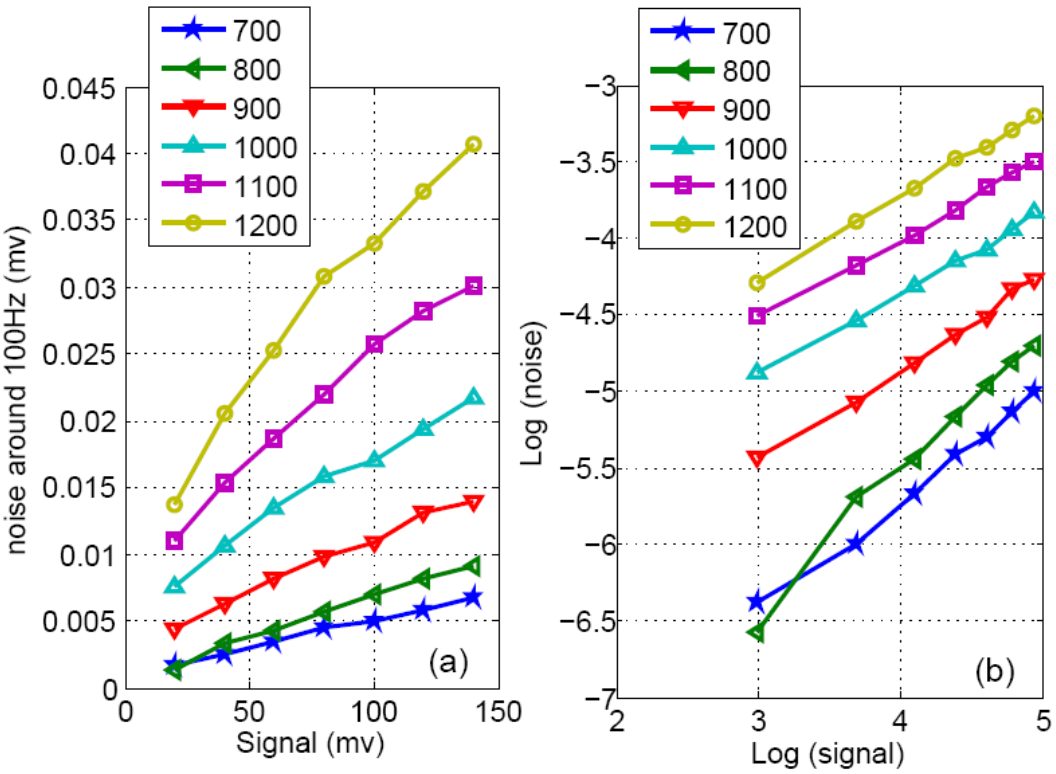

Figure 4.2: (a) Noise power dependence data at different gain (applied voltage) levels; (b) the same data on double log plot.

practical applications, a simple and compact design is desired, so only classical light source is considered in our experiments.

In FTCARS, the first pulse also generates a nonresonant signal which does not interfere with the time dependent resonant signal since it is not time coincident. The presence of this background signal lowers the SNR by $\sqrt{2}$. Additionally, electronic noise and a small amount of light that leaks through filters contribute to the noise floor. To suppress all these noise sources, a local field which is a few times greater than the nonresonant signal generated by the second pulse is required. One easy solution is to change the power ratio of the two pulses. For example, if the second pulse is twice as powerful as the first one, then the nonresonant signal generated by the second pulse is eight times as strong as the first one and the local field dominates. The shortcoming of this method is that the resonant signal is not optimized because $E_r \propto E_1^2 E_2$ and the ideal power ratio would be $2:1$.

An alternative approach is to add an external field to perform an interferometric measurement[78, 79]. This external field needs to be phase stabilized with respect to the resonant signal. A straightforward way to add the external field is to use a second Michelson interferometer. As discussed in previous chapter, there is a 0.2 rad short term phase drift in our interferometer which may cause error for the interferometric measurement. Phase stabilization electronics and piezo transducers can correct for this error, but they complicate the experiment[80]. The source of this 0.2 rad drift comes from the fact that there are 6 separated elements in the interferometer and the two beams of the interferometer go through different elements. If both the signal and external field traverse the same optical path, the phase stability should be greatly improved. An external field for FTCARS must be time-coincident, and contain frequencies appropriate to interfere with the blue-shifted resonant signal. The

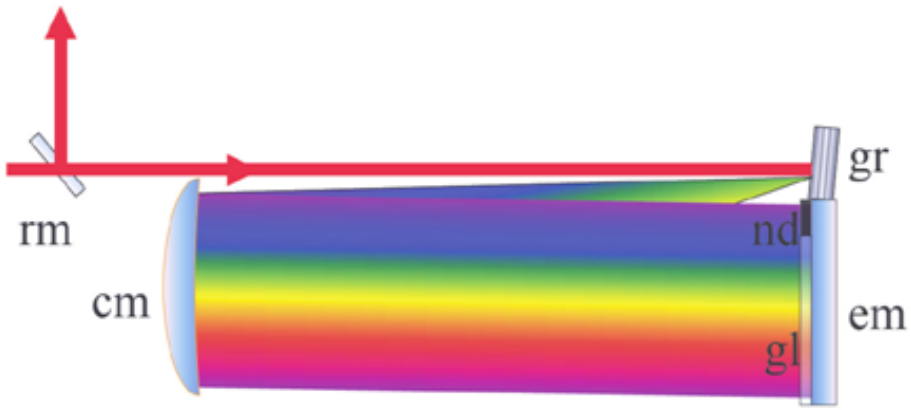

Figure 4.3: 4f setup, RM: return mirror, CM: curved mirror, gr: grating, ND: linear ND filter, EM: end mirror (Fourier plane), gl: compensation glass

broad bandwidth of our probe pulse suggests that the blue edge of the spectrum, which is normally attenuated by a long pass filter to enable effective separation of the FTCARS signal could be used for interferometric detection. We note that this arrangement has excellent passive phase stability since the external field is derived from the probe pulse itself: any phase drift will be common to both signal and external field and will not affect their relative phase.

4.4 Experimental setup

We implement interferometric FTCARS (IFTCARS) with an all reflective 4f pulse shaper setup (Fig.4.3) inserted after the interferometer in Fig.3.2. In a 4f setup, the separations between grating to curved mirror and between curved mirror to end mirror are exactly equal to the focal length of the curved mirror. With a collimated input, this setup is identical to a spectrometer. The grating disperses the input light to different directions according to its wavelength and the beam of each color is still collimated. The curved mirror makes each color propagate in parallel and focus to a spot whose size is determined by the input beam size and the focal length of the curved mirror (in other words, the numerical aperture).

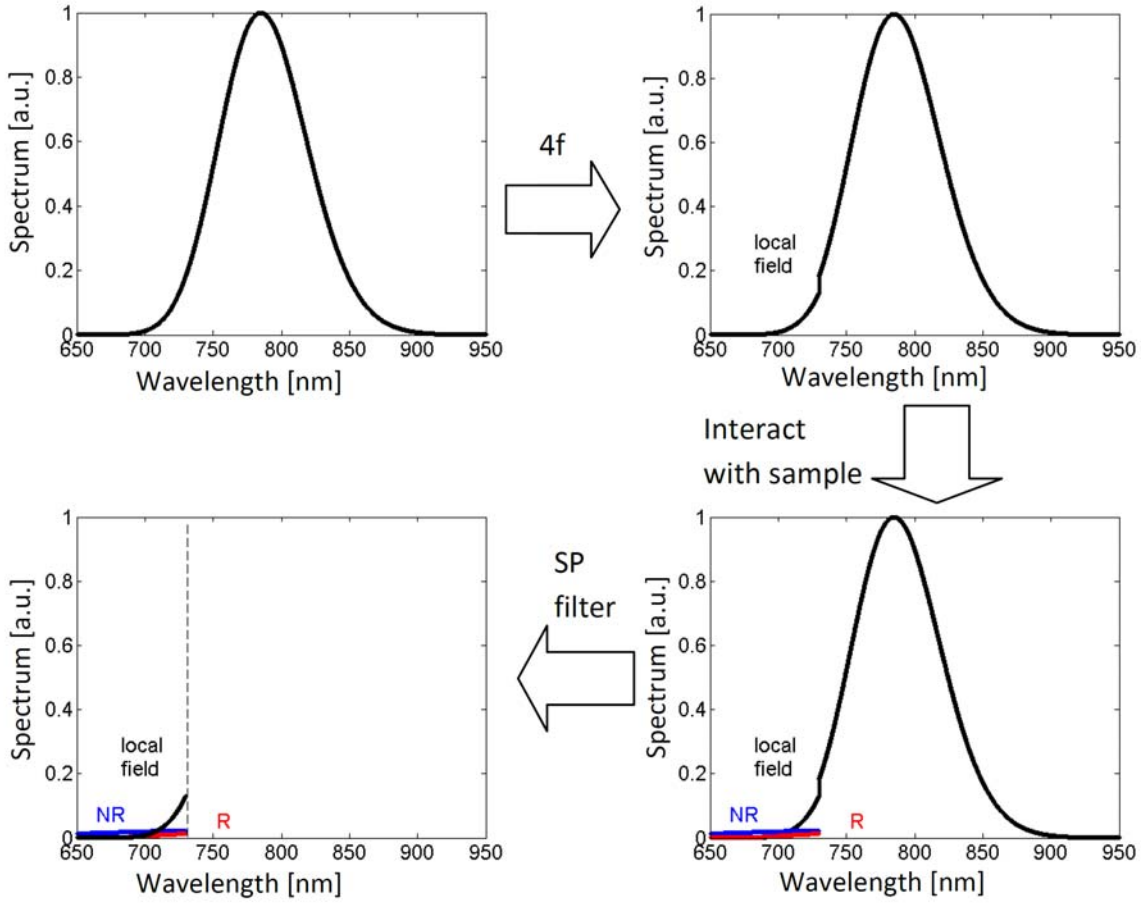

Figure 4.4: Probe pulse spectrum variation: The blue edge of the probe pulse is reduced by the 4f setup to provide a controllable local field. Blue shifted NR and CARS(R) signals are generated in the sample. A short pass filter only passes the blue shifted signal and the controllable local field.

In order to minimize dispersion, we use all reflective elements except for the glass and the ND filter. The end mirror is tilted down and the return beam is lower than the input beam to allow separation of input and output. The position of the curved mirror is fixed on the optical table, and the grating and end mirrors are mounted on two translational stages. The dispersion of the beam is measured before and after the 4f setup to ensure it is at the zero dispersion point. The spectrum at different positions on the output beam cross section is measured 10 meter away from the four f pulse shaper to verify that the spatial chirp has been minimized. When properly aligned, the final 4f setup is free from both spatial chirp and temporal chirp. Setting up the folded 4f is simpler than a true 4f with two gratings and two curved mirrors, which has four degrees of position freedom.

Unlike FTCARS, in IFTCARS the blue edge of the probe pulse is not completely blocked, allowing it to act as a local field. A neutral density (ND) filter is placed in front of the end mirror to control the local field intensity. A glass plate of the same material and thickness is placed next to the ND filter to compensate for the group delay. The setup works as an adjustable long-pass filter, where the leakage through the ND filter becomes the new local field. One important parameter for optimizing the IFTCARS signal is the interference contrast between the resonant CARS signal and the local field, which depends on the relative spectral profiles of the signal and the local field. To investigate the effect of using the blue edge of the laser pulse (as in IFTCARS) and the NR signal (as in FTCARS), we calculate the interference contrast for theses two cases relative to using an ideal local field with spectral characteristics that matched the signal. The calculation shows that the interference contrast is within 5% of the optimum value for an 800cm^{-1} mode and within 25% for a 1400 cm^{-1}. Despite the fact that the NR signal has a long tail extending past 685nm, the

difference between employing the NR signal and the blue edge of the laser pulse as the local field is negligible, in agreement with our experimental observations. The benefit of IFTCARS comes from the ability to adjust the magnitude of the local field, rather than its spectral characteristics.

4.5 Phase stability

The advantage of this setup over many other interferometric methods [81, 82] is the passive phase stability. In order to quantitatively characterize the stability, spectral interferometry [73, 83] between the nonresonant signal and the local field was recorded with a spectrometer equipped with a thermo-electrically cooled CCD. To generate clear fringes in spectral domain, two No.2 cover slips were inserted between the ND filter and the end mirror to generate a time delay of 1.7 ps. The strength of the added local field was varied until the highest fringe visibility is achieved. To monitor the phase stability, 10,000 spectra were recorded over 100 seconds with an actual exposure time of 6.7 msec/spectrum. The 10,000 spectra are plotted together and shown in Fig. 4.5. The time domain measurement usually takes one second. Thus the measurement over 100 seconds is more than enough to characterize the stability. Fourier transform yields the time delay and phase. The standard deviation of the phase difference between the measurements is 0.0143 which is equivalent to a phase stability of $\lambda/435$, indicating that the passive phase stability is extremely good.

4.6 Experimental results

We use a $4\mu m$ polystyrene bead to demonstrate the SNR improvement with IFTCARS. The nonresonant signal is used to locate the position of the bead. 13 pJ pulses are used for both nonresonant imaging and CARS imaging. The entire non-

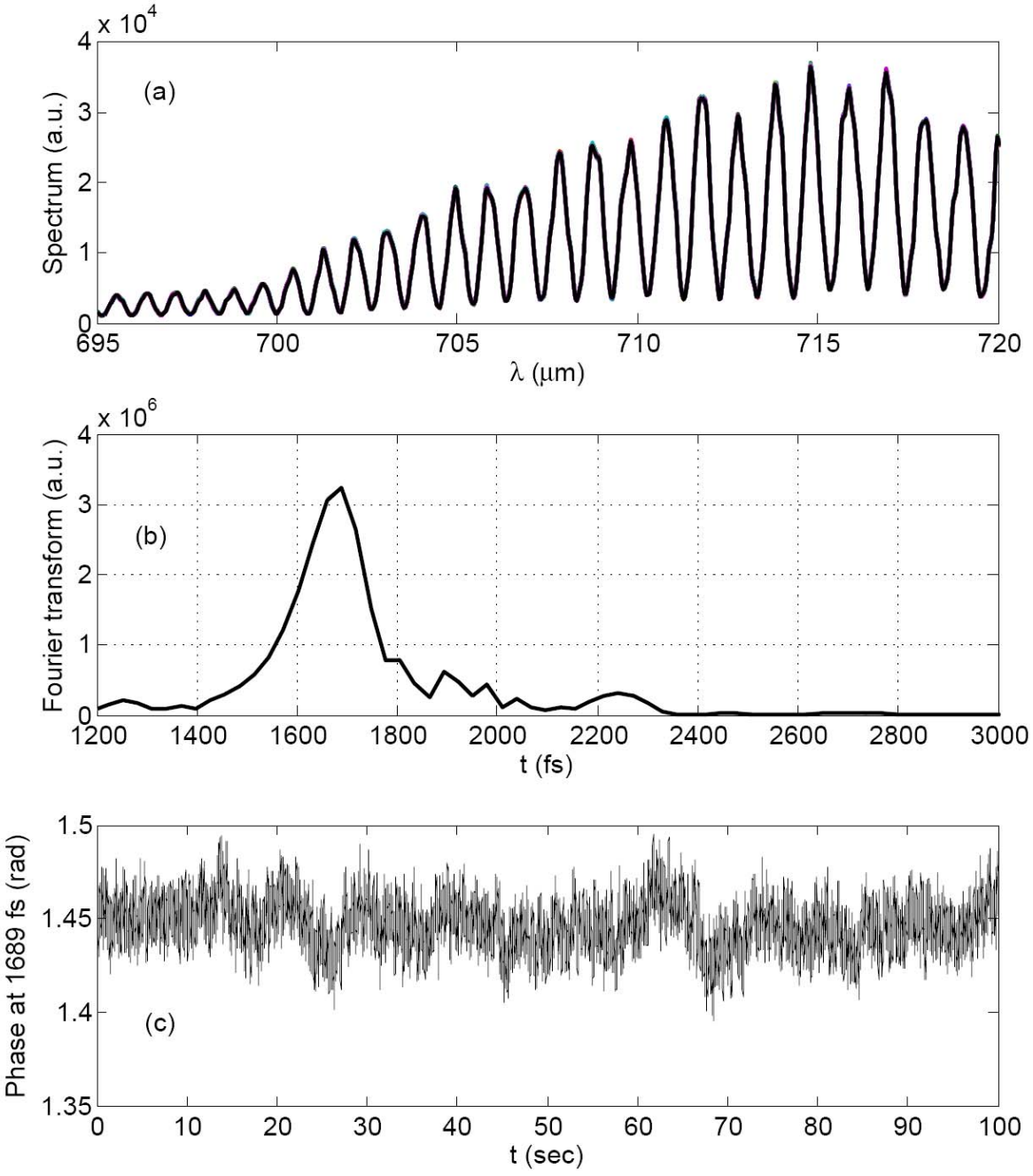

Figure 4.5: Phase stability of IFTCARS setup, determined by spectral interferometry. (a) 10,000 spectra are plotted. The fringes are generated by introducing a time delay on the local field. (b) The absolute value of the Fourier transform of the spectra in (a). (c) The phase at 1689 fs time delay, whose standard deviation 0.0143rad is equivalent to $\lambda/435$ at $\sim 710nm$

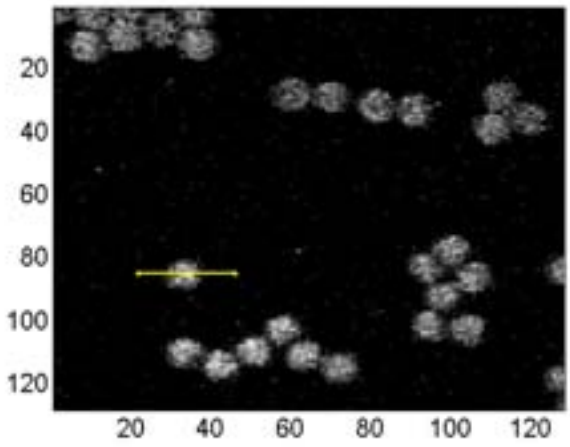

Figure 4.6: Nonresonant signal image of 4 μm polystyrene beads. The yellow line indicates the linescan position.

resonant image is acquired in 0.5 second. The yellow line in Fig. 4.6 indicates the position of the linescan. The time delay range is 2100fs, yielding $16cm^{-1}$ spectral resolution. The linescans acquired with IFTCARS and FTCARS are shown in Fig. 4.7 (a) and (b). Under the same experimental conditions, IFTCARS produces a bright resonant image at the expected spectral peak position for polystyrene within the spectral resolution of the measurement and shows a considerably better SNR than the FTCARS measurement. Fig. 4.7(c) compares the power spectrum for a single pixel in the image, demonstrating the considerable improvement made with the addition of the local field.

To clearly show the effect of the added local field, the total noise is plotted as a function of added local field power on a double log plot (Fig. 4.8). Two regimes are clearly seen on the plot: a background noise regime (local field $<$ 1pW) and the shot noise regime (1 nW $>$ local field $>$ 100pW). The actual local field used in the IFTCARS images shown in Fig.4.7 is 38 picoW as indicated with an arrow. From the previous discussion, we know that the SNR starts to saturate once the noise enters the shot-noise regime. In theory, an arbitrarily high local field can be

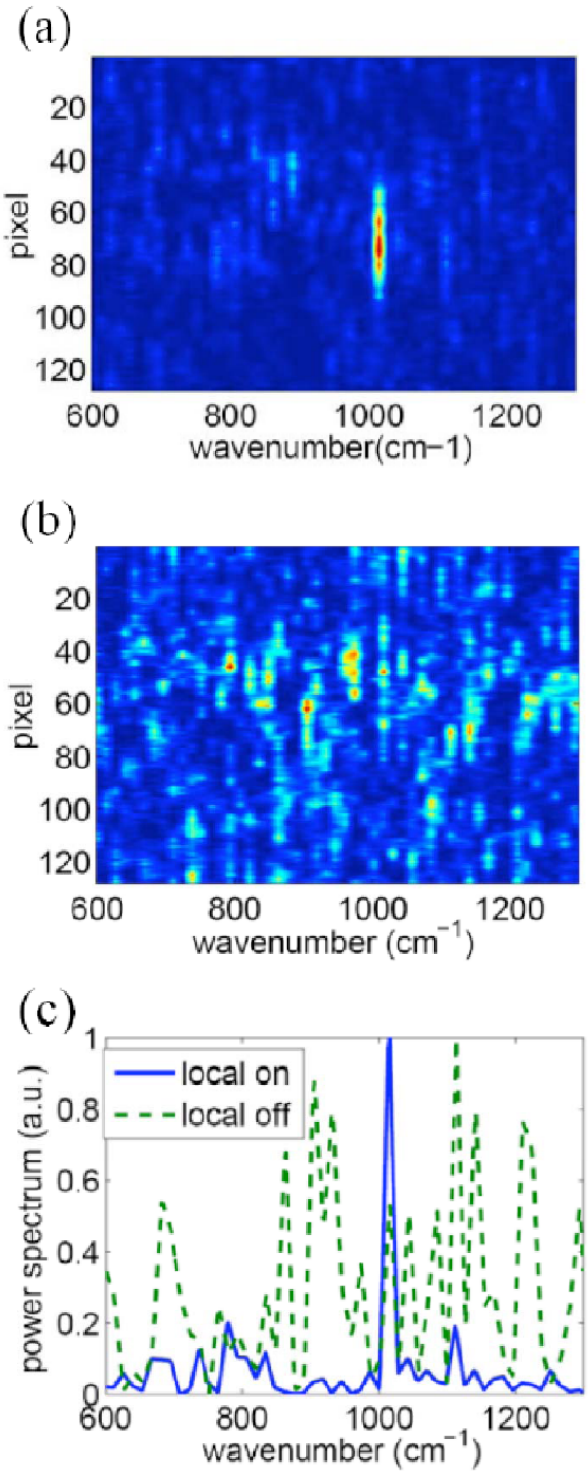

Figure 4.7: (a) Line scan through a $4\mu m$ polystyrene bead taken with IFTCARS. The image is acquired with 1 mW power (13pJ pulse) in each beam with a data acquisition time of 4 seconds and spectral resolution of $16cm^{-1}$. b) Corresponding standard FTCARS line scan (local field is blocked). c) Comparison of CARS spectra at pixel 75 in the two images.

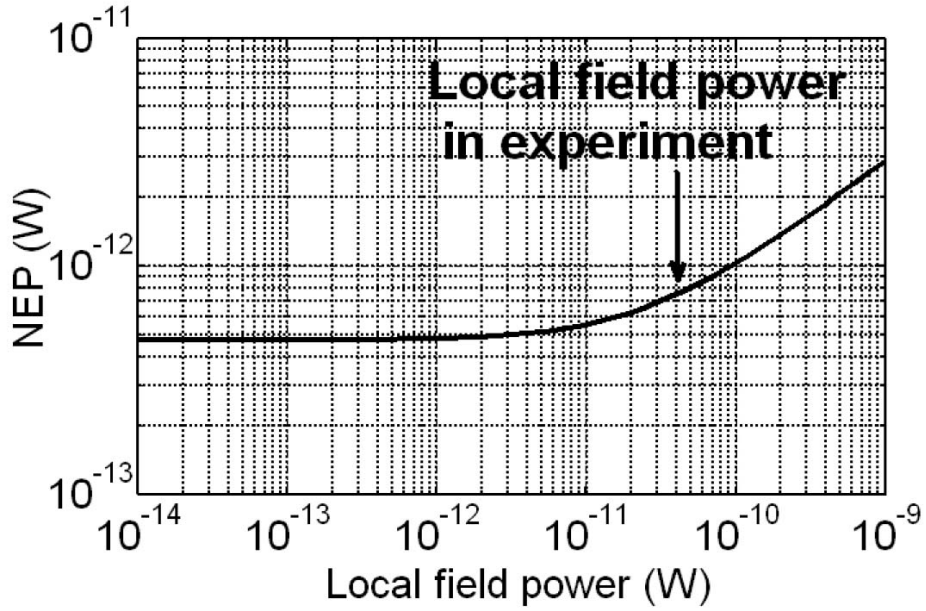

Figure 4.8: Total noise equivalent power (NEP) vs.local field power. Two regimes are clearly seen: a background noise regime (local field $<$ 1pW) and the shot noise regime (local field $>$ 100pW). The actual local field used in the IFTCARS images shown in Fig. 4.7 is 38pW as indicated with an arrow.

added without affecting SNR because the signal amplitude and the shot noise have the same dependence on the local field. In experiments, however, there are two other concerns. One is that the laser power noise becomes significant if the power is above 1nW. The other concern is that the signal is digitized with a data acquisition card with 12 bit dynamic range. The signal contrast is $ab/b^2 = a/b$, which decreases at higher local field power. So in our experiment, the magnitude of the local field was chosen to operate as close to the shot-noise limit as possible while taking into account the finite dynamic range of the 12 bit data acquisition electronics. Further increasing the local field without the need to consider the dynamic range of the data acquisition is expected to give at most a 25% improvement in SNR.

4.7 Comparing IFTCARS with pump-probe impulsive Raman scattering

One extreme situation of IFTCARS is where the local field added is greater than 1 nW, providing a total signal that is strong enough to be detected by Si diode detectors, whose quantum efficiency is higher than that of a PMT in the near infrared region. This is similar to the conventional pump-probe technique, in which no filters are placed before the sample and the entire blue edge of the probe pulse enters the detector. At this signal level, laser noise becomes significant and a balanced detector is required to cancel the laser amplitude fluctuations. If power fluctuations are completely canceled, this method can also reach the shot-noise limited SNR and then the power ratio between pump and probe pulses should be 2:1 for maximized resonant signal generation.

4.8 Dual channel detection

In pump-probe impulsive Raman scattering experiments, both the red and blue edge of the probe pulse can be measured. As the probe pulse may gain or lose energy to the molecular oscillation, the probe pulse is either blue or red shifted. Therefore, the oscillations measured on the red and blue edges of the probe pulse are out of phase by π[39].

In IFTCARS, the phase of the time domain oscillation can be tuned by rotating the compensation glass plate in the 4f setup. The relative phase between the anti-Stokes and Stokes signals can be set to π. By separating the anti-Stokes signal from the Stokes signal with a spectral filter, both signals can be simultaneous recorded with two PMT detectors. This can be useful to remove noise common to both channels. For example, at the early stage of this experiment, certain electronic noise affected both of the PMT detectors. If one data set is subtracted from the other,

this common noise can be greatly reduced (Fig. 4.9). Since that time, improved shielding of the experiment has reduced the common background noise, making this balanced detection unnecessary.

4.9 Conclusion

In this chapter, the SNR of FTCARS is analyzed and the result suggests that an adjustable local field can help achieve shot-noise-limited SNR. We implement IFTCARS in a setup of passive phase stability to provide additional local field. Experimental measurement indicates a phase stability better than $\lambda/400$. IFTCARS is directly compared with FTCARS with low excitation power and shows an improved SNR, which makes IFTCARS valuable when the generated NR signal is not strong enough to suppress the background noise.

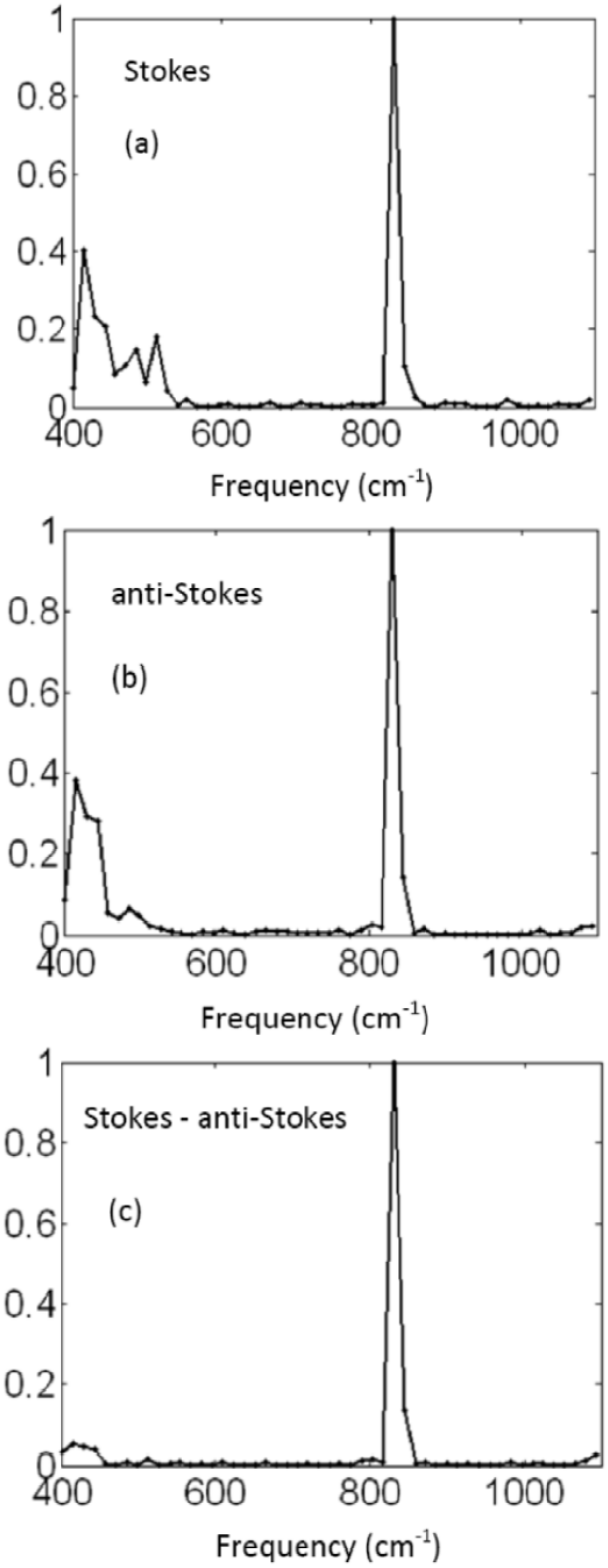

Figure 4.9: (a) Stokes spectrum. (b) anti-Stokes spectrum. (c) Fourier transform of difference signal.

CHAPTER V

Spectral-domain coherent Raman imaging

5.1 Introduction

In the field of optical coherence tomography (OCT)[48, 49] and sum frequency generation spectroscopy[50], there have been discussions about the significant SNR advantage of spectral domain methods over time domain methods. In this chapter we consider the time domain interferometry method of IFTCARS, and compare its achievable SNR with that of its spectral-domain counterpart. We conclude that the methods achieve roughly equivalent SNRs under shot-noise-limited conditions when the same detector is used. We verify this claim experimentally.

5.2 Benefits of spectral domain measurements

There are three practical advantages of using spectral domain measurements. First, laser power fluctuations do not distort the spectral line shape in spectral domain methods, while in the time domain they can modulate the shape of the retrieved spectrum. For IFTCARS, the signal is linearly proportional to both the pump power and the probe power. From Fourier transform theory, we know that multiplication in one domain is equivalent to convolution in the other domain. Thus, if the laser power has a sinusoidal fluctuation such that in the time domain it modulates the signal, then in the spectral domain, there will be side bands generated. Laser fluctu-

ations can be corrected for if the input laser power(P) is measured. We note that the laser fluctuations at the sample may have two origins: power instability and pointing instability. In our microscope setup, the latter is the larger effect and causes line to line variations in the image. A more demanding task is to take time domain measurements on samples that vary quickly over the measurement time, which causes significant signal intensity variation. In this situation, it is of great advantage to perform spectral domain measurements.

For time domain measurements, the pulse needs to be as short as possible to resolve the high frequency modes. One disadvantage of using a very short pulse is that it has higher chance to damage the sample compared to using longer pulses of similar power[70, 71]. In the spectral domain method, there is flexibility in choosing the input bandwidth. For example, in single mode CARS measurements, pulses as long as a few picoseonds are employed. Thus the peak power is much lower than that of the femtosecond pulses used in the time domain method.

The third advantage is that with the same femtosecond laser, the spectral domain method allows efficient measurement of the higher frequency Raman modes. For example, our laser pulse spectrum spans from 735nm to 850nm. Taking only the blue and red edge of the laser pulse allows excitation and detection of a 1841 cm^{-1} mode in the spectral domain method. The pulse duration in the time domain is 15-16 fs which cannot resolve modes as high frequency as 1841 cm^{-1}.

5.3 Theory of time delayed spectral domain coherent Raman measurement

The idea behind the time delayed spectral domain method is similar to FTCARS: it is the fact that the nuclear contribution is long lived compared to the electronic contribution (NR) and time delayed measurement can effectively suppress the NR

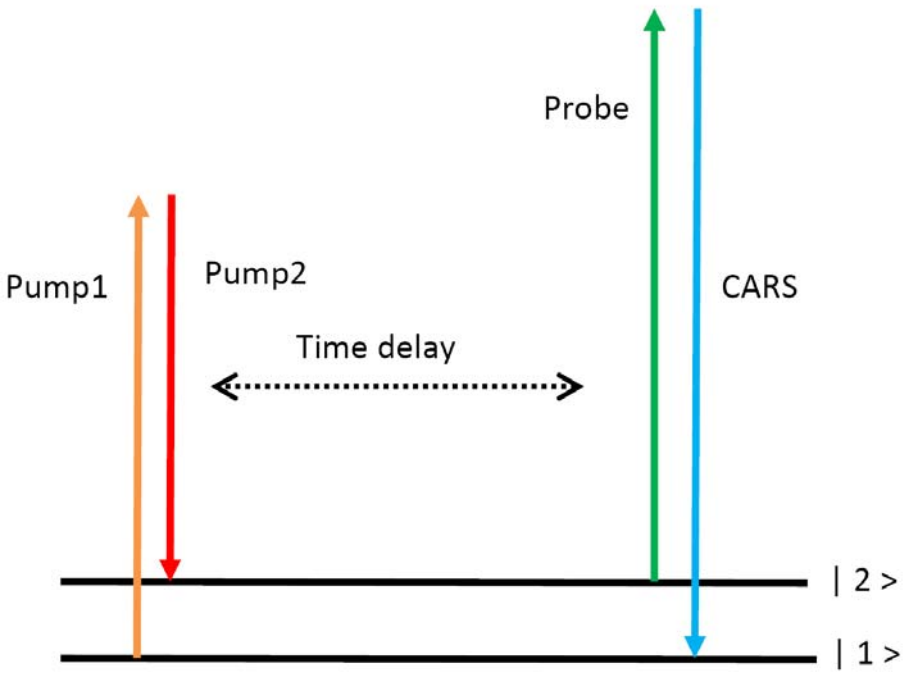

Figure 5.1: Energy diagram of the time delayed spectral domain CARS

signal. This idea has been applied in CARS spectroscopy[21] and more recently in CARS microscopy[42]. Short femtosecond pulses of two colors are used to prepare the Raman coherence (Fig.5.1). At a certain time delay, a long pulse of different color probes the coherence and generates blue and red shifted light. The reason to use three colors is to make sure that the Raman signal is isolated in the spectral domain from the NR signal. Provided that the dark noise of the cooled CCD detector is very low, this method is also shot-noise limited. The resolution of this method is determined by the line-width of the long probe pulse. If the probe pulse is much longer than the time delay, it overlaps with the first two pump pulses in time and generates NR background. The time delay can be increased to reduce the overlapping, at the cost of reducing the signal level due to Raman decay. This is in great contrast to FTCARS, in which the spectral resolution is unlimited and the NR background can be completely removed without sacrificing resolution and signal strength.

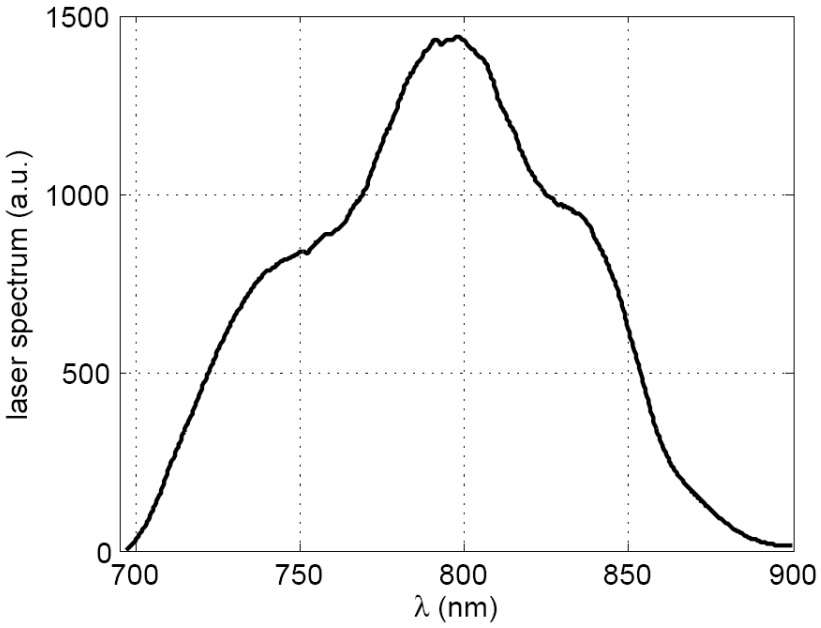

Figure 5.2: Laser spectrum

5.4 Implementation with a single pulse

We implemented the time delayed spectral domain CARS (TDSCARS) with our 12fs Ti:sapphire oscillator. The laser spectrum is shown in Fig.5.2. The laser beam is sent into a 4f pulse shaper where a mask placed at the Fourier plane selects two pump pulses and one probe pulse, as shown in Fig.5.3. As an example, we show the final spectra for exciting an 800 cm^{-1} mode (Fig.5.4 (a)) and 1400 cm^{-1} mode (Fig.5.4 (b)). The time delay between the pump and the probe pulses is applied with thin coverslips. The group delay of the coverslip is measured with spectral interferometry. First the Michelson interferometer is set to the $t = 0$ position. Then the thin coverslip is inserted into one arm. The spectral domain interference pattern(Fig.5.5 (a)) is recorded and Fourier transformed to the time domain(Fig.5.5 (b)), indicating a time delay of 250fs. Note that the reduced interference contrast is not due to unbalanced power but to the low resolution of the compact spectrometer. In the folded reflective 4f setup, the beam double passes the coverslip which makes the overall group delay of

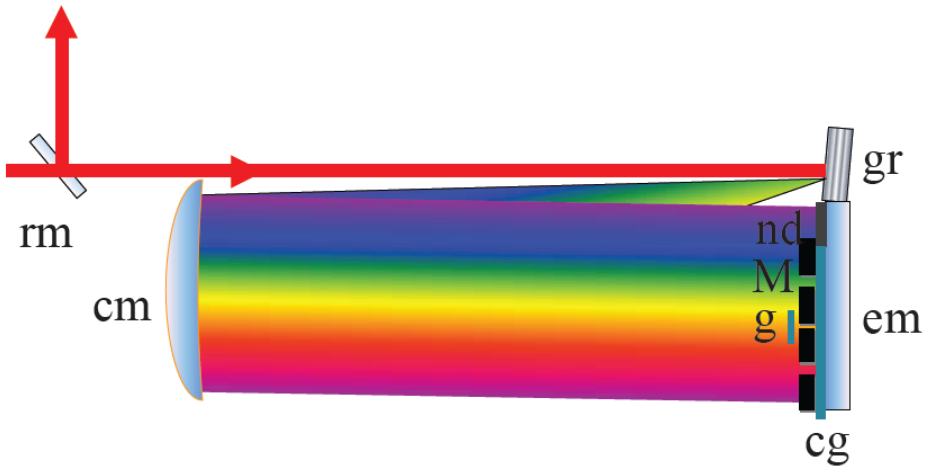

Figure 5.3: 4f setup. rm, return mirror; cm, concave mirror; gr, grating; em, end mirror; cg, compensation glass; nd, neutral density filter; g, coverslip; M, mask.

the probe pulse equal to 500fs. The group delay measurement is centered at 790nm which may differ from the actual probe pulse wavelength. Because the coverslip is thinner than 200μm, the group delay dispersion is negligible.

Fig.5.6 shows the effect of the time delay on the signal spectrum for a sample of 2-propanol. Without the time delay, the probe pulse temporally overlaps with the two pump pulses and generates strong NR signal around 800cm^{-1}. With a 500fs time delay, the overlapping is reduced significantly and the resonant signal becomes dominant, which agrees with the spontaneous Raman spectrum within the bandwidth of the probe pulse. The presence of a small amount of NR signal interferes with the resonant signal, and the fringe period matches the time delay of the probe pulse, indicating that most of the NR signal is generated around t_0. The background at 600 cm^{-1} in Fig.5.6 (b) is the NR signal generated by the two pump pulses.

5.5 Interferometric time-delayed spectral domain CARS

For imaging applications, the exposure time per pixel is often very short since rapid image acquisition is desirable. If only a few photons are acquired, the CCD

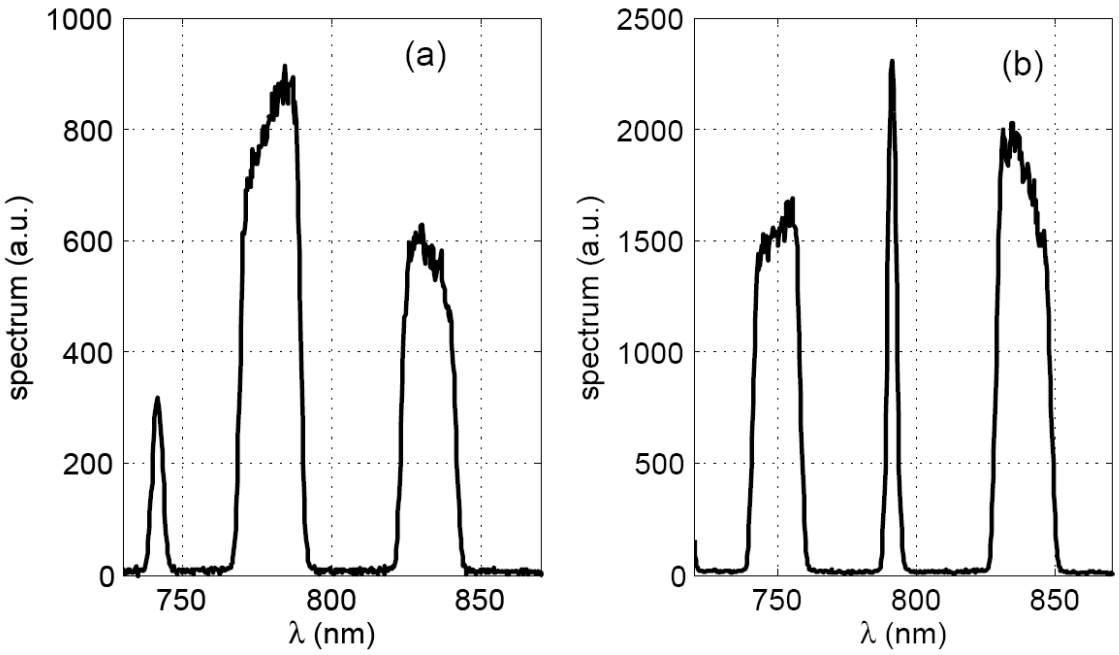

Figure 5.4: (a) Spectrum for exciting 800 cm^{-1} mode; (b) spectrum for exciting 1400 cm^{-1} mode;

read noise can often overwhelm the shot noise. Under this condition, it is useful to apply interferometric techniques to suppress CCD read noise; the SNR can be greater than one even if there are only two photons acquired ($\sqrt{2} > 1$).

An approach similar to IFTCARS can be employed to add a local field to amplify the weak resonant signal and reach the shot-noise-limited regime. Two No.2 coverslips are carefully placed to add $\sim 1700fs$ time delay to the probe pulse. The final input spectrum is shown in Fig.5.7. Note that the local field from 700 to 720 nm is 9 orders of magnitude weaker than the input pulses.

Using 2-propanol as a reference sample, the amount of resonant signal present can be determined by blocking the local field. The spectrum acquired with one second exposure time is shown in Fig.5.8, where the fringes are due to the interference between resonant CARS signal generated at t=1700fs with the NR signal generated around t=0fs. Based on this measurement, the total signal collected over one second is about 1.9×10^4 photons. So if the exposure time is reduced to 4msec and the noise is

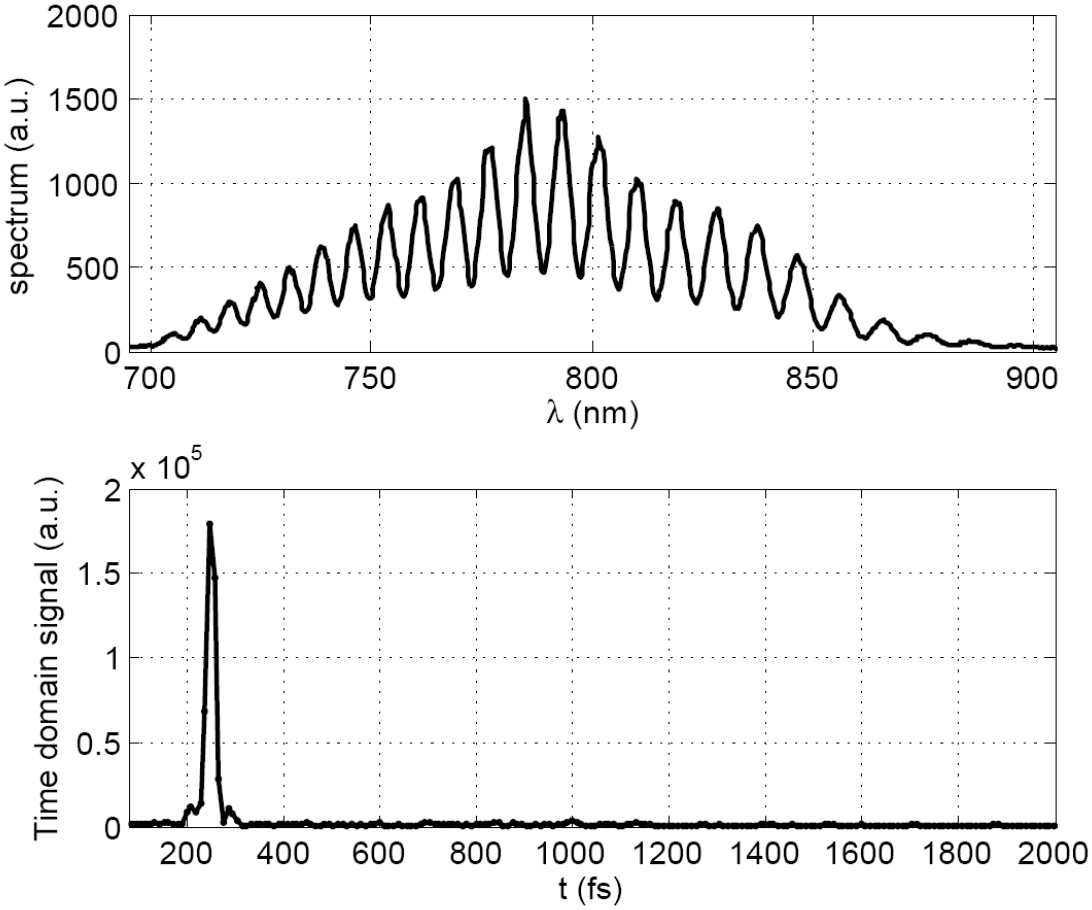

Figure 5.5: (a) Interference pattern in the spectral domain. The reduced signal contrast is due to the limited resolution of the compact spectrometer (b) Fourier transform of the interference pattern, indicating a time delay of 250fs.

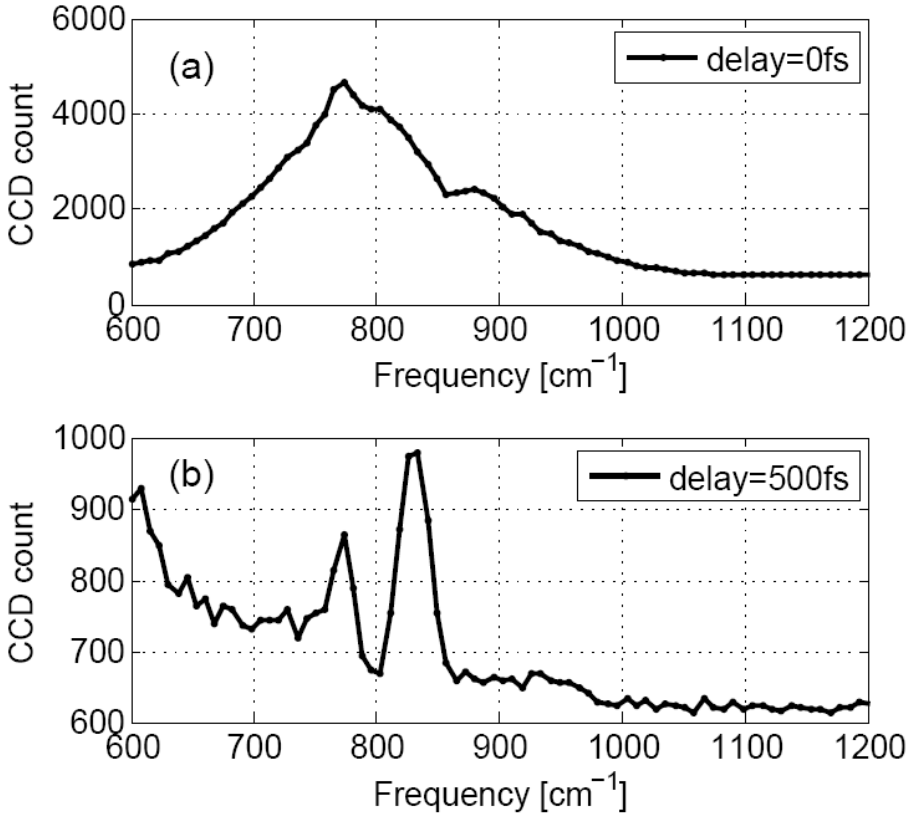

Figure 5.6: 2propanol signal spectrum without (above) and with (below) time delay. The excitation power is 2.35mW. The data acquisition time is 200msec. In (b) the peak position around 820cm^{-1} agrees with the spontaneous Raman spectrum of 2-propanol within the bandwidth of the probe pulse. The background at 600 cm^{-1} is the NR signal generated by the two pulse pulses.

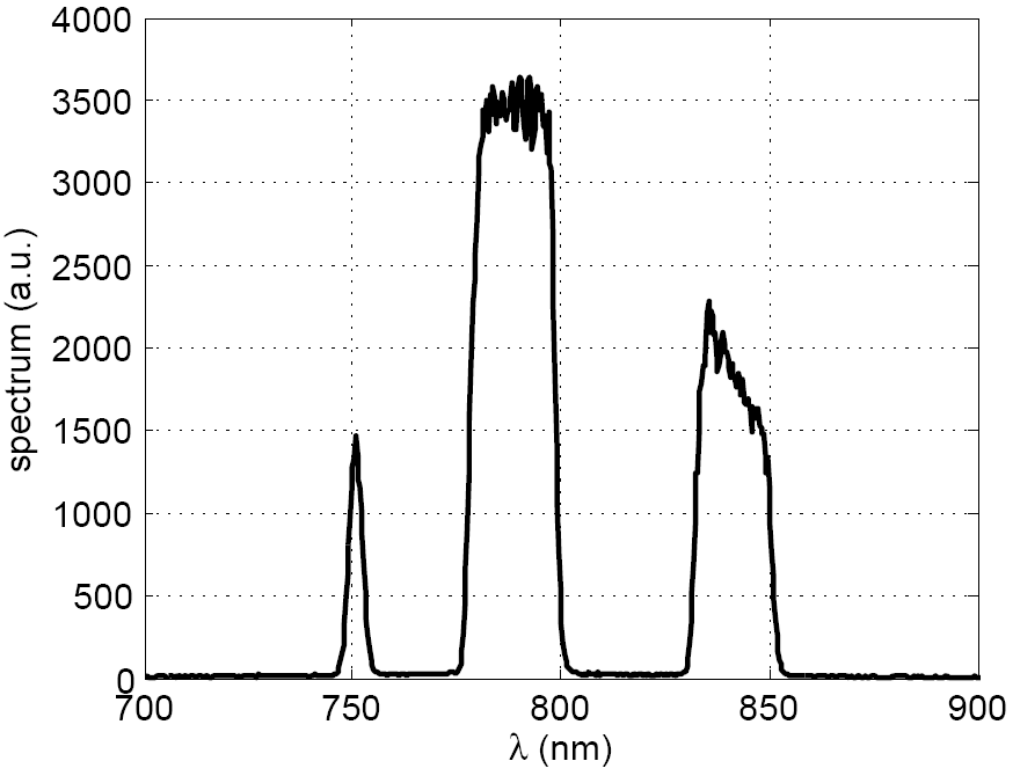

Figure 5.7: Input spectrum. The local field from 700 to 720nm is too weak to show up on the same scale.

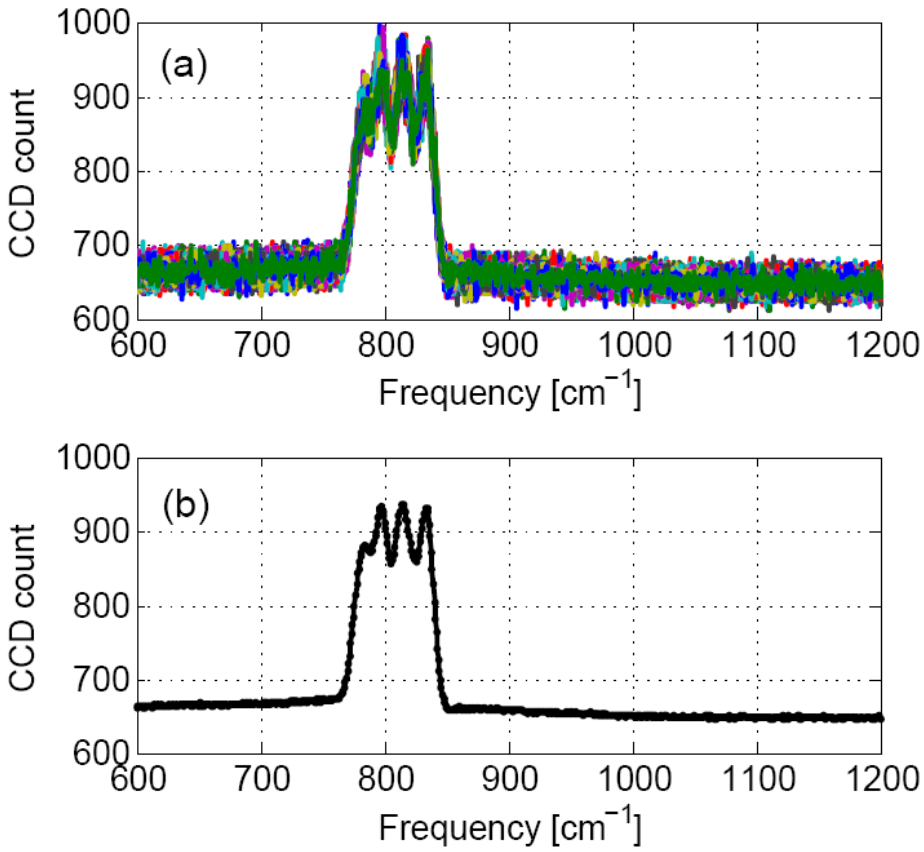

Figure 5.8: (a) 100 TDSCARS spectra from 2-propanol, input power = 4.8mW, exposure time = 1 sec; (b) averaged spectrum from (a).

dominated by shot noise only, the SNR is estimated to be $\sqrt{1.9 \times 10^4 \times 0.004} = 8.7$.

As in IFTCARS, here we use the blue edge of the laser spectrum as the local field. Fig.5.9 shows the measured local field spectrum, with fringes coming from the etalon effect of the ND filter placed in front of the Fourier plane. This local field is located around t=0 fs and overlaps with the NR signal in the time domain. The interference between this local field with the resonant signal generates fringes in the spectral domain. To retrieve the CARS spectrum, the data processing takes three steps. In step one, the spectrum of the local field is subtracted from the signal spectrum to get a clean interference pattern. Note that the shape of the local field can be measured with a very high SNR such that it does not add noise

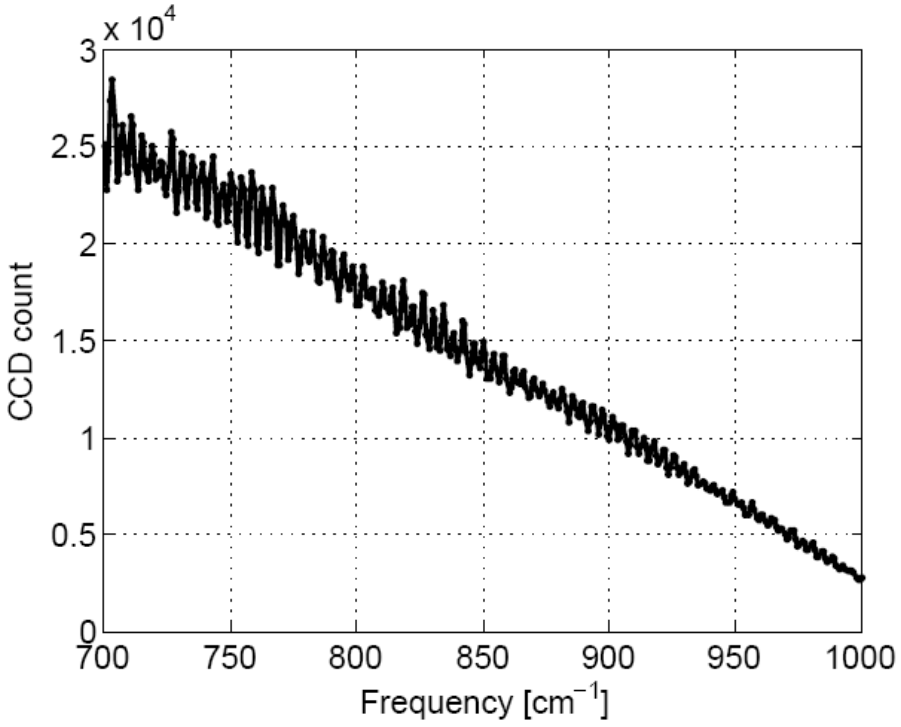

Figure 5.9: Local field spectrum.

into the data processing. In step two, the spectrum is Fourier transformed into the time domain and a bandpass filter is used to select the signal, which occurs around 1700fs. This step removes the NR signal(t=0) since it overlaps with the local field(t=0). In step three, the bandpass filtered signal is inverse Fourier transformed to retrieve the spectrum(Fig.5.10). Statistics over 4000 such measurements indicates $SNR = 8.37 \pm 0.24$ which is close to the expected value of 8.7, indicating that we are operating within the shot-noise-limited regime.

With the local field, the SNR is only determined by how many signal photons are collected. Without the local field, the CCD read noise reduces the SNR. Fig.5.11 (a) shows 10 signal spectra with the local field blocked, under the same experimental conditions as Fig.5.10. For comparison, the entrance of the CCD is closed and 10 measured dark noise spectra are shown in Fig.5.11 (b). Without the local field amplification, the signal is overwhelmed by the noise from the detector.

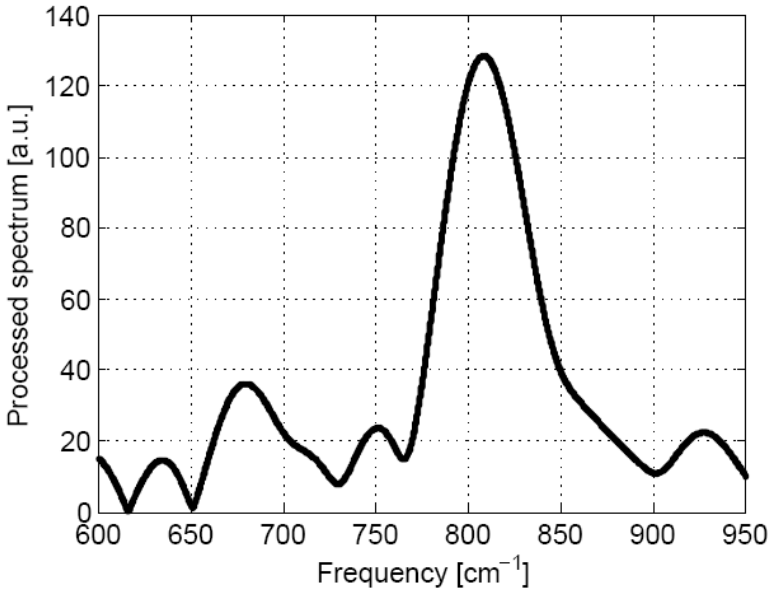

Figure 5.10: Processed ITDSCARS spectrum of 2-propanol, input power 4.8mW, exposure time 4msec.

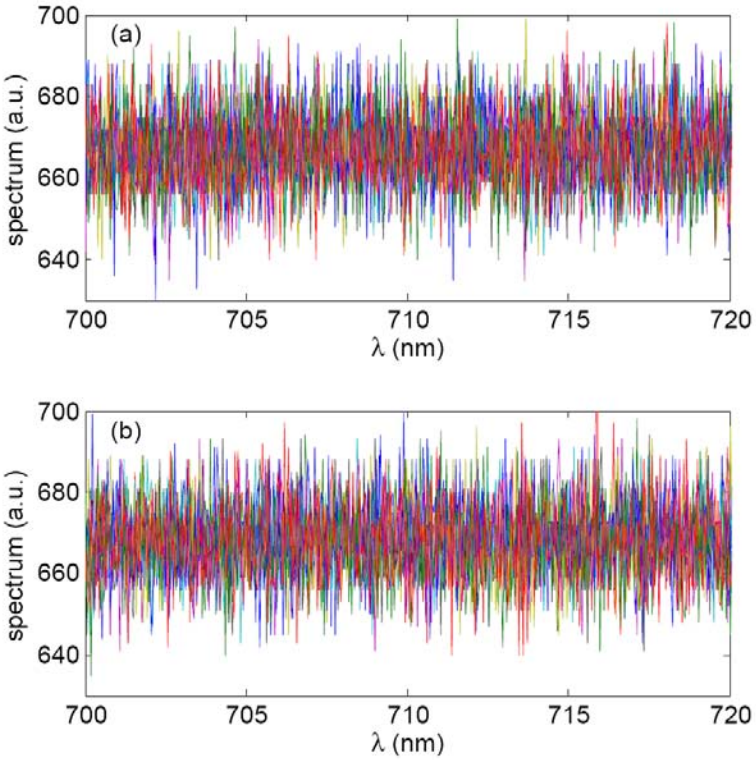

Figure 5.11: (a) Signal spectrum with the local field blocked; (b) CCD noise.

Besides the advantage of the shot noise limited SNR, ITDSCARS allows further reduction of the nonresonant signal background. The idea of the time delayed spectral domain method is to reduce the temporal overlap of the pump pulses with the probe. As a function of the time delay, the resonant CARS signal decays exponentially. For a certain delay range, the nonresonant signal decays faster than the resonant signal. Beyond a certain point, the ratio of the nonresonant to the resonant signal does not decrease any more. The nonresonant signal is mainly coming from the overlapping of the pump pulses around $t = 0$ with the long tail of the probe pulse. Phase shaping of the probe pulse can further decrease the overlapping, but in general this overlapping generates nonresonant background. To illustrate this problem, the temporal distribution of the pump and probe, and the generated blue shifted nonresonant signal is plotted in Fig.5.12. From this plot, we can see that the nonresonant signal is mainly located around $t = 0$. In ITDSCARS, a bandpass filter is applied to select the signal around t=1700fs after the Fourier transform. This time gated measurement can effectively remove the nonresonant signal around t_0.

In summary, ITDSCARS has been demonstrated with passive phase stability. The strong local field can effectively suppress the dark noise of the CCD detector, and the SNR is only limited by the shot noise only. In other words, it is only necessary to collect 100 photons of the resonant signal to achieve a SNR of 10 ($\sqrt{100}$). This means that the SNR does not rely on the low noise of the detector, and less expensive detectors with much higher dark noise and read noise can be used to achieve the same SNR. Another advantage over FTCARS is that ITDSCARS allows time gated measurement which is also the principle behind spectral domain OCT[48]. This time gated measurement can effectively remove the nonresonant signal around t0 and yield clean chemical contrast.

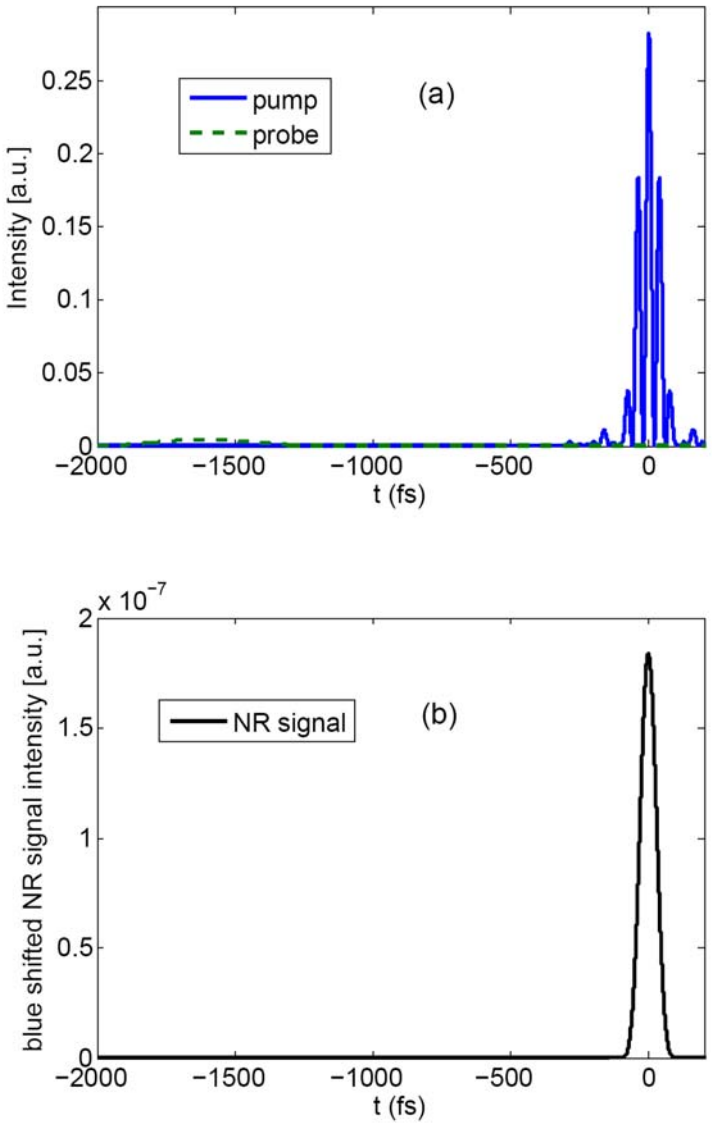

Figure 5.12: (a) Pump pulses and the probe pulse in time domain ;(b) the blue shifted nonresonant signal.

5.6 Signal to noise ratio comparison between spectral domain and time domain methods

Suppose a total of b^2 and a^2 photons of the local field signal and the resonant signal, respectively, are collected over a data acquisition time of t. If the IFTCARS measurement is composed of N equal time steps, then in each time step, the collected photons of the local field and and resonant signal on average are b^2/N and a^2/N, and the oscillatory signal is $(2ab\cos\Delta\phi(t))/N$. If the noise is dominated by the shot noise from the local field, then the noise from each time step is $\sqrt{b^2/N}$. In the Fourier transform, the oscillatory signal from each time step adds up coherently. The signal amplitude in the spectral domain is linearly proportional to N, the number of the time steps involved, provided the signal amplitude at each step is a constant. The noise, however, adds up incoherently. The noise amplitude in the spectral domain is proportional to $\sqrt{N}$. So after Fourier transform, in the spectral domain, we have

$$signal = 2ab/N \times N/2 = ab \tag{5.1}$$

$$noise = \sqrt{b^2/N} \times \sqrt{N} = b \tag{5.2}$$

$$SNR = a \tag{5.3}$$

Two conclusions can be drawn from the above arguments: firstly, the SNR of IFTCARS is not affected by the detection bandwidth. This still holds true even if the bandwidth is so large that the average collected photon number is below one. Secondly, the SNR is independent of the amount of the local field. This is expected due to the shot-noise limited character of the measurement. The first conclusion can be verified through numerical simulation. In the simulation, the number of total photons acquired was 5E4. The E field ratio between resonant signal and the local

field is 0.025 which matches the experimental data of 2-propanol. A single Raman mode of 40 fs period is assumed in the calculation. The number of time domain steps is taken to be 5E3, 5E4, and 5E5, and the range of delay scan is 2ps. A Poisson distribution is used to describe the photon statistics. The simulation result is shown in Fig.5.13. From the total photon number and the relative E field ratio, we know the total photon numbers of the resonant signal and local field. From Eq.5.3, we compute a SNR of 5.6 which matches the simulation results regardless of the sampling rate.

Here we consider the SNR analysis for TDSCARS and ITDSCARS. In TDSCARS, if the resonant signal is large enough to reach the shot-noise-limited regime, the SNR is $a^2/a = a$ which is the same as in IFTCARS. If the resonant signal is so small that a local field is required to reach the shot-noise-limited regime, ITDSCARS should be used. In ITDSCARS, the signal is produced by interference between the local field and the resonant signal, and the noise is dominated by the shot noise from the local field. This yields the SNR, $ab/b = a$. Thus the highest SNR in the spectral domain method is the same as in IFTCARS given that the same amount of the resonant signal(a^2) is detected and the measurement is shot-noise limited.

5.7 Signal to noise ratio comparison (experiment)

We used 2-propanol as the sample to compare time and spectral domain methods. The delay scan range of the time domain measurement is 300-2900 fs. The probe pulse(centered at 741.5nm, 4nm width) time delay in the spectral domain method is 1600 fs, chosen to limit the NR contribution. The total input power of each measurement is 6mW. At this input power the resonant signal is large enough to reach the shot-noise-limited regime and ITDSCARS is not needed. The spectral domain data measured in 2propanol and water is shown in Fig.5.14. The peak

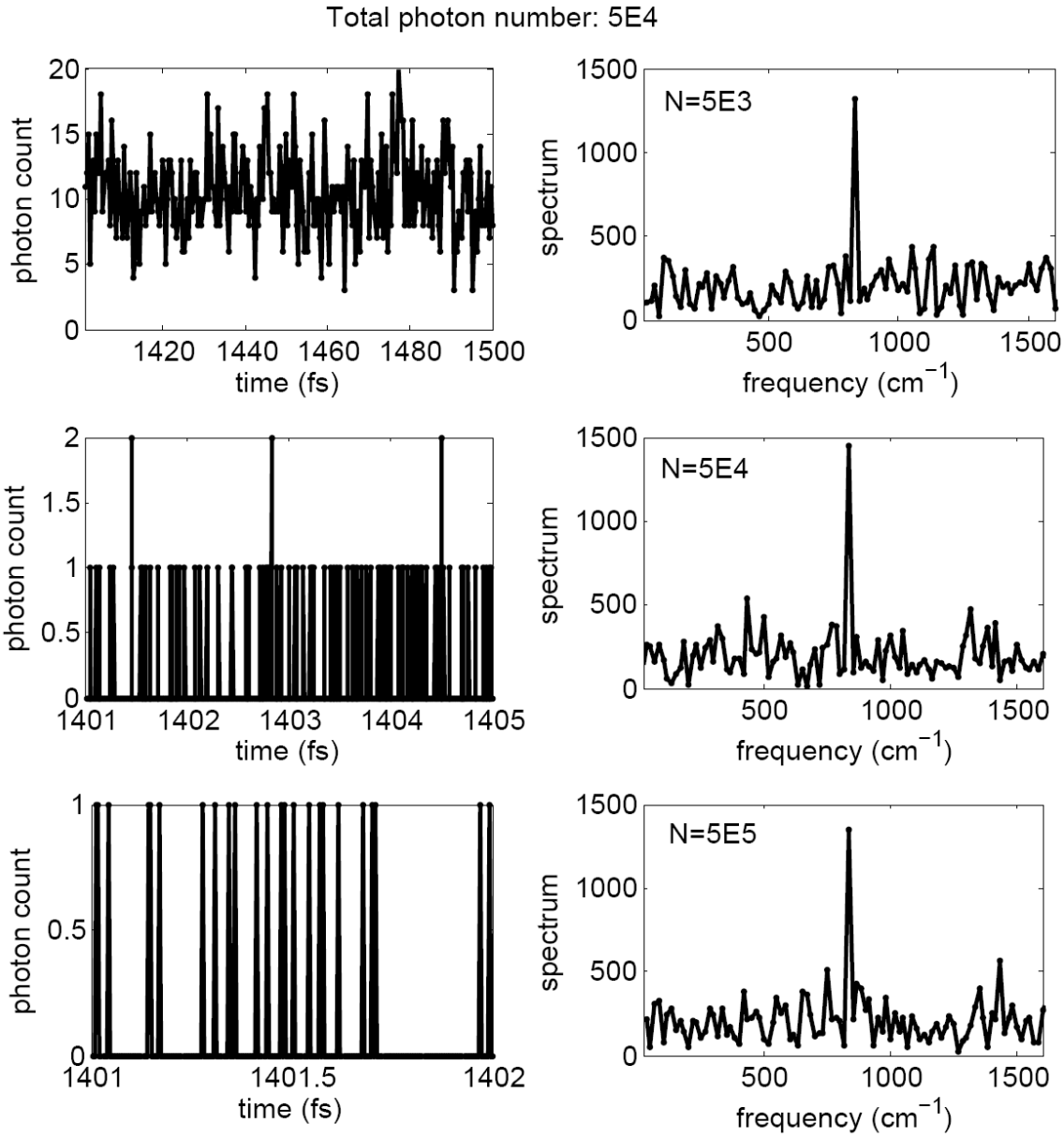

Figure 5.13: Simulation of IFTCARS SNR. The three plots on the left side are the time domain signal; The three plots on the right side are corresponding spectra from the Fourier transform. The total photon number is 5E4. Three different detection bandwidths are considered with a total number of time steps of 5E3, 5E4, and 5E5. Note in the case of 5E5, the average photon number per time step is 0.1. A Poisson distribution is used to describe the photon statistics.

around 500cm^{-1} is the NR signal generated by the two pump pulses. The sharp edge is cut by a short-pass filter at 725nm placed in front of the spectrometer to block the laser light. The 2-propanol spectrum shows the expected CARS signal around 820cm^{-1}, while the acquired spectrum for water is flat in this region. The resolution of this measurement is limited by the width of the probe pulse (4nm). Two methods can be used to estimate the ratio of NR signal to resonant signal. One is to compare the data measured in water and in 2propanol. The amount of NR signal generated in the two samples may have a slight difference, but the shape is preserved. We can use the water spectrum to estimate the amount of NR signal around 820cm^{-1} in 2propanol. The second method is to directly measure the spectral interference fringe contrast. To lower the read noise of the CCD, the 1340 pixels of the CCD are binned into 134 effective pixels. The reduced resolution makes the first method more reliable. From the measured spectrum, the NR signal is estimated to be $\sim 3\%$ of the resonant signal.

To estimate the spectral domain SNR, 100 spectra are recorded with a one second exposure time for each spectrum (Fig.5.15). The signal is the mean peak height, and the noise is the standard deviation of the peak height, measured to be 102 photons. This compares well with the shot-noise limited value of 93 counts obtained from the peak height (8731 counts) of the signal at 820cm^{-1}. The SNR of the measurement is 86.

To perform the time domain measurements, the FTCARS method was used and the CCD pixels were binned into one effective pixel. The time domain data measured for 2-propanol with FTCARS is shown in Fig.5.16. The signal is defined as the peak height in the Fourier transformed spectrum. There are two ways to estimate the amount of noise. One is to measure the standard deviation of the signal in the

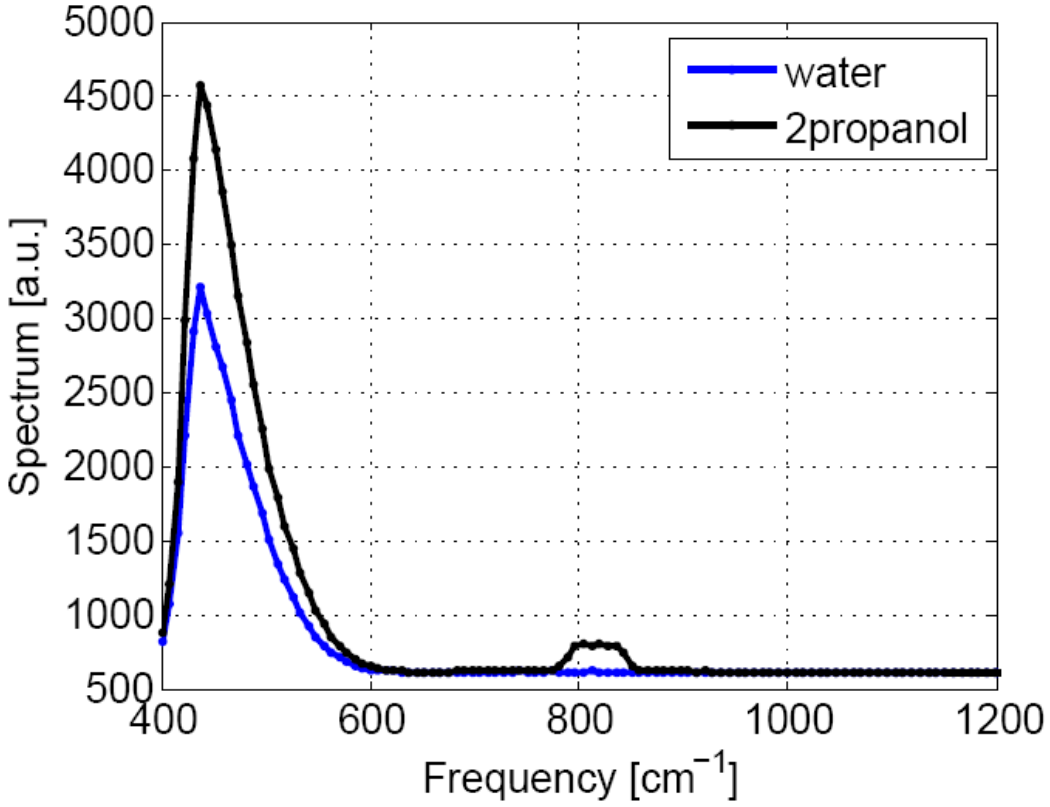

Figure 5.14: Measured CARS spectrum of 2propanol and water with 1600fs delay on the probe beam.

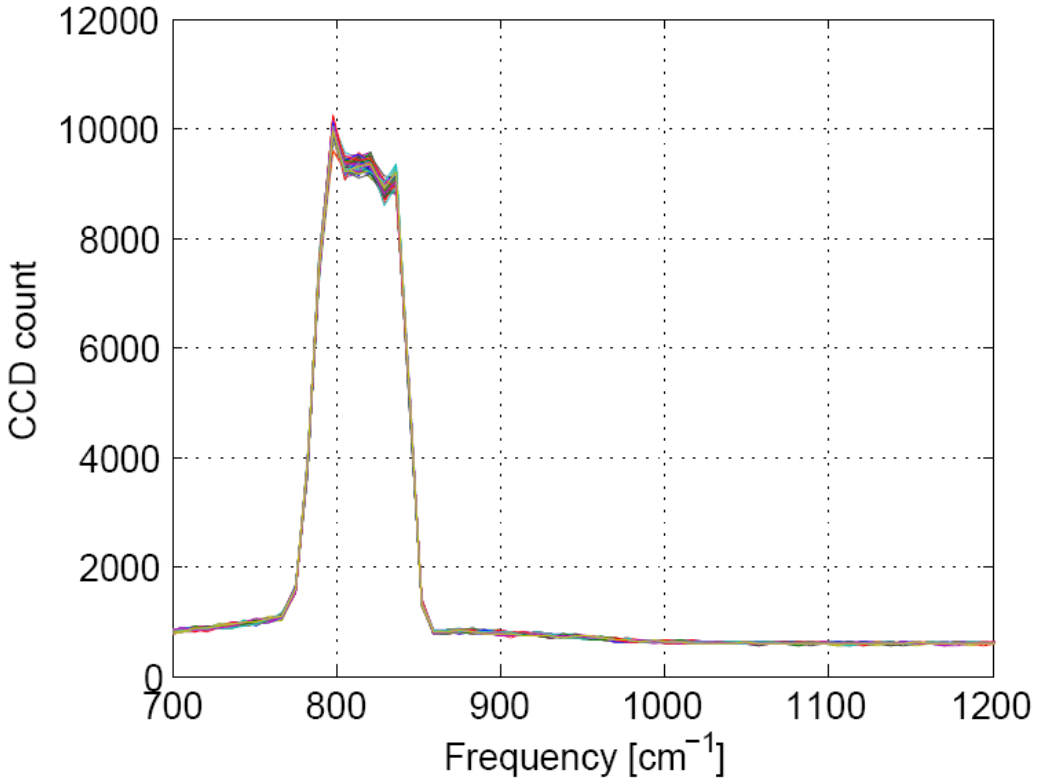

Figure 5.15: 100 2-propanol CARS spectra. Exposure time of each spectrum is one second.

spectrum away from the peak. The other is to repeat the measurement many times and obtain the standard deviation of the peak height fluctuation. If the noise is dominated by the shot noise from the local field, these two methods yield the same result, which we confirmed by measurement, obtaining a SNR of 80. The effective data acquisition time is 1.7 seconds. If the time is reduced to one second to match the spectral domain measurements, the SNR is estimated to be $80/\sqrt{1.7} = 61$. In FTCARS, the NR signal generated by the first pulse generates shot noise and reduces the SNR of the measurement. If IFTCARS is used to suppress this noise, the SNR can be increased to $61 \times \sqrt{2} = 87$, which compares well with results obtained from the spectral domain method.

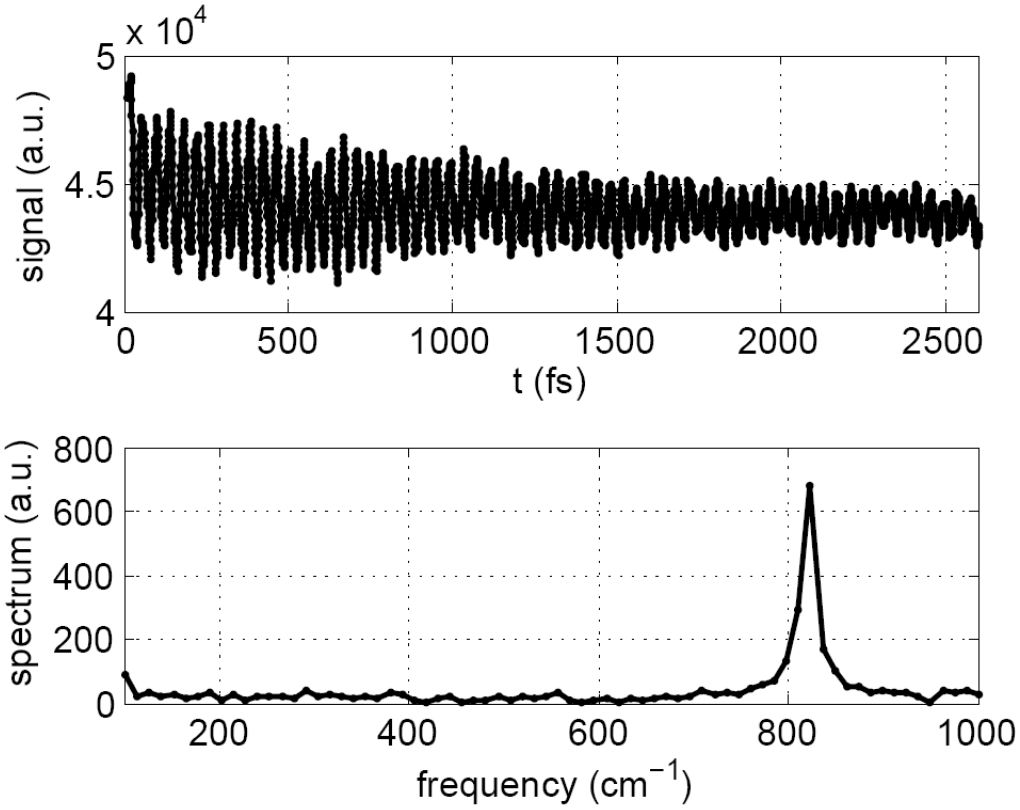

Figure 5.16: FTCARS time domain data and its Fourier transform

5.8 Conclusion

In this chapter, the theory and implementation of TDSCARS and ITDSCARS are discussed. Similar to FTCARS and IFTCARS, a time delay is employed to reduce the NR background and increase the chemical contrast in TDSCARS and ITDSCARS. The SNR of TDSCARS is compared to that of FTCARS both in theory and in experiment. Under shot-noise-limited conditions, both methods yield similar SNR.

Practically, the noise characteristics of the different detectors used in time and spectral domain measurements must also be considered. The higher quantum efficiency of CCD detectors over PMTs can offer some improvement (approximately a factor of 2) in SNR for shot-noise-limited CARS imaging. We also note that while FTCARS requires only a single detector, avoiding grating losses, this benefit is offset by losses due to imperfect filters, and the fact that the resonant signal that is not sufficiently blueshifted with respect to the probe is rejected in our spectral filtering method. Other considerations important for biological imaging must include sample photodamage. Koester et al. have studied photodamage in cells using 75 fs-3.2 ps pulse durations [70]. They have found that photodamage scales nonlinearly with incident intensity, providing motivation for using longer pulses. The pixel dwell time may also be a consideration for minimizing photodamage. By rapidly scanning one line in the image while scanning the time delay, FTCARS returns multiple times to make measurements at a given sample position, but has a shorter dwell time at each measurement. Depending on the dominant photodamage mechanism, this could provide an advantage over spectral domain methods that have longer consecutive dwell times at a given sample position.

CHAPTER VI

Coherent versus incoherent Raman scattering

6.1 Introduction

Coherent Raman microscopy is commonly considered to be superior to microscopy based on spontaneous Raman scattering. The benefits of CARS are thought to be threefold: 1) the blue shifted signal can be easily separated from red-shifted fluorescence signals that are present in some biological samples, 2) the multiphoton nature of CARS provides 3D sectioning ability without the need for confocal detection, 3) the coherent driving force applied to the individual molecules gives rise to the collective radiation of all the molecules inside the excitation volume, greatly enhancing the radiated signal power. The key question addressed in this chapter is whether the latter benefit holds under the conditions relevant for biological imaging. To date, incoherent and coherent methods have not been compared under these conditions, though claims of 4-5 orders of magnitude improvement in SNR are commonly made in the literature [84–88].

To make a legitimate comparison between coherent and incoherent methods, coherent Stokes Raman scattering(CSRS) and spontaneous Raman scattering are directly compared in experiments. CSRS instead of CARS is used for this comparison because the CSRS signal is overlapped with the spontaneous Raman signal in the

spectral domain and therefore the two methods can be compared without changing the detector or the beam alignment. For molecules of a certain concentration, a critical power is determined, below which spontaneous Raman scattering is shown to be superior. The results of this work suggest that at the low excitation conditions necessary for biological imaging, spontaneous Raman microscopy shows comparable or even higher sensitivity, contrary to the common belief that CARS microscopy provides orders of improvement in sensitivity.

6.2 Theory

The theories of incoherent and coherent Raman scattering have been discussed in **Chapter 2**. From Eq.2.36 and 2.38 we see the expected ratio of coherent to spontaneous Raman signal is given by

$$\begin{aligned}\frac{P_{CSRS}}{P_{Raman}} &= \left(\frac{4\pi^2\omega_{CSRS}}{c^2 n_{CSRS}}\right)^2 \frac{\left(\frac{2Nc^4}{\hbar\omega_s^4}\Delta\frac{d\sigma}{d\Omega}\right)^2}{4\Delta\omega^2+\Gamma^2} L^2 \frac{P_1P_2P_3T^2}{A^2\tau^2}/PLN\frac{d\sigma}{d\Omega}\Omega_{collection} \\ &= \left(\frac{4\pi^2\omega_{CSRS}}{c^2 n_{CSRS}}\right)^2 \frac{\left(\frac{2c^4}{\hbar\omega_s^4}\Delta\right)^2 \frac{d\sigma}{d\Omega}}{4\Delta\omega^2+\Gamma^2} NL \frac{P_1P_2P_3T^2}{A^2\tau^2}/P\Omega_{collection} \qquad (6.1)\end{aligned}$$

An experimental comparison of CSRS and spontaneous Raman scattering under spectroscopy condition has been previously reported [89], showing 5 orders of magnitude of enhancement made with coherent scattering using an optical parametric amplifier operating at 1kHz. Eq. 2.38 indicates that the third order coherent scattering has quadratic dependence on T ($T = 1/reprate$) in contrast to the linear incoherent process which is independent of T. Keeping all experimental parameters the same but varying the reprate, we would expect the incoherent scattering to be 10 times as strong as the coherent scattering if the experimental comparison is performed with a 1MHz laser system. Intuitively there exists a critical power at a certain repetition rate below which the linear process is stronger. For biomedical applications, the

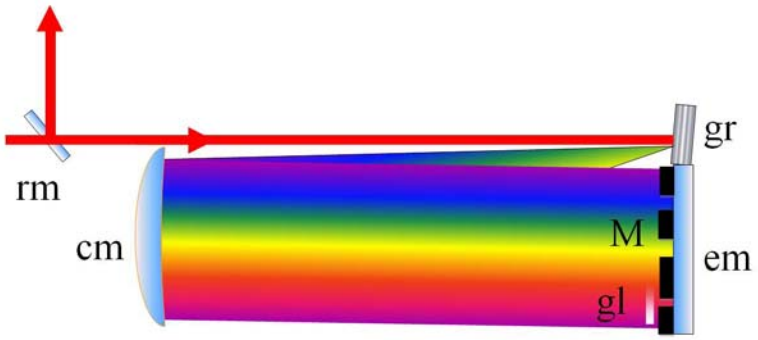

Figure 6.1: CSRS setup. rm: return mirror, cm: concave mirror, gr: grating, M: amplitude mask, gl: glass slide

power used is ideally limited to a few mW. Thus if the critical power is above the mW level, the coherent methods lose their SNR advantage.

Another challenge of biomedical applications is the low molecule concentration. Spontaneous scattering has a linear dependence on the number density in contrast to the quadratic dependence of coherent scattering, which reduces the SNR advantage of coherent methods at low molecule concentrations. A common misconception of coherent methods is that, like spontaneous Raman scattering, the sensitivity of interferometric measurements should have a linear dependence on the molecule density, because the measured quantity is χ_{CARS} instead of $|\chi_{CARS}|^2$[31, 90]. As we discussed in **Chapter 5**, under shot-noise-limited conditions, the SNR of both the direct measurements and interferometric measurements is $\sqrt{n}$, where n is the number of the collected photons of resonant signal. Because it is the SNR not the signal which determines the sensitivity of the measurement, interferometric methods cannot improve the sensitivity at low molecule concentrations.

6.3 Experiment

To make a straightforward comparison, CSRS and Raman signal are measured. The CSRS measurement is performed using the time delayed CARS approach out-

lined in **Chapter 5**. Fig. 6.1 shows the setup of the 4f pulse shaper for the CSRS measurement. The only change from the spectral domain CARS measurement is that the order of the slit position on the mask is reversed such that the probe beam is at the longer wavelength side. In this way, Raman scattering can be directly measured by blocking the two pump beams without changing the alignment or the detector.

A NA 0.4 objective lens is used for focusing the input beam. The focal volume can be determined with two methods. One method is to measure the beam profile at the back aperture of the objective lens and use the calculation techniques discussed in **Chapter 2** to compute the field distribution at the focus. The other method is to use a razor blade to directly block the beam and measure the intensity distribution. Both methods show that the focal volume is $\pi(1.3 \pm 0.07)^2 \times (8 \pm 0.4)\mu m^3$.

If the sample's thickness is much greater than $8\mu m$, the ratio of coherent to incoherent signal will be reduced by the larger interaction volume available for spontaneous Raman scattering. As discussed in **Chapter 2** the excitation volume of a linear process is not confined to the focus as in higher order nonlinear process such as two photon or three photon absorption. Similarly if the thickness is much smaller than $8\mu m$, the ratio is also reduced since the effect is the same as reducing the molecule's concentration. So in our experiments, only samples of the thickness similar to the length of the focus are considered.

To suppress the NR background, a 800fs time delay is applied to the probe pulse with a thin cover slip. The spectral resolution is determined by the linewidth of the probe pulse ($\sim$4nm). Because the signal power is the only concern in this comparison measurement, no attempt was made to improve the spectral resolution. Fig. 6.2 shows the images and spectra of the comparison measurement. Fig. 6.2 (a)-(d) and (e)-(h) are measured on polystyrene beads of $7.3\mu m$ and $4.3\mu m$ in diameter

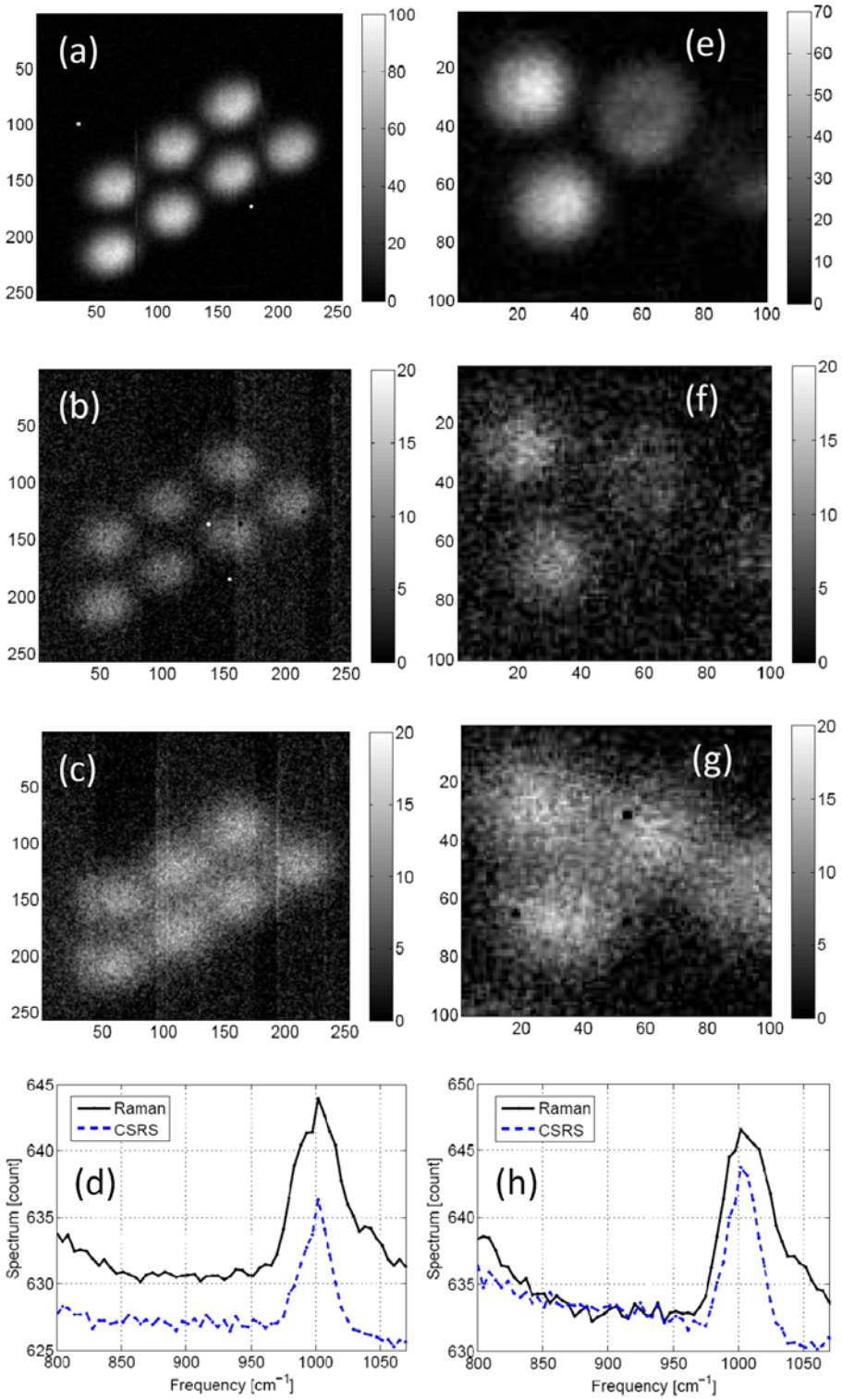

Figure 6.2: (a)-(d) and (e)-(h) are measured on polystyrene beads of 7.3μm and 4.3μm in diameter respectively. The image intensity is the difference in intensity between 1000cm^{-1} and 950cm^{-1}. (a) CSRS, power=4mW, exposure=40msec/pixel. (b) CSRS, power=1.3mW, exposure=100msec/pixel. (c) Raman, power=1.3mW, exposure=100msec/pixel. (d) Averaged spectrum from (b) and (c). (e) CSRS, power=4mW, exposure=50msec/pixel. (f) CSRS, power=1.3mW, exposure=200msec/pixel. (g) Raman, power=1.3mW, exposure=200msec/pixel. (h) Averaged spectrum from (f) and (g). The image sizes are 30μm and 10μm for (a)-(c) and (e)-(g) respectively.

respectively. The difference between the averaged spectral intensity around $1000cm^{-1}$ and around $950cm^{-1}$ is defined as the image intensity. Fig. 6.2 (a) and (e) show the CSRS images measured at 4mW power with 40msec/pixel and 50msec/pixel exposure time respectively. (b) and (c) are direct comparisons of CSRS and Raman respectively with 1.3mW input power and 100msec pixel exposure time. (f) and (g) are direct comparison with 1.3mW input power and 200msec pixel exposure time. The bead looks bigger in the Raman measurement because the signal has a linear dependence on the interaction path length in contrast to the quadratic dependence of the coherent signal. The averaged spectra shown in (d) and (h) are measured at the center of the beads (highest signal intensity), and the spectra show that the peak intensity of the Raman measurement is comparable or slightly higher than that of the CSRS measurement. Therefore the critical power above which coherent Raman provides larger signal than incoherent methods is determined to be ∼1.3mW. If the optimized power ratio (1:1:1) is used for the CSRS measurement, the signal can be increased by a factor of ∼3.5 which reduces the critical power by ∼2 to ∼0.7mW.

The collected spontaneous Raman signal can be increased with a larger collection solid angle. In the experiment, a NA 0.8 condenser is used to collect the forward propagating signal. Due to the size mismatch between the condenser and all the optics after it, the effective NA is estimated to be ∼0.6 which causes a difference in the signal collection efficiency by $2/(1-\cos(\arcsin(0.6)))$. This factor is however not included in the comparison because the collection solid angle in real imaging applications can never reach 4π, and in many applications the back reflected Raman signal is collected with the same objective lens. Not including this factor biases the result towards the coherent method, since it is more efficiently collected.

Based on the ratio derived in Eq.6.1 and using the input power ($P_1 = 0.29mW$,

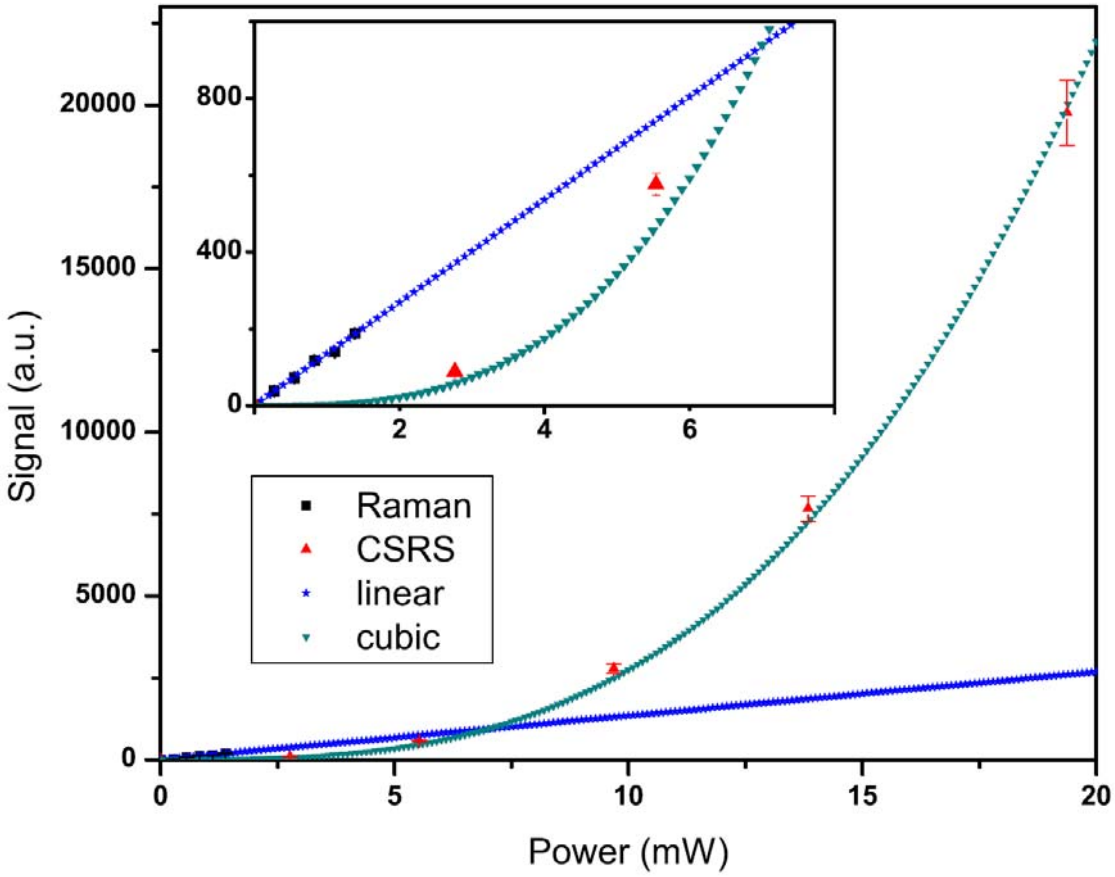

Figure 6.3: Power dependence measurement of 2-propanol sandwiched between two fused silica slides. The optical path length is $\sim 10\mu m$.

$P_2 = 0.93mW$, $P_3 = 0.08mW$), the beam diameter at the focus ($1.36\mu m$), and the physical properties of polystyrene (Density=1.05g/cm^3, Peak Raman cross section measured at 488nm = 0.28x10^{-29}cm^2/(sr.cm^{-1}), Raman linewidth = 8cm^{-1}) we calculate the ratio of coherent to incoherent signal using Eq.6.1 and get $P_{CSRS}/P_{Raman} = 6 \pm 3$ which is reasonably consistent with our measurements.

6.4 Solution measurements

A power dependence measurement is performed on pure 2-propanol to give additional validation. To make the sample thickness comparable to the depth of focus of the beam, two small pieces of aluminum foil of 18 μm thick are sandwiched between

two 1 mm thick fused silica slides. The two pieces of foil are located at two corners of the slides such that the two slides form a wedge. With such a design, the thickness of 2-propanol can be continuously varied to match the depth of the focus. The sample is scanned perpendicular to the beam (z-scan), and the signal variation as a function of the sample position is used to compute the actual sample thickness, which is determined to be $10\pm1\mu m$. Fig. 6.3 shows the power dependence measurement results. The available power at the sample for spontaneous Raman scattering measurement is limited by the spectral density of the Ti:sapphire oscillator to $\sim$1.3mW. The incoherent and coherent data are fitted with a linear and cubic function that pass through the origin. From the inset of Fig.6.3, we can clearly see the crossing of the two fitting curves. The power of the crossing point is the critical power beyond which coherent methods offer improvement over incoherent ones. In this measurement, the critical power is $\sim$7mW. If the optimized power ratio $(1:1:1)$ is used, the CSRS signal can be amplified by a factor of $\sim$3.5, which lowers the critical power by $\sim$2 to $\sim$3.7mW. In the above comparison, the third order nonlinear CSRS signal is compared with spontaneous Raman scattering. If the input power is lower than the critical power, the spontaneous Raman signal generated by the probe pulse in CSRS measurement should also be included. Thus the lower limit for the amount of signal in CSRS should be one third as much as in the spontaneous Raman scattering when equal power is used for the three laser pulses.

All the above measurements were performed in samples of high concentration. If the concentration is reduced as it will be in most biological imaging scenarios, the critical power should be further increased because incoherent scattering has linear dependence on concentration in contrast to the quadratic dependence of the coherent signal.

6.5 Conclusion

In summary, we have directly compared spontaneous Raman scattering to CSRS. Different from an earlier study[89] comparing the two measurements, the input power, pulse energy, beam geometry, focusing, and signal collection all resemble the conditions of biomedical imaging. The critical input power which generates equal amounts of spontaneous and coherent signal is determined in the experiment to be in the few mW range for pure samples and will be considerably higher (a few hundred mW) for lower concentration samples (mMol).

The implication for biomedical applications is that the coherent method has an advantage only if the sample's damage threshold is much higher than the critical power and the nonlinearity of the photo-damage mechanism is low. If the photo-damage mechanism scales linearly with the light intensity, then the repetition rate of the light source used for coherent methods should be as low as the inverse of the imaging pixel dwell time. For a dwell time of $4\mu s/pixel$, a 250kHz system should be used to give the highest possible pulse energy for the coherent method, which can significantly increase the third order nonlinear signal (quadratic dependence on the inverse of the repetition rate). However, if the photo-damage mechanism has nonlinear dependence[70, 71] on the light intensity and the damaging power is close to the critical power, then spontaneous Raman may be preferred for imaging.

In addition, spontaneous Raman has several other advantages: 1) The experiment is greatly simplified with CW lasers, 2) Spontaneous scattering can acquire the entire Raman spectrum (limited only by the bandwidth of the detector) with high resolution, 3) With CW lasers, the light intensity can be much lower than using picosecond or femtosecond pulsed lasers, which is beneficial if the photo-damaging

mechanism has a nonlinear dependence on the light intensity [70, 71]. One disadvantage of spontaneous scattering is that the stronger signal is on the Stokes side which may overlap with fluorescence signals. In biological material, a number of common molecules such as NADH and flavin produce fluorescence signals. A simple solution to this problem is to perform time-gated measurement [91] since fluorescence has much slower decay rate than Raman scattering.

In the literature, there have been a flourish of publications on the development of various CARS microscopies in the past decade [33, 81, 92, 93], while little attention has been paid to quantifying the actual advantage of using CARS over the conventional spontaneous Raman scattering in real applications. The experimental results presented in this chapter provides a basis for evaluating the relative performance of coherent and spontaneous Raman methods in biomedical imaging, and indicates that under many conditions spontaneous Raman may provide higher sensitivity and simplicity.

CHAPTER VII

Coherent Raman scattering in the near field

7.1 Introduction

In the 1970's it was discovered that Raman scattering cross-sections could be dramatically enhanced in the presence of a rough metal surface, [94] an effect that has been called surface-enhanced Raman spectroscopy (SERS). An explosion of research on SERS (for reviews see [95–98]) has shown that SERS sensitivity can reach the single molecule level. However, the signal enhancement is highly sensitive to the metal surface characteristics. Electromagnetic calculations indicate that the enhancements necessary to achieve single molecule detection cannot be explained by electric field enhancement alone, but require an additional enhancement that is chemical in nature, explaining why not all adsorbed molecules achieve the same degree of enhancement.[95] To date, single molecule detection of biological molecules has only been successful using metal colloidal suspensions, where significant enhancements occur only at certain "hot-spots". Until we can better engineer materials to control where these "hot-spots" occur, single molecule SERS will not become a generally applicable technique. In addition to greatly enhancing the sensitivity of Raman scattering, SERS automatically provides high spatial resolution owing to the rapid decrease in the electric field away from the metal surface. Though not as impressive

as the enhancements obtainable by colloidal suspensions, SERS has also been obtained from single metal nanoparticles and has been used for tip-enhanced Raman imaging employing metal AFM tips.[53, 56, 58, 98, 99]

The higher order dependence of CARS signals on the applied electric field suggests that significantly higher enhancements can be obtained with surface enhanced CARS (SECARS) compared to SERS. SECARS was predicted in 1979 by Shen, who demonstrated that surface plasmon waves from a silver surface could enhance CARS signals from benzene at the surface interface.[100] SECARS in silver colloid suspensions was theoretically modeled in 1984[101] and experimentally observed in 1994 by Keifer et al,[102] who obtained enhancements of 2 orders of magnitude in silver colloid solutions. Like early CARS microscopy demonstrations, early experimental SECARS work was hindered by large background signals.[78] These signals arise from nonresonant processes within the sample as discussed previously, as well as fluorescence and four-wave-mixing signals from the metal nanoparticles.[103] More recently, SECARS has been used to obtain single molecule detection of the biological molecule deoxyguanosine monophosphate (dGMP) using a silver colloid suspension.[104] They report 3 orders of magnitude enhancement of SECARS with respect to SERS. In an effort to improve the sensitivity while retaining the chemical specificity of Raman imaging, tip-enhanced CARS (TECARS) was implemented by the Kawata group in 2004.[59, 105] The high sensitivity of TECARS has permitted the Kawata group to image the ring-breathing mode of adenine (1337 cm-1) in clusters of DNA, and they report enhancements of 100 for CARS compared to spontaneous Raman imaging.[59] To date no spectrally-resolved TECARS measurements have been made. In this chapter, a time domain coherent Raman scattering experiment on nanostructured metal substrate is discussed. The measurement results presented here are prelimary

studies to motivate the applications of the background free CARS in the near field for potential imaging and biosensing applications.

7.2 Introduction to surface plasmons

A plasmon is a collective oscillation of an electron gas surrounding the atomic lattice of metal. At a metal's surface, these charge density oscillations give rise to surface plasmons. The motion of electrons is naturally coupled to electromagnetic waves. Solution of Maxwell's equations for p-polarized wave exists at the interface between metal(ε_1) and dielectric medium (ε_2). If we assume the wave vector k is contained in $x-z$ plane ($z\perp$surface), the E field in both media can be written as

$$\mathbf{E}_j = \begin{pmatrix} E_{j,x} \\ 0 \\ E_{j,z} \end{pmatrix} e^{ik_x x + ik_{j,z} z - i\omega t}, \qquad j = 1, 2 \tag{7.1}$$

If both half spaces are source free ($\nabla \cdot \mathbf{D} = 0$), we have

$$k_x^2 + k_{j,z}^2 = \varepsilon_j k^2, \qquad j = 1, 2 \tag{7.2}$$

The continuity of the the parallel component of $\mathbf{E}$ and the perpendicular component of $\mathbf{D}$ leads to

$$E_{1,x} = E_{2,x} \tag{7.3}$$

$$\varepsilon_1 E_{1,z} = \varepsilon_2 E_{2,z} \tag{7.4}$$

There are four linear equations and also four variables. The matrix has to be non-singular to have a solution, requiring the determinant to be 0. Thus the only physical solution is

$$\varepsilon_1 k_{2,z} = \varepsilon_2 k_{1,z} \tag{7.5}$$

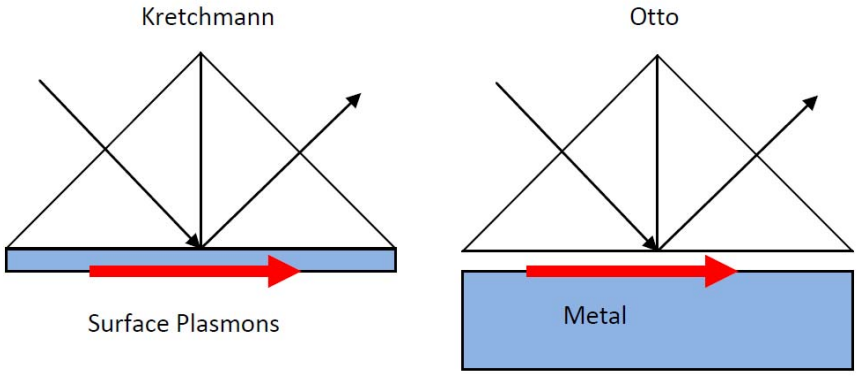

Figure 7.1: Diagrams of the Kretschmann configuration and the Otto configuration

which leads to

$$k_x^2 = \frac{\varepsilon_1 \varepsilon_2}{\varepsilon_1 + \varepsilon_2} \frac{\omega^2}{c^2} \tag{7.6}$$

$$k_{j,z}^2 = \frac{\varepsilon_j^2}{\varepsilon_1 + \varepsilon_2} \frac{\omega^2}{c^2}, \qquad j = 1, 2 \tag{7.7}$$

ε_1(metal) is a complex function of ω in general. The Drude model for free electron gas shows that the oscillation of the electrons is π out of phase with respect to the driving field. Thus the real part of ε_1 is negative. If the imaginary part of ε_1 is neglected, Eq.7.6 shows that $\varepsilon_1 + \varepsilon_2$ has to be negative for a real k_x (propagating wave). From Eq.7.6, we can also tell that the surface plasmon wavevector k_x is greater than the wavevector in the dielectric medium because $\varepsilon_1/(\varepsilon_1 + \varepsilon_2) > 1$. Thus an evanescent wave in a dielectric medium is required to excite surface plasmons.

Two configurations have been proposed to excite surface plasmons. One is the Otto configuration[106] (Fig.7.1), in which an evanescent wave at a glass air interface is used to excite the surface plasmon at an air metal interface. In this configuration, the glass and metal are separated by a thin layer of air. A more stable and convenient configuration is proposed by Kretschmann[107]. In this setup (Fig.7.1), a thin layer of metal is coated on a glass substrate such that the metal is sandwiched between

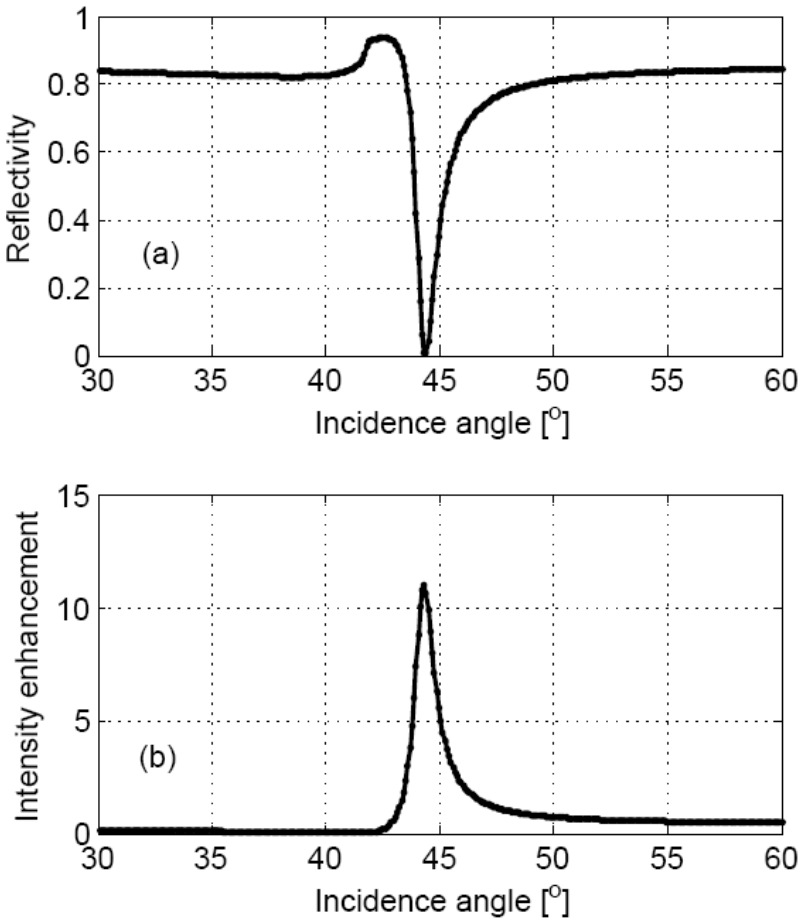

Figure 7.2: Reflectivity (a) and intensity enhancement (b) of glass substrate coated with 50nm gold.

air and glass. Propagating waves in the glass are able to provide a large enough k_x for the surface plasmon at the metal air interface. Based on the parameters and hint from reference[66], the reflectivity and light intensity enhancement are calculated for a 50 nm thin gold layer ($\varepsilon = -11.6 + 1.2i, 633nm$) coated on glass ($n = 1.5$). Fig.7.2 (a) is the calculated reflectivity and (b) is the light intensity enhancement. With this plane substrate, the enhancement is moderate (~ 10). In general, the enhancement is predicted to be greater at the surface of nanoscale sharp metal structures, a claim that has been verified experimentally[108].

7.3 Experiment

As a preliminary step exploring the applications of background free CARS in the near field, a nanostructured substrate is employed to test whether sub 20fs laser pulses can be supported on nanoscale sharp structures. The substrate was purchased from D3 technologies (Klarite). These substrates are routinely used for SERS measurements. The SEM image[7] and the intensity distribution from FDTD simulation for normal incidence[7] is shown in Fig. 7.3 (a) and (b) respectively. The void structure has been designed to give higher stability and reproducibility of enhanced Raman signals.

It has been shown that care must be taken to avoid heating the substrate as heating can cause irreversible morphological changes of the near field hot site through annealing[109]. Initial FTCARS measurements using 75MHz pulse train confirmed this. To reduce the input power and preserve the pulse energy for the nonlinear scattering, a high speed Electro-optical modulator(pulse picker) is employed to reduce the repetition rate of the Ti:sapphire laser system. The total thickness of the KDP crystals inside the pulse picker(Fig.7.4 (a)) is 16cm, which is immersed in index matching oil. The crystal polarizer inside the housing of the pulse picker is removed and a thin film polarizer is used instead external to the housing to reduce the overall material dispersion. To compensate the material dispersion ($\sim 10^4 fs^2$) of the entire system, a 4f pulse shaper (Fig.7.4 (b)) equipped with a 640 pixel liquid crystal spatial light modulator is employed to both measure and compensate the dispersion.

The output of the 4f pulse shaper is sent to the FTCARS setup (Fig.7.5). Instead of collecting the signal in the forward direction, the back scattered light from the nanostructured substrate is collected with the same NA0.4 objective lens. 0.4 μl of

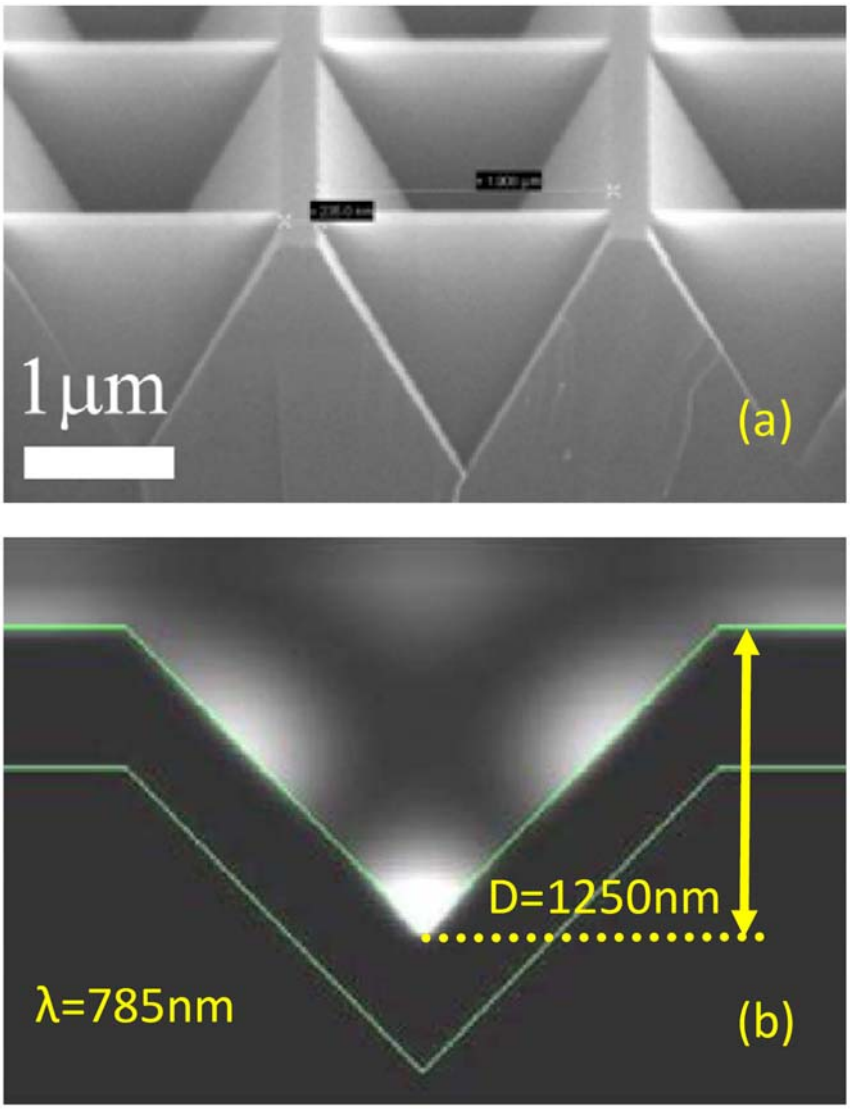

Figure 7.3: (a), SEM image of the nanostructured substrate[7]. (b) Intensity distribution from FDTD simulation for normal incidence. The depth of the void structure is 1250nm and the incident wavelength is 785nm[7].

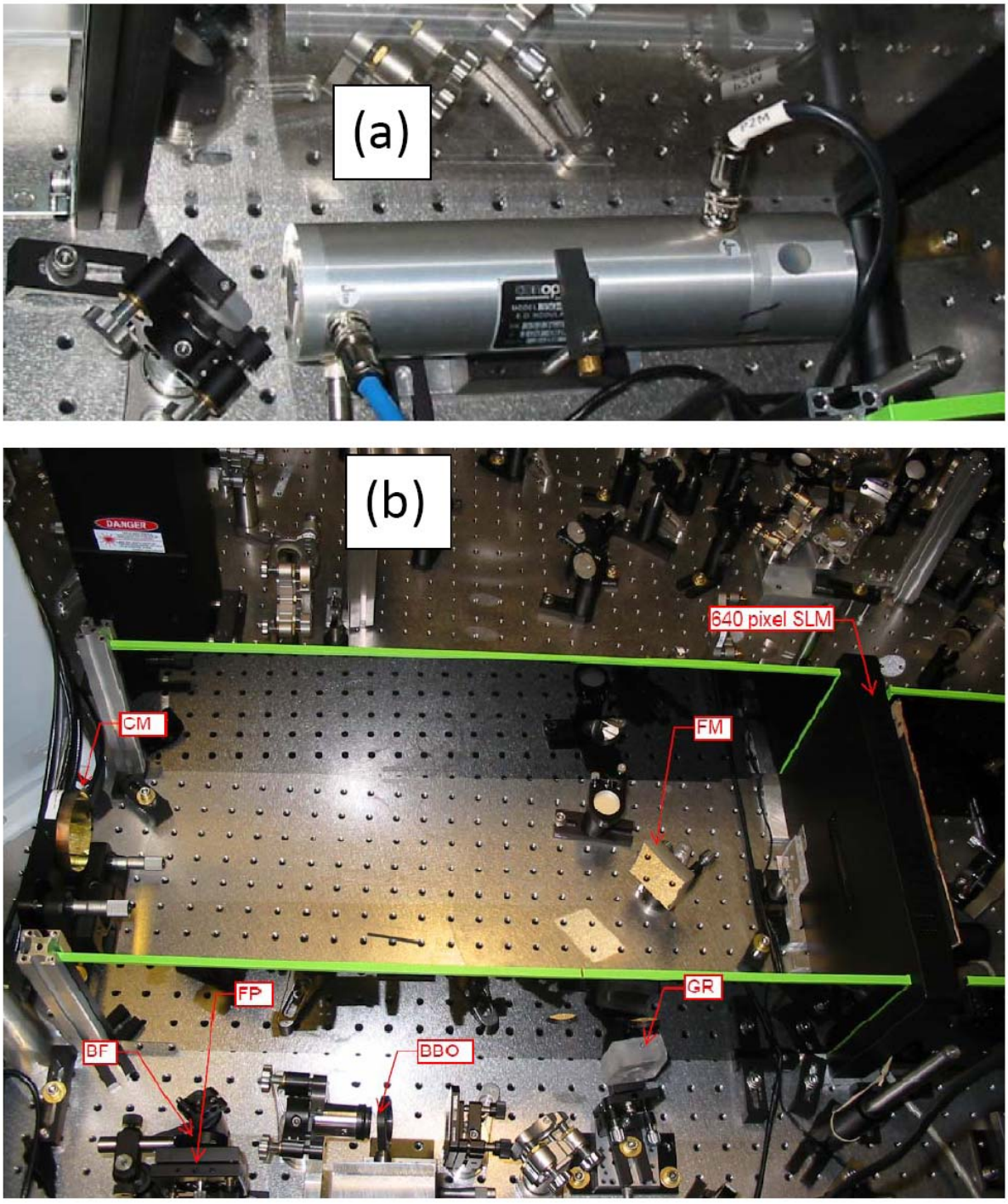

Figure 7.4: (a), photo of the pulse picker. (b) photo of the 4f pulse shaper. The 640 pixel LCD spatial light modulator(SLM) is located at the Fourier plane which is also the symmetry plane of the setup. FM: folding mirror, GR: 600 groves/mm gold coated grating, CM: gold coated concave mirror(f=647mm), BBO: 20μm thick type I BBO crystal for second harmonic generation, BF: bandpass filter for 400nm second harmonic light, FP: fiber coupler to spectrometer.

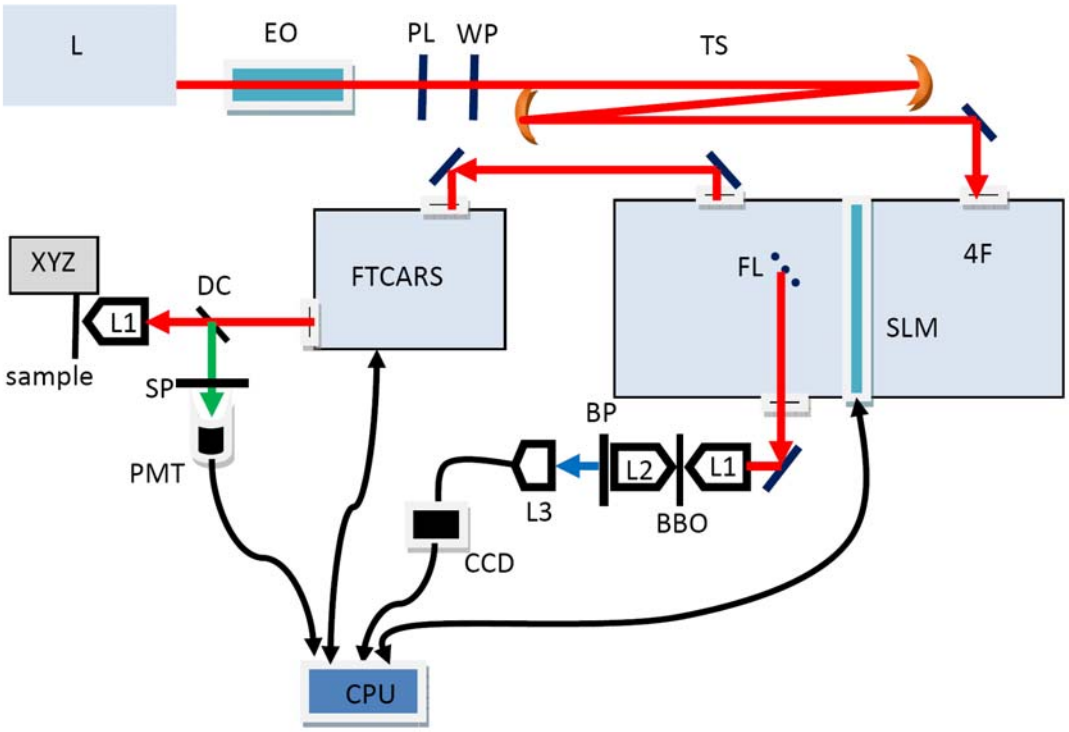

Figure 7.5: L: Ti:sapphire oscillator, EO: pulse picker, PL: thin film polarizer, WP: half wave plate, TS: telescope for beam expansion, 4F: 4f pulse shaper, SLM: 640 pixel spatial light modulator, FL: flipper mirror, L1, L2, L3: objective lens, CCD: compact spectrometer, BP: bandpass filter for 400nm light, DC, dichroic beam-splitter, SP: short pass filter, XYZ: 3D translation stage, sample: benzenethiol on gold coated nanostructured substrate, CPU: computer.

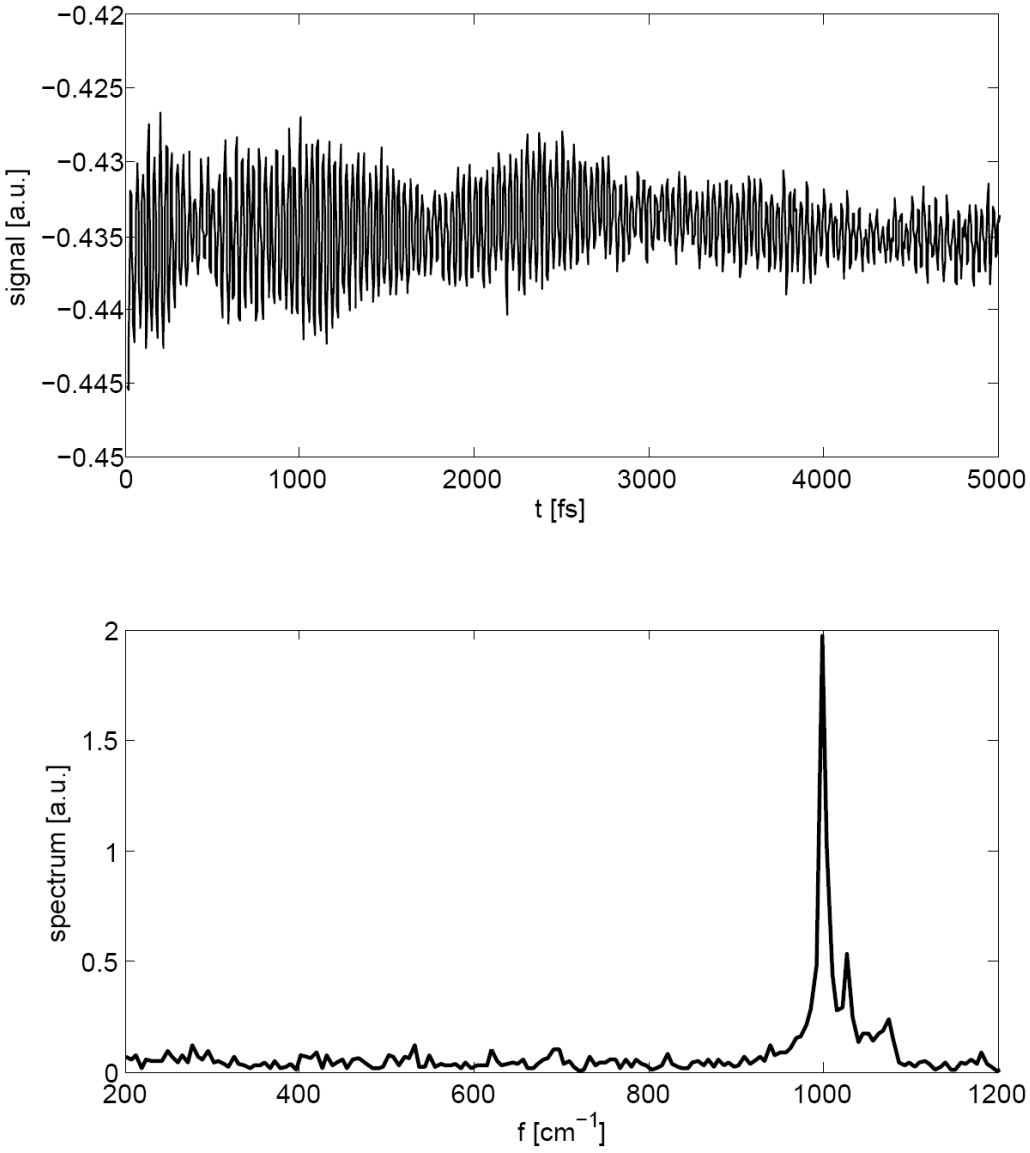

Figure 7.6: (a) FTCARS signal for benzenethiol on the Klarite substrate. (b), Fourier transformed spectrum indicating the modes at 997cm^{-1}, 1021cm^{-1}, and 1072cm^{-1}, as expected from the Raman spectrum[8].

benzenethiol, which attaches to the gold surface with the thiol group, is dried on the substrate. The repetition rate of the Ti:sapphire oscillator is reduced by 10 to 7.5MHz. The total power on the sample is 1.4mW. At this power level, FTCARS can be performed on the substrate for tens of minutes without loss of signal amplitude, indicating that the heating effect is negligible. At repetition rate higher than 15MHz, irreversible signal loss is observed. Fig.7.6 (a) shows the averaged time domain data over 40 scans, which is Fourier transformed to produce the spectrum as is shown in Fig.7.6 (b). The Raman modes of benzenethiol at 997cm^{-1}, 1021cm^{-1}, and 1072cm^{-1} are clearly resolved, as expected from the Raman spectrum [8]. To obtain an idea of the effect of the nanostructured surface on the signal level, the experiment was repeated on a flat section of the gold coated substrate. No detectable FTCARS signal was observed.

7.4 Conclusion

As the first step exploring the applications of the background free CARS in the near field, gold coated nanostructured substrate was employed to provide near field enhancement to the attached benzenethiol molecules. The heating effect is successfully minimized with a high speed pulse picker and a 4f pulse shaper equipped with a 640 pixel SLM for both dispersion measurement and compensation. Areas on the substrate with the nanostructured void show consistent and reproducible signals, while the areas without the nanostructured void show no signal peaks. The ability to resolve the $1000cm^{-1}$ mode of benzenethiol demonstrates that sub 20fs pulses can be supported by such specially engineered surface plasmon substrate, which paves the way for various near field nonlinear spectroscopies and microscopies that require such short pulses. Future work will compare enhancements observed with coherent

and incoherent methods as a way of assessing the possible improvements in sensitivity offered by TECARS for imaging and SECARS for biosensing applications.

CHAPTER VIII

Conclusion

8.1 Summary

In this thesis, we discussed the theory, implementation and applications of time domain CARS methods (FTCARS and IFTCARS). As a time domain multiplex CARS approach, FTCARS allows easy removal of the NR background and acquisition of much of the fingerprint region in a single measurement. The simple setup of FTCARS can be conveniently combined with self-phase modulation imaging (NR imaging) and two photon fluorescent imaging via epi detection. We have applied FTCARS to image polymer samples (PMMA, polystyrene) and biological samples (Caenorhabditis elegans). The simplicity, robustness and multimodality make FTCARS a very promising tool for biological imaging applications.

If the excitation power is low, the generated NR signal may not provide a large enough local oscillator field to suppress the background noise. IFTCARS is a time domain interferometric method which uses the blue edge of the laser pulse as the local oscillator field to suppress the NR background. We implemented IFTCARS in a setup of passive phase stability (better than $\lambda/400$) and demonstrated improved SNR compared to FTCARS, making IFTCARS valuable under low excitation powers.

In Chapter 5, the theory and implementation of TDSCARS and ITDSCARS are

discussed. Similar to FTCARS and IFTCARS, a time delay is employed to reduce the NR background and increase the chemical contrast in TDSCARS and ITDSCARS. The SNR of TDSCARS is compared to that of FTCARS both in theory and in experiment. Under shot-noise-limited conditions, both methods yield similar SNR. Practically, the noise characteristics of the different detectors used in time and spectral domain measurements must also be considered. The higher quantum efficiency of CCD detectors over PMTs can offer some improvement (approximately a factor of 2) in SNR for shot-noise-limited CARS imaging. We also note that while FTCARS requires only a single detector, avoiding grating losses, this benefit is offset by losses due to imperfect filters, and the fact that the resonant signal that is not sufficiently blue-shifted with respect to the probe is rejected in our spectral filtering method.

Coherent Raman methods are often claimed to yield a few orders of magnitude improvement in SNR than incoherent Raman methods. We compared CSRS with spontaneous Raman scattering under experimental conditions relevant for biological imaging application. A critical power can be determined in experiment, above which coherent methods have greater SNR. For high concentration samples such as 2-propanol and polystyrene, the critical power is measured to be on the order of 1mW with a 75MHz oscillator system. This measurement provides a basis for evaluating the SNR advantage of coherent methods, and indicates that in many biological applications, spontaneous Raman measurements may be simpler and more sensitive.

As the first step exploring the applications of the background free CARS in the near field, gold coated nanostructured substrate was employed to provide near field enhancement to the attached benzenethiol molecules. The heating effect is successfully minimized with a high speed pulse picker and a 4f pulse shaper equipped with a 640 pixel SLM for both dispersion measurement and compensation. Areas on the

substrate with the nanostructured void show consistent and reproducible signals, while the areas without the nanostructured void show no signal peaks. The ability to resolve the $1000cm^{-1}$ mode of benzenethiol demonstrates that sub 20fs pulses can be supported by such specially engineered surface plasmon substrate, which paves the way for various near field nonlinear spectroscopies and microscopies that require such short pulses.

8.2 Future directions

From the comparison between coherent with incoherent Raman methods, we know that coherent methods favor high molecule concentrations. Future research should explore the applications in high concentration samples such as polymers, collagens and tissues.

While the light intensity is significantly enhanced in near field microscopy, the number of molecules probed is much reduced. Spontaneous Raman scattering has linear dependence on both the light intensity and the number of molecules while coherent Raman scattering has cubic dependence on the light intensity and quadratic dependence on the number of molecules. Spontaneous Raman scattering has been successfully applied in near field imaging, which indicates that the light intensity enhancement is able to overcome the reduced number of molecules and suggests that coherent methods should work even better in the near field. The next step is to compare spontaneous Raman scattering with coherent Raman scattering in the near field and verify the signal enhancement. Should this enhancement be significant, near field CARS imaging will find applications in biology, chemistry and material science.

APPENDICES

APPENDIX A

Summary of dispersion measurement and compensation

In this appendix, the dispersion measurement and compensation methods employed for the experiments in this thesis are discussed. If the amount of dispersion is low ($\sim 10^3 fs^2$) and the shape of the spectral phase is simple such that it can be approximated with a Taylor series, the dispersion can be measured with the second order autocorrelation and compensated by chirp mirrors or prism pairs, which is summarized in Section A.1. If the amount of dispersion is on the order of $\sim 10^4 fs^2$ and the spectral phase is complicated, sophisticated measurement and compensation methods are required, which is discussed in Section A.2.

A.1 Low dispersion measurement and compensation

The Michelson interferometer inside the FTCARS setup can be conveniently used to generate two collinear pulses for fringe resolved autocorrelation (FRAC). Beta barium borate (BBO) crystal is the most commonly used nonlinear medium for doubling near-IR light. For measuring the dispersion of a high NA water immersed objective lens, the BBO crystal has to be placed to within $\sim 100\mu m$ distance from the front surface of the lens and the generated blue light need to be efficiently collected by another lens and directed to a detector. A simpler solution is to directly use detectors with nonlinear response such as GaAsP diode detector[110] which responses to

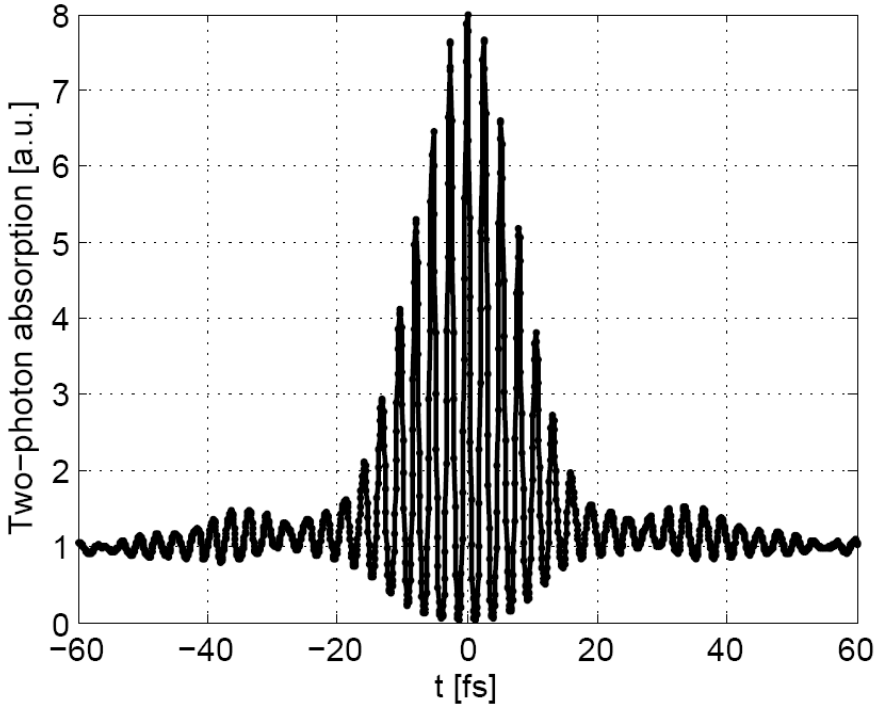

Figure A.1: Second order fringe resolved autocorrelation measured with an GaAsP diode. The dispersion ($\sim 1200fs^2$) of a NA1.2 water immersed lens is compensated by a pair of chirped mirrors. The estimated pulse duration is $\sim 12fs$

visible light via one photon absorption and near-IR light via two-photon absorption. Fig.A.1 shows the second order FRAC measurement with an GaAsP photodiode. The dispersion of a NA1.2 water immersed objective lens is effectively compensated by a pair of chirped mirror providing $-1200fs^2$ dispersion. The estimated pulse duration from this measurement is $\sim 12fs$.

For measuring the blue light(400nm), two-photon photodiode as sensitive as GaAsP to near IR light does not exist and the one photon absorption generates a comparably large signal. To utilize such a diode for pulse measurement, non-collinear beam geometry is required, which makes one-photon signal a flat background since the total power of the two pulses conserves in non-collinear beam geometry in contrast to the power redistribution made possible with the Michelson interferometer. The ZnS photodiode[111] kindly provided by Professor Kam Sing Wong at Hong Kong

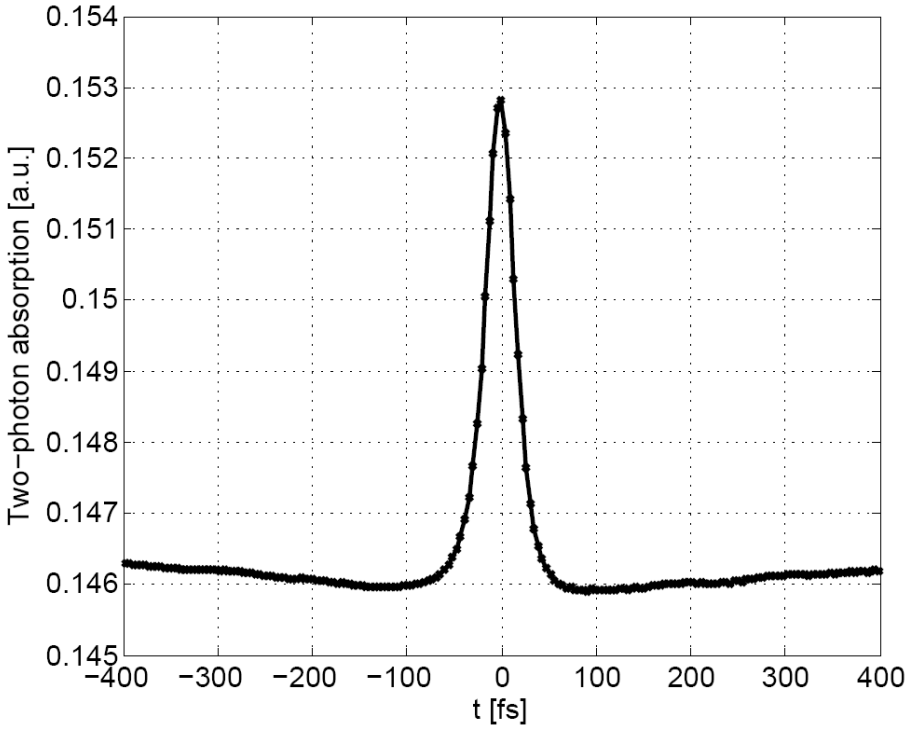

Figure A.2: Non-collinear autocorrelation measured with ZnS photodiode

University of Science and Technology is employed to measure the blue light (centered at $\sim$ 400nm, $\sim$ 10nm bandwidth) generated by our Ti:saphhire oscillator from a 0.1 mm thick type I BBO crystal. Fig.A.2 shows the measured non-collinear autocorrelation. The two photon absorption generates a peak on the top of a large one-photon background. The slope on the baseline is due to the nonlinear saturation of the diode. Fitting the peak to a gaussian function yields a pulse duration of $\sim 27fs$.

A.2 High dispersion measurement and compensation

The pulse picker used for controlling the repetition rate of the laser system is very dispersive ($\sim 10^4 fs^2$) and the spectral phase distortion can not be simply treated as a Taylor series. Under these situations, sophisticated dispersion measurement and compensation methods become necessary.

Multiphoton intrapulse interference phase scan (MIIPS)[112, 113] is a spectral phase shaping technique that can both measure and compensate dispersion. The basic idea of MIIPS is to measure the second harmonic spectrum variation with different applied spectral phase masks allowing the spectral phase profile of the input pulse to be inferred from the measured two dimensional second harmonic spectrum. The MIIPS measurement is implemented with a 4f setup. A 640 pixel LCD spatial light modulator (SLM) is placed in the Fourier plane which is also the symmetry plane of the setup. A flipper mirror is placed inside the 4f to switch the light to between the CARS measurement and a $20\mu m$ thin BBO crystal for the MIIPS measurement. The second harmonic signal from the BBO is filtered to remove the near-IR components and sent into a fiber coupled compact spectrometer. The SLM and the spectrometer are controlled by a Matlab program for implementing the MIIPS measurement. The entire 4f setup is carefully shielded from air currents which can distort the spectral phase and cause significant fluctuation in the generate second harmonic spectrum especially when the laser pulse is compensated to near transform limited. The entire optical table is enclosed by a box with a smaller box enclosing only the 4f setup. The two layers of shielding effectively minimizes the phase distortion caused by air flow.

Depending on the amount of the dispersion, MIIPS measurements are repeated for several times, with the dispersion range reduced and the dispersion resolution increased in each round of measurement. Following the literature[112, 113] the phase scan function used in the measurement is

$$f(\Delta) = \alpha \cos(\gamma\Delta - \delta) \tag{A.1}$$

$$\tag{A.2}$$

where $\Delta = \omega - \omega_0$ and γ is an estimated transform limited pulse duration which

in our measurement is 15fs (the effective bandwidth of the 4f pulse shaper is from 720nm to 850nm), δ is the phase offset and is the parameter being scanned, and α is related to the modulation period. For measuring a very large dispersion, α is first set to a very large number to increase the range of the measurement ($\alpha = 40\pi$ in the first round), and then gradually reduced to smaller numbers ($\alpha = 1.5\pi$ in the last two rounds). Fig.A.3 (a) (b) show the MIIPS scans in the first and the last round of the measurement. The spectral phase information is encoded in the spacing and the shape of the measured spectra. The calculated spectral phase is inverted and plotted in Fig.A.3(c). This phase is applied to the spatial light modulator to compensate the system dispersion, producing the second harmonic spectrum is shown in Fig.A.3(d). This spectrum corresponds well to the spectrum of a transform limited pulse.

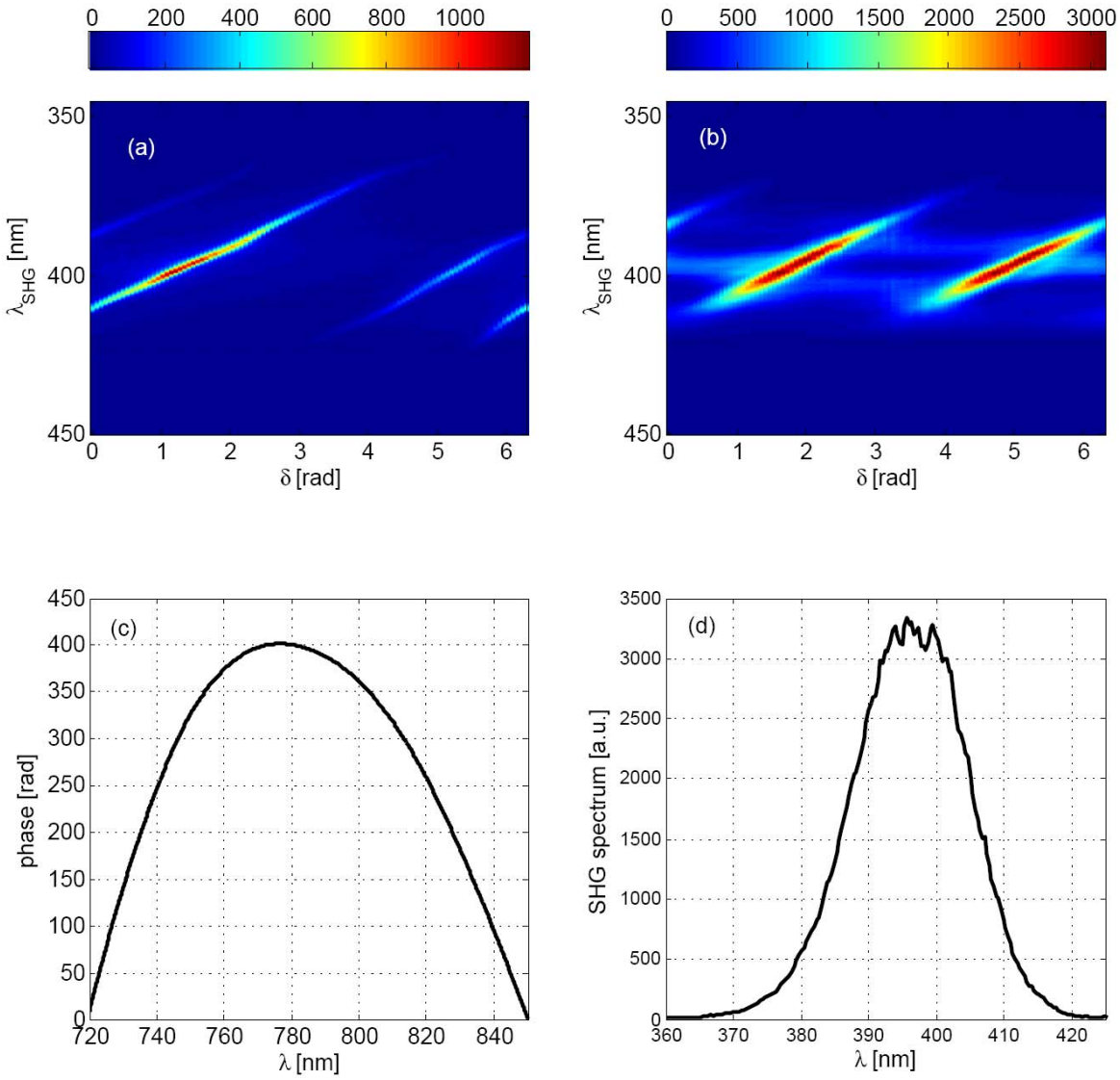

Figure A.3: (a), MIIPS scan in the first round. (b) MIIPS scan in the last round. (c) calculated spectral phase profile. (d) final second harmonic spectrum

APPENDIX B

Table of acronyms

Table B.1: List of acronyms

APD	Avalanche photodiode
BBO	Beta barium borate crystal
CARS	Coherent anti-Stokes Raman scattering
CCD	Charge-coupled device
CSRS	Coherent Stokes Raman scattering
FDTD	Finite-difference time-domain
FTCARS	Fourier transform coherent anti-Stokes Raman scattering
FLIP	Fluorescence loss in photobleaching
FRAP	Fluorescence recovery after photobleaching
FRAC	Fringe resolved autocorrelation
FWM	Four wave mixing
GFP	Green fluorescent protein
IFTCARS	Interferometric Fourier transform coherent anti-Stokes Raman scattering
IPSF	Illumination point spread function
ITDSCARS	Interferometric Time delayed spectral domain Coherent anti-Stokes Raman scattering
MIIPS	Multiphoton intrapulse interference phase scan
NA	Numerical aperture
NR	Nonresonant
PMMA	Poly(methyl methacrylate)
PDT	Photodynamic therapy
PMT	Photomultiplier tube
SECARS	Surface enhanced Coherent anti-Stokes Raman scattering
SERS	Surface enhanced Raman scattering
SHG	Second harmonic generation
SNR	Signal-to-noise ratio
SPM	Self phase modulation
TDSCARS	Time delayed spectral domain Coherent anti-Stokes Raman scattering
THG	Third harmonic generation

BIBLIOGRAPHY

BIBLIOGRAPHY

[1] P. D. Maker and R. W. Terhune. Study of optical effects due to an induced polarization third order in electric field strength. *Physical Review*, 137(3A):801–819, 1965.

[2] EO Potma, DJ Jones, JX Cheng, XS Xie, and J Ye. High-sensitivity coherent anti-Stokes Raman scattering microscopy with two tightly synchronized picosecond lasers. *OPTICS LETTERS*, 27(13):1168–1170, 2002.

[3] GJ PUPPELS, FFM DEMUL, C OTTO, J GREVE, M ROBERTNICOUD, DJ ARNDTJOVIN, and TM JOVIN. STUDYING SINGLE LIVING CELLS AND CHROMOSOMES BY CONFOCAL RAMAN MICROSPECTROSCOPY. *NATURE*, 347 (6290):301–303, SEP 20 1990. ISSN 0028-0836.

[4] JX Cheng, A Volkmer, and XS Xie. Theoretical and experimental characterization of coherent anti-Stokes Raman scattering microscopy. *JOURNAL OF THE OPTICAL SOCIETY OF AMERICA B-OPTICAL PHYSICS*, 19(6):1363–1375, JUN 2002.

[5] A. M. Weiner, D. E. Leaird, G. P. Wiederrecht, and K. A. Nelson. Femtosecond multi-pulse impulsive stimulated raman-scattering spectroscopy. *J. Opt. Soc. Am. B*, 8:1264–1275, 1991.

[6] SW CORNELL and JL KOENIG. LASER-EXCITED RAMAN SCATTERING IN POLYSTYRENE. *JOURNAL OF APPLIED PHYSICS*, 39(11):4883–&, 1968. ISSN 0021-8979.

[7] NMB Perney, JJ Baumberg, ME Zoorob, MDB Charlton, S Mahnkopf, and CM Netti. Tuning localized plasmons in nanostructured substrates for surface- enhanced Raman scattering. *OPTICS EXPRESS*, 14(2):847–857, JAN 23 2006.

[8] Hye Young Jung, Yong-Kyun Park, Sunyho Park, and Seong Kyu Kim. Surface enhanced Raman scattering from layered assemblies of close-packed gold nanopardicles. *ANALYTICA CHIMICA ACTA*, 602(2):236–243, OCT 29 2007.

[9] R HEIM, AB CUBITT, and RY TSIEN. IMPROVED GREEN FLUORESCENCE. *NATURE*, 373(6516):663–664, FEB 23 1995. ISSN 0028-0836.

[10] M Ormo, AB Cubitt, K Kallio, LA Gross, RY Tsien, and SJ Remington. Crystal structure of the Aequorea victoria green fluorescent protein. *SCIENCE*, 273(5280):1392–1395, SEP 6 1996.

[11] A Miyawaki, J Llopis, R Heim, JM McCaffery, JA Adams, M Ikura, and RY Tsien. Fluorescent indicators for Ca2+ based on green fluorescent proteins and calmodulin. *NATURE*, 388 (6645):882–887, AUG 28 1997.

[12] RY Tsien. The green fluorescent protein. *ANNUAL REVIEW OF BIOCHEMISTRY*, 67: 509–544, 1998.

[13] J Stricker, P Maddox, ED Salmon, and HP Erickson. Rapid assembly dynamics of the Escherichia coli FtsZ-ring demonstrated by fluorescence recovery after photobleaching. *PROCEEDINGS OF THE NATIONAL ACADEMY OF SCIENCES OF THE UNITED STATES OF AMERICA*, 99(5):3171–3175, MAR 5 2002.

[14] NB Cole, CL Smith, N Sciaky, M Terasaki, M Edidin, and J LippincottSchwartz. Diffusional mobility of Golgi proteins in membranes of living cells. *SCIENCE*, 273(5276):797–801, AUG 9 1996.

[15] TJ Dougherty, CJ Gomer, BW Henderson, G Jori, D Kessel, M Korbelik, J Moan, and Q Peng. Photodynamic therapy. *JOURNAL OF THE NATIONAL CANCER INSTITUTE*, 90(12):889–905, JUN 17 1998.

[16] PJ Campagnola and LM Loew. Second-harmonic imaging microscopy for visualizing biomolecular arrays in cells, tissues and organisms. *NATURE BIOTECHNOLOGY*, 21(11): 1356–1360, NOV 2003.

[17] D Debarre, W Supatto, AM Pena, A Fabre, T Tordjmann, L Combettes, MC Schanne-Klein, and E Beaurepaire. Imaging lipid bodies in cells and tissues using third-harmonic generation microscopy. *NATURE METHODS*, 3(1):47–53, JAN 2006.

[18] Martin C. Fischer, Henry C. Liu, Ivan R. Piletic, Yasmin Escobedo-Lozoya, Ryohei Yasuda, and Warren S. Warren. Self-phase modulation signatures of neuronal activity. *OPTICS LETTERS*, 33(3):219–221, FEB 1 2008.

[19] C. L. Evans, X. Y. Xu, S. Kesari, X. S. Xie, S. T. C. Wong, and G. S. Young. Chemically-selective imaging of brain structures with cars microscopy. *Optics Express*, 15(19):12076–12087, 2007.

[20] J. X. Cheng, A. Volkmer, L. D. Book, and X. S. Xie. An epi-detected coherent anti-stokes raman scattering (e-cars) microscope with high spectral resolution and high sensitivity. *Journal of Physical Chemistry B*, 105(7):1277–1280, 2001.

[21] M. O. Scully, G. W. Kattawar, R. P. Lucht, T. Opatmy, H. Pilloff, A. Rebane, A. V. Sokolov, and M. S. Zubairy. Fast cars: Engineering a laser spectroscopic technique for rapid identification of bacterial spores. *Proc. Natl. Acad. Sci.*, 99(17):10994–11001, 2002.

[22] T. Hellerer, C. Axang, C. Brackmann, P. Hillertz, M. Pilon, and A. Enejder. Monitoring of lipid storage in caenorhabditis elegans using coherent anti-stokes raman scattering (cars) microscopy. *Proceedings of the National Academy of Sciences of the United States of America*, 104(37):14658–14663, 2007.

[23] M. Muller and J. M. Schins. Imaging the thermodynamic state of lipid membranes with multiplex cars microscopy. *J. Phys. Chem. B*, 106:3715–3723, 2002.

[24] M. D. Duncan, J. Reintjes, and T. J. Manuccia. Scanning coherent anti-stokes raman microscope. *Opt. Lett.*, 7(8):350–352, 1982.

[25] A. Zumbusch, G. R. Holtom, and X. S. Xie. Three-dimensional vibrational imaging by coherent anti-stokes raman scattering. *Physical Review Letters*, 82(20):4142–4145, 1999.

[26] GW Baxter, MJ Johnson, JG Haub, and BJ Orr. OPO CARS: Coherent anti-Stokes Raman spectroscopy using tunable optical parametric oscillators injection-seeded by external-cavity diode lasers. *CHEMICAL PHYSICS LETTERS*, 251(3-4):211–218, 1996.

[27] H Kano and H Hamaguchi. Femtosecond coherent anti-Stokes Raman scattering spectroscopy using supercontinuum generated from a photonic crystal fiber. *APPLIED PHYSICS LETTERS*, 85(19):4298–4300, NOV 8 2004.

[28] H. F. Wang, Y. Fu, P. Zickmund, R. Y. Shi, and J. X. Cheng. Coherent anti-stokes raman scattering imaging of axonal myelin in live spinal tissues. *Biophysical Journal*, 89(1):581–591, 2005.

[29] F. Ganikhanov, C. L. Evans, B. G. Saar, and X. S. Xie. High-sensitivity vibrational imaging with frequency modulation coherent anti-stokes raman scattering (fm cars) microscopy. *Optics Letters*, 31(12):1872–1874, 2006.

[30] J. X. Chen, A. Volkmer, L. D. Book, and X. S. Xie. Multiplex coherent anti-stokes raman scattering microspectroscopy and study of lipid vesicles. *Journal of Physical Chemistry B*, 106(34):8493–8498, 2002.

[31] S.-H. Lim, A. G. Caster, and S. R. Leone. Single-pulse phase-control interferometric coherent anti-stokes raman scattering spectroscopy. *Phys. Rev. A*, 72:041803R, 2005.

[32] S. H. Lim, A. G. Caster, O. Nicolet, and S. R. Leone. Chemical imaging by single pulse interferometric coherent anti-stokes raman scattering microscopy. *Journal Of Physical Chemistry B*, 110(11):5196–5204, 2006.

[33] N. Dudovich, D. Oron, and Y. Silberberg. Single-pulse coherently controlled nonlinear raman spectroscopy and microscopy. *Nature*, 418:512–514, 2002.

[34] D. Oron, N. Dudovich, and Y. Silberberg. Single-pulse phase-contrast nonlinear raman spectroscopy. *Physical Review Letters*, 89(27):273001, 2002. 273001.

[35] D. Oron, N. Dudovich, D. Yelin, and Y. Silberberg. Narrow-band coherent anti-stokes raman signals from broad-band pulses. *Physical Review Letters*, 88(6), 2002. 063004.

[36] N. Dudovich, D. Oron, and Y. Silberberg. Single-pulse coherent anti-stokes raman spectroscopy in the fingerprint spectral region. *J. Chem. Phys.*, 118(20):9208–9215, 2003.

[37] E. Frumker, E. Tal, Y. Silberberg, and D. Majer. Femtosecond pulse-shape modulation at nanosecond rates. *Optics Letters*, 30(20):2796–2798, 2005.

[38] JL OUDAR, RW SMITH, and YR SHEN. POLARIZATION-SENSITIVE COHERENT ANTI-STOKES RAMAN-SPECTROSCOPY. *APPLIED PHYSICS LETTERS*, 34(11):758–760, 1979.

[39] R. Merlin. Generating coherent thz phonons with light pulses. *Solid State Communications*, 102(2-3):207–220, 1997.

[40] Y. X. Yan and K. A. Nelson. Impulsive stimulated light-scattering. 2. comparison to frequency-domain light-scattering spectroscopy. *J. Chem. Phys.*, 87:6257–6265, 1987.

[41] L. Li and J. X. Cheng. Label-free coherent anti-stokes raman scattering imaging of coexisting lipid domains in single bilayers. *Journal of Physical Chemistry B*, 112(6):1576–1579, 2008.

[42] Y. J. Lee and M. T. Cicerone. Vibrational dephasing time imaging by time-resolved broadband coherent anti-stokes raman scattering microscopy. *Applied Physics Letters*, 92(4), 2008.

[43] Georgi I. Petrov, Rajan Arora, Vladislav V. Yakovlev, Xi Wang, Alexei V. Sokolov, and Marlan O. Scully. Comparison of coherent and spontaneous Raman microspectroscopies for noninvasive detection of single bacterial endospores. *PROCEEDINGS OF THE NATIONAL ACADEMY OF SCIENCES OF THE UNITED STATES OF AMERICA*, 104(19):7776–7779, MAY 8 2007.

[44] J. P. Ogilvie, E. Beaurepaire, A. Alexandrou, and M. Joffre. Fourier-transform coherent anti-stokes raman scattering microscopy. *Opt. Lett.*, 31(4):480–482, 2006.

[45] Jennifer P. Ogilvie, Meng Cui, Dmitry Pestov, Alexei V. Sokolov, and Marlan O. Scully. Time-delayed coherent Raman spectroseopy. *MOLECULAR PHYSICS*, 106(2-4):587–594, 2008.

[46] Meng Cui, Joshua P. Skodack, and Jennifer P. Ogilvie. Chemical imaging with Fourier transform coherent anti-Stokes Raman scattering microscopy. *Applied Optics*, 47(31):5790–5798, 2008.

[47] M. Cui, M. Joffre, J. Skodack, and J. P. Ogilvie. Interferometric fourier transform coherent anti-stokes raman scattering. *Optics Express*, 14(18):8448–8458, 2006.

[48] JF de Boer, B Cense, BH Park, MC Pierce, GJ Tearney, and BE Bouma. Improved signal-to-noise ratio in spectral-domain compared with time-domain optical coherence tomography. *OPTICS LETTERS*, 28(21):2067–2069, NOV 1 2003.

[49] MA Choma, MV Sarunic, CH Yang, and JA Izatt. Sensitivity advantage of swept source and Fourier domain optical coherence tomography. *OPTICS EXPRESS*, 11(18):2183–2189, SEP 8 2003.

[50] J. A. McGuire and Y. R. Shen. Signal and noise in fourier-transform sum-frequency surface vibrational spectroscopy with femtosecond lasers. *Journal Of The Optical Society Of America B-Optical Physics*, 23(2):363–369, 2006.

[51] K Kneipp, Y Wang, H Kneipp, LT Perelman, I Itzkan, R Dasari, and MS Feld. Single molecule detection using surface-enhanced Raman scattering (SERS). *PHYSICAL REVIEW LETTERS*, 78(9):1667–1670, MAR 3 1997.

[52] K Kneipp, H Kneipp, VB Kartha, R Manoharan, G Deinum, I Itzkan, RR Dasari, and MS Feld. Detection and identification of a single DNA base molecule using surface-enhanced Raman scattering (SERS). *PHYSICAL REVIEW E*, 57(6):R6281–R6284, JUN 1998.

[53] K Kneipp, AS Haka, H Kneipp, K Badizadegan, N Yoshizawa, C Boone, KE Shafer-Peltier, JT Motz, RR Dasari, and MS Feld. Surface-enhanced Raman Spectroscopy in single living cells using gold nanoparticles. *APPLIED SPECTROSCOPY*, 56(2):150–154, FEB 2002.

[54] Y INOUYE and S KAWATA. NEAR-FIELD SCANNING OPTICAL MICROSCOPE WITH A METALLIC PROBE TIP. *OPTICS LETTERS*, 19(3):159–161, FEB 1 1994.

[55] H Furukawa and S Kawata. Local field enhancement with an apertureless near-field-microscope probe. *OPTICS COMMUNICATIONS*, 148(4-6):221–224, MAR 15 1998.

[56] N Hayazawa, Y Inouye, Z Sekkat, and S Kawata. Metallized tip amplification of near-field Raman scattering. *OPTICS COMMUNICATIONS*, 183(1-4):333–336, SEP 1 2000.

[57] N Hayazawa, Y Inouye, Z Sekkat, and S Kawata. Near-field Raman scattering enhanced by a metallized tip. *CHEMICAL PHYSICS LETTERS*, 335(5-6):369–374, MAR 2 2001.

[58] N Hayazawa, T Yano, H Watanabe, Y Inouye, and S Kawata. Detection of an individual single-wall carbon nanotube by tip-enhanced near-field Raman spectroscopy. *CHEMICAL PHYSICS LETTERS*, 376(1-2):174–180, JUL 17 2003.

[59] T Ichimura, N Hayazawa, M Hashimoto, Y Inouye, and S Kawata. Tip-enhanced coherent anti-Stokes Raman scattering for vibrational nanoimaging. *PHYSICAL REVIEW LETTERS*, 92(22), JUN 4 2004.

[60] B LIEDBERG, C NYLANDER, and I LUNDSTROM. SURFACE-PLASMON RESONANCE FOR GAS-DETECTION AND BIOSENSING. *SENSORS AND ACTUATORS*, 4(2):299–304, 1983.

[61] B LIEDBERG, C NYLANDER, and I LUNDSTROM. BIOSENSING WITH SURFACE-PLASMON RESONANCE - HOW IT ALL STARTED. *BIOSENSORS & BIOELECTRONICS*, 10(8):R1–R9, FAL 1995.

[62] CS WANG. THEORY OF STIMULATED RAMAN SCATTERING. *PHYSICAL REVIEW*, 182(2):482–494, 1969.

[63] G Placzek. *Mark Handbuck der Radiologies*. Academische Verlagsgesellschaft, Leipzig, 1934.

[64] John David Jackson. *Classical Electrodynamics*. Wiley, USA, 1998.

[65] Max Born and Emil Wolf. *Principles of Optics*. Cambridge University Press, UK, 1999.

[66] L Novotny and B Hecht. *Principles of Nano-Optics*. Cambridge University Press, UK, 2006.

[67] C Xu, W Zipfel, JB Shear, RM Williams, and WW Webb. Multiphoton fluorescence excitation: New spectral windows for biological nonlinear microscopy. *PROCEEDINGS OF THE NATIONAL ACADEMY OF SCIENCES OF THE UNITED STATES OF AMERICA*, 93 (20):10763–10768, OCT 1 1996.

[68] JX Cheng and XS Xie. Greens function formulation for third-harmonic generation microscopy. *Journal of the Optical Society of America B*, 19(7):1604–1610 , 2002.

[69] WM TOLLES, JW NIBLER, JR MCDONALD, and AB HARVEY. REVIEW OF THEORY AND APPLICATION OF COHERENT ANTI-STOKES RAMAN-SPECTROSCOPY (CARS). *APPLIED SPECTROSCOPY*, 31(4):253–271, 1977. ISSN 0003-7028.

[70] HJ Koester, D Baur, R Uhl, and SW Hell. Ca2+ fluorescence imaging with pico- and femtosecond two-photon excitation: Signal and photodamage. *BIOPHYSICAL JOURNAL*, 77 (4):2226–2236, 1999.

[71] A Hopt and E Neher. Highly nonlinear photodamage in two-photon fluorescence microscopy. *BIOPHYSICAL JOURNAL*, 80(4):2029–2036, 2001.

[72] WR Zipfel, RM Williams, and WW Webb. Nonlinear magic: multiphoton microscopy in the biosciences. *NATURE BIOTECHNOLOGY*, 21(11):1368–1376, NOV 2003.

[73] L Lepetit, G Cheriaux, and M Joffre. Linear techniques of phase measurement by femtosecond spectral interferometry for applications in spectroscopy. *JOURNAL OF THE OPTICAL SOCIETY OF AMERICA B-OPTICAL PHYSICS*, 12(12):2467–2474, DEC 1995.

[74] TD Klots. Raman vapor spectrum and vibrational assignment for pyridine. *SPECTROCHIMICA ACTA PART A-MOLECULAR AND BIOMOLECULAR SPECTROSCOPY*, 54(10): 1481–1498, SEP 1998.

[75] M. C. Fischer, T. Ye, G. Yurtsever, A. Miller, M. Ciocca, W. Wagner, and W. S. Warren. Two-photon absorption and self-phase modulation measurements with shaped femtosecond laser pulses. *Optics Letters*, 30(12):1551–1553, 2005.

[76] N Uzunbajakava, A Lenferink, Y Kraan, E Volokhina, G Vrensen, J Greve, and C Otto. Nonresonant confocal Raman imaging of DNA and protein distribution in apoptotic cells. *BIOPHYSICAL JOURNAL*, 84(6):3968–3981, JUN 2003.

[77] A. Gatti, E. Brambilla, L. A. Lugiato, and M. I. Kolobov. Quantum entangled images. *Phys. Rev. Lett.*, 83(9):1763–1766, Aug 1999. doi: 10.1103/PhysRevLett.83.1763.

[78] Y. R. Shen. *The Principles of Nonlinear Optics*. Wiley Interscience, New Jersey, 2003.

[79] Marc D. Levenson. *Introduction to nonlinear laser spectroscopy*. Academic Press, USA, 1982.

[80] TH Zhang, CN Borca, XQ Li, and ST Cundiff. Optical two-dimensional Fourier transform spectroscopy with active interferometric stabilization. *OPTICS EXPRESS*, 13(19):7432–7441, SEP 19 2005.

[81] D. L. Marks, C. Vinegoni, J. S. Bredfeldt, and S. A. Boppart. Interferometric differentiation between resonant and coherent anti-stokes raman scattering and nonresonant four-wave-mixing processes. *Appl. Phys. Lett.*, 85(23):5787–5789, 2004.

[82] G. W. Jones, D. L. Marks, C. Vinegoni, and S. A. Boppart. High-spectral-resolution coherent anti-stokes raman scattering with interferometrically detected broadband chirped pulses. *Opt. Lett.*, 31(10):1543–1545, 2006.

[83] C Iaconis and IA Walmsley. Spectral phase interferometry for direct electric-field reconstruction of ultrashort optical pulses. *OPTICS LETTERS*, 23(10):792–794, MAY 15 1998.

[84] JX Cheng and XS Xie. Coherent anti-Stokes Raman scattering microscopy: Instrumentation, theory, and applications. *JOURNAL OF PHYSICAL CHEMISTRY B*, 108(3):827–840, JAN 22 2004.

[85] Bernhard von Vacano, Lars Meyer, and Marcus Motzkus. Rapid polymer blend imaging with quantitative broadband multiplex CARS microscopy. *JOURNAL OF RAMAN SPECTROSCOPY*, 38(7):916–926, JUL 2007.

[86] A Volkmer. Vibrational imaging and microspectroscopies based on coherent anti-Stokes Raman scattering microscopy. *JOURNAL OF PHYSICS D-APPLIED PHYSICS*, 38(5):R59–R81, MAR 7 2005.

[87] TW Kee, HX Zhao, and MT Cicerone. One-laser interferometric broadband coherent anti-Stokes Raman scattering. *OPTICS EXPRESS*, 14(8):3631–3640, APR 17 2006.

[88] Hilde A. Rinia, Mischa Bonn, Michiel Muller, and Erik M. Vartiainen. Quantitative CARS spectroscopy using the maximum entropy method: The main lipid phase transition. *CHEMPHYSCHEM*, 8(2):279–287, FEB 2 2007.

[89] Dmitry Pestov, Gombojav O. Ariunbold, Xi Wang, Robert K. Murawski, Vladimir A. Sautenkov, Alexei V. Sokolov, and Marlan O. Scully. Coherent versus incoherent Raman scattering: molecular coherence excitation and measurement. *OPTICS LETTERS*, 32(12):1725–1727, 2007.

[90] E. R. Andresen, S. R. Keiding, and E. O. Potma. Picosecond anti-stokes generation in a photonic-crystal fiber for interferometric cars microscopy. *Optics Express*, 14(16):7246–7251, 2006.

[91] Vladimir V. Yakovlev. Time-gated confocal Raman microscopy. *SPECTROSCOPY*, 22(10): 34–41, OCT 2007.

[92] T. W. Kee and M. T. Cicerone. Simple approach to one-laser, broadband coherent anti-stokes raman scattering microscopy. *Opt. Lett.*, 29(23):2701–2703, 2004.

[93] B. C. Chen and S. H. Lim. Optimal laser pulse shaping for interferometric multiplex coherent anti-stokes raman scattering microscopy. *Journal of Physical Chemistry B*, 112(12):3653–3661, 2008.

[94] FLEISCHM.M, PJ HENDRA, and MCQUILLA.AJ. RAMAN-SPECTRA OF PYRIDINE ADSORBED AT A SILVER ELECTRODE. *CHEMICAL PHYSICS LETTERS*, 26(2):163–166, 1974. ISSN 0009-2614.

[95] Martin Moskovits. Surface-enhanced Raman spectroscopy: a brief perspective. In *SURFACE-ENHANCED RAMAN SCATTERING: PHYSICS AND APPLICATIONS*, volume 103 of *TOPICS IN APPLIED PHYSICS*, pages 1–17. 2006.

[96] Katrin Kneipp, Harald Kneipp, and Janina Kneipp. Surface-enhanced Raman scattering in local optical fields of silver and gold nanoaggregatess - From single-molecule Raman spectroscopy to ultrasensitive probing in live cells. *ACCOUNTS OF CHEMICAL RESEARCH*, 39(7):443–450, JUL 18 2006.

[97] A. Hartschuh, H. Qian, A. J. Meixner, N. Anderson, and L. Novotny. Tip-enhanced optical spectroscopy for surface analysis in biosciences. *SURFACE AND INTERFACE ANALYSIS*, 38(11):1472–1480, NOV 2006.

[98] Alexandre Bouhelier. Field-enhanced scanning near-field optical microscopy. *MICROSCOPY RESEARCH AND TECHNIQUE*, 69(7):563–579, JUL 2006.

[99] L Novotny, EJ Sanchez, and XS Xie. Near-field optical imaging using metal tips illuminated by higher-order Hermite-Gaussian beams. *ULTRAMICROSCOPY*, 71(1-4):21–29, MAR 1998.

[100] CK CHEN, ARBD CASTRO, YR SHEN, and F DEMARTINI. SURFACE COHERENT ANTI-STOKES RAMAN-SPECTROSCOPY. *PHYSICAL REVIEW LETTERS*, 43(13): 946–949, 1979. ISSN 0031-9007.

[101] H CHEW, DS WANG, and M KERKER. SURFACE ENHANCEMENT OF COHERENT ANTI-STOKES RAMAN-SCATTERING BY COLLOIDAL SPHERES. *JOURNAL OF THE OPTICAL SOCIETY OF AMERICA B-OPTICAL PHYSICS*, 1(1):56–66, 1984. ISSN 0740-3224.

[102] EJ LIANG, A WEIPPERT, JM FUNK, A MATERNY, and W KIEFER. EXPERIMENTAL-OBSERVATION OF SURFACE-ENHANCED COHERENT ANTI-STOKES-RAMAN SCATTERING. *CHEMICAL PHYSICS LETTERS*, 227(1-2):115–120, SEP 2 1994.

[103] L Novotny and SJ Stranick. Near-field optical microscopy and spectroscopy with pointed probes. *ANNUAL REVIEW OF PHYSICAL CHEMISTRY*, 57:303–331, 2006.

[104] TW Koo, S Chan, and AA Berlin. Single-molecule detection of biomolecules by surface-enhanced coherent anti-Stokes Raman scattering. *OPTICS LETTERS*, 30(9):1024–1026, MAY 1 2005.

[105] S Kawata, T Ichimura, N Hayazawa, Y Inouye, and M Hashimoto. Tip-enhanced near-field CARS microscopy. *JOURNAL OF NONLINEAR OPTICAL PHYSICS & MATERIALS*, 13 (3-4):593–599, DEC 2004.

[106] A OTTO. EXCITATION OF NONRADIATIVE SURFACE PLASMA WAVES IN SILVER BY METHOD OF FRUSTRATED TOTAL REFLECTION. *ZEITSCHRIFT FUR PHYSIK*, 216(4):398–&, 1968.

[107] KRETSCHM.E. DETERMINATION OF OPTICAL CONSTANTS OF METALS BY EXCITATION OF SURFACE PLASMONS. *ZEITSCHRIFT FUR PHYSIK*, 241(4):313–&, 1971.

[108] Weihua Zhang, Xudong Cui, Boon-Siang Yeo, Thomas Schmid, Christian Hafner, and Renato Zenobi. Nanoscale roughness on metal surfaces can increase tip-enhanced Raman scattering by an order of magnitude. *NANO LETTERS*, 7(5):1401–1405, MAY 2007.

[109] Weihua Zhang, Thomas Schmid, Boon-Siang Yeo, and Renato Zenobi. Near-field heating, annealing, and signal loss in tip-enhanced Raman spectroscopy. *JOURNAL OF PHYSICAL CHEMISTRY C*, 112(6):2104–2108, FEB 14 2008.

[110] JK Ranka, AL Gaeta, A Baltuska, MS Pshenichnikov, and DA Wiersma. Autocorrelation measurement of 6-fs pulses based on the two-photon-induced photocurrent in a GaAsP photodiode. *OPTICS LETTERS*, 22(17):1344–1346, SEP 1 1997.

[111] T Sun, BKK Fung, IK Sou, GKL Wong, KS Wong, and G Lanzani. Two-photon absorption autocorrelation of visible to ultraviolet femtosecond laser pulses using ZnS-based photodetectors. *IEEE PHOTONICS TECHNOLOGY LETTERS*, 14(1):86–88, 2002.

[112] BW Xu, JM Gunn, JM Dela Cruz, VV Lozovoy, and M Dantus. Quantitative investigation of the multiphoton intrapulse interference phase scan method for simultaneous phase measurement and compensation of femtosecond laser pulses. *JOURNAL OF THE OPTICAL SOCIETY OF AMERICA B-OPTICAL PHYSICS*, 23(4):750–759, APR 2006.

[113] VV Lozovoy, I Pastirk, and M Dantus. Multiphoton intrapulse interference. IV. Ultrashort laser pulse spectral phase characterization and compensation. *OPTICS LETTERS*, 29(7): 775–777, APR 1 2004.